universität wien

MASTERARBEIT | MASTER'S THESIS

Titel | Title

Introduction of multiple slip systems for anisotropic microstructure modelling in FEM-framework

verfasst von | submitted by

Leo Schwarzmeier BSc

angestrebter akademischer Grad | in partial fulfilment of the requirements for the degree of

Master of Science (MSc)

Wien | Vienna, 2025

Studienkennzahl lt. Studienblatt | Degree programme code as it appears on the student record sheet:	UA 066 876
Studienrichtung lt. Studienblatt | Degree programme as it appears on the student record sheet:	Masterstudium Physics
Betreut von | Supervisor:	Dipl.-Phys. Dr. Claas Abert Privatdoz.

Acknowledgements

I specially want to thank my mentor at the Leichtmetallkompetenzzentrum Ranshofen (LKR), Dr. Johannes Kronsteiner, for his support in setting up this master thesis project and for the explanations and time for discussions throughout. Without him, this project would not have been possible. Gratitude and acknowledgements are also in order for Dr. Nikolaus Papenberg and Alois Ott, for their work and support on the simulation input parameter acquisition, the long and detailed explanations they gave me on the topic of metallurgy as well as their preparations done to the measurement data beforehand. Moreover, I am very grateful to my university supervisor Dr. Claas Abert, to oversee a project which might have had a little bit of different than his usual research topics. His advises and input in our monthly meetings was appreciated nonetheless and helped refine this work. Additionally: Special thanks to our intern, Laura Felder, for the support in setting up the simulations and the help in plotting the planes displayed in the stereographic projection of Figure 2.7, Sindre Hovden for supplying the sample geometry as well as my other colleges at LKR for the discussions and brainstorming sessions. Furthermore, thanks to my friends and family for their continuing support.

I also wish to extend my gratitude to the faculty of physics from university of Vienna for allowing me to undertake this work and my employer, LKR, for providing equipment and data.

Finally, funding from the government of Upper Austria through the project "Datenbasierte Optimierung von Rekristallisation, Textur und Eigenspannungen in metallurgischen Prozessen" (Data-T-Rex), grant number: Wi-2021-305676/13-Au, is deeply appreciated.

Abstract

The history of a metal's handling is imprinted on the material, due to the microstructure evolution happening inside, which is known to influence its macroscopic mechanical properties. Predicting the microstructure using forming simulations can help to adjust industrial process parameters to obtain application favourable material properties. However, due to the development of the microstructure being temperature, strain and strain-rate dependent, its evolution might vary at points of different strain rates during large deformations, even within an isotropic alloy composition. This is partly the case because the deformation leads to an increase in thermal energy in the crystal system, which in turn can lower the energy threshold for slip system activation. The presented work explains the physical effects of plastic deformation in polycrystalline metals of isotropic chemical composition and applies a multiscale simulation approach, that couples the evolution of the microstructure via the Visco-Plastic Self-Consistent (VPSC) mean-field model for texture simulations to a commercial Finite Element Method (FEM) software. This method is computationally less expensive than typical crystal plasticity (CP)FEM-models and allows simulating industrial scale metal forming processes together with the developing microstructure. An optimization model is used to determine the 4 parameters per slip mode of the extended Voce hardening law, which is done for an industrial EN AW-5754 (AlMg3) alloy at several constant temperatures by simulating tensile tests and comparing them with measured force-displacement curves. Furthermore, a method for estimating the slip system activation with temperature change is presented. The macroscopic material behaviour of the investigated alloy was brought into good agreement with the measurements of forces at constant temperatures by adjusting the hardening parameters of the microstructure model. The aim of developing a model for simulating temperature dependent industrial metal forming processes that depends on only a few, easily determined material parameters was achieved and evaluated against experimental results.

Kurzfassung

Die innere Struktur eines Metalls ist das Ergebnis der durchlaufenen Prozesse und hat einen großen Einfluss auf die Eigenschaften eines Werkstoffes. Die Vorhersage der Mikrostruktur mithilfe von Umformsimulationen kann helfen, industrielle Prozessparameter anzupassen, um anwendungsfreundliche Materialeigenschaften zu erhalten. Da die Mikrostrukturentwicklung jedoch von der Temperatur, der Dehnung und der Dehnungsrate abhängt, kann sie bei großen Verformungen selbst bei einer isotropen Legierungszusammensetzung an Stellen unterschiedlicher Dehnungsraten variieren. Teilweise ist dies der Fall, weil die Verformung zu einer Erhöhung der Wärmeenergie im Kristallsystem führt, welche wiederum die Energieschwelle für eine Gleitsystemaktivierung senken kann. Die vorliegende Arbeit erklärt die physikalischen Effekte plastischer Verformung in polykristallinen Metallen isotroper chemischer Zusammensetzung und wendet einen mehrskaligen Simulationsansatz an, der die Mikrostrukturentwicklung über das Visco-Plastic Self-Consistent (VPSC)-Mittelfeldmodell für Textursimulationen mit einer kommerziellen Finite Element Method (FEM)-Software koppelt. Diese Methode ist weniger rechenaufwendig als typische Kristallplastizitäts-, eng. crystal plasticity (CP), CPFEM-Modelle und ermöglicht die Simulation industrierelevanter Metallumformungsprozesse zusammen mit ihrer Mikrostruktur. Über ein Optimierungsmodell werden die 4 Parameter pro Gleitsystem des erweiterten Voce'schen Verfestigungsgesetzes für eine EN AW-5754 (AlMg3) Legierung bei mehreren konstant gehaltenen Temperaturen bestimmt, indem Zugversuche simuliert und mit gemessenen Kraft-Weg-Kurven verglichen werden. Weiters wird eine Methode zur Abschätzung der Gleitsystemaktivierung bei Temperaturänderung vorgestellt. Das makroskopische Materialverhalten der untersuchten Legierung wurde durch das Anpassen der Verfestigungsparameter des Mikrostrukturmodells in gute Übereinstimmung mit den Messungen konstanter Temperatur gebracht. Das Ziel, ein Modell für die Simulation temperaturabhängiger industrieller Umformprozesse zu entwickeln, welches von nur wenigen, einfach zu bestimmenden Materialparametern abhängt, wurde erreicht und anhand experimenteller Ergebnisse evaluiert.

Contents

List of Tables

List of Figures

1 Introduction to multiscale Modelling

Simulations in material sciences provide a supporting role for understanding the underlying physical effects in context with the material properties. Furthermore, simulations can help in the development of new parts as well as evaluating the feasibility of new applications for certain alloys. To correctly model a material's behaviour, a theoretical understanding of the processes happening inside is necessary. For metal-forming applications, it is well known that the history of the metal's handling is imprinted on the material, due to the microstructure evolution happening inside. To make reliable material property predictions, both the chemical composition and the microstructure needs to be accounted for [23]. However, for this thesis, a homogeneous distribution of the chemical elements is assumed, as the focus is on the anisotropic behaviour that is the result of the microstructural change due to crystal plasticity. Other, here neglected, processes that can influence the microstructure include recrystallization and phase transformation [23]. While most concepts of microstructural phenomena are formulated within a continuum approach, which are on the mesoscopic length scale in the order of µm, the underlying mechanisms take place on an atomistic level [23]. Table 1.1 provides an overview of the different length scales.

Property	Atomistics	Microstructure	Continuum	Mechanical Part
Length Scale	nm	µm	mm	m

Table 1.1: In multiscale modelling macroscopic properties, microstructure and atomistic processes happen in different length scales. Table after [23].

For solving the multiscale problem in this thesis, two different theories are combined: A mathematical mean-field model for calculating the microstructure evolution of statistical representative grains inside a continuum deformation, that is computed via the Finite Element Method (FEM). On the one hand, FEM gives the capability of obtaining detailed solutions on the mechanics of a deforming solid. On the other hand, Visco-Plastic Self-Consistent (VPSC) model, which is the used mean-field model for the polycrystalline relations, updates the microstructure and provides the resulting anisotropic response to the solid body. This approach has proven to be more suitable for industrial multiscale forming applications, due to the reduced computational resources required, if compared to full-field crystal plasticity (CP) CPFEM-models [1, 16].

Following the motivation and the aim of this thesis in Section 1.1, an explanation of some important quantities and nomenclatures is given in Section 1.2. Starting from the underlying crystallographic structure of a metal in Section 2.1, proceeding to the resulting microstructural properties in Section 2.2 the underlying physical effects in

metal deformations are discussed. The observed macroscopic behaviours of ductile metal aggregates are laid out in Section 2.3. The computational methods are discussed in Section 3 and contain the use of FEM for solving the Partial Differential Equation (PDE) of the solid body deformation problem from Section 2.3.2. Here, also the usage of the program VPSC-FEM with its connection to the FEM-solver LS-DYNA® is explained, together with the conceived method for providing hardening parameters for the thermo-mechanical deformations. Results are presented in Section 4 with a discussion and outlook provided in Section 5.

This thesis was done in cooperation with the numerical simulation group[1] of the Leichtmetallkompetenzzentrum Ranshofen (LKR) GmbH, a subsidiary company of the Austrian Institute of Technology (AIT) GmbH, during an employment of the author. All measurement data and computational equipment was provided by LKR.

1.1 Motivation and Aim of Thesis

This thesis deals with implementing and validating a method for providing temperature-dependent hardening parameters for anisotropic microstructure modelling of a polycrystalline solid body aggregate. The aim is the numerical prediction of changes in the microstructure during thermo-mechanical processing of Al-alloys, considering several slip systems of a certain slip mode at different temperatures. The work done by the author consists of a literature study concerning hardening laws, coding and adapting subroutines in Fortran and the application of the developed code to simulate thermo-mechanical treatment of aluminium alloys.

1.2 Definitions and Nomenclature

Some definitions and nomenclatures are scale independent and are defined preliminary as they are used in the microstructure modelling as well as the macroscopic continuum deformation. This includes the continuum configuration changes discussed in Section 1.2.1, as well as the definitions of stress and strain in Section 1.2.2. Note that throughout this thesis index notation as well as sum convention over double appearing indices are used, with $i, j, k, l, m \in \{1, 2, 3\}$ referring to the three spatial coordinates, if not specifically mentioned otherwise. Furthermore, no difference between co- and contravariant tensors is regarded as an orthonormal basis system is always assumed. Tensors are printed bold in text, with vectors in some images displayed using an arrow to empathize directional behaviour.

1.2.1 Continuum Configuration and Deformation Gradient

The movement of a continuum in space is defined through the reversible, non-linear mapping Equation (1.1),

$$\boldsymbol{x} := \boldsymbol{x}(\boldsymbol{X}, t) \tag{1.1}$$

[1] Link: `https://www.ait.ac.at/en/research-topics/numerical-simulation` (visited on 28/07/2024)

which assigns a material point P, that occupies at the initial moment $t = t_0$ a spatial position given through the position vector $\boldsymbol{X}$, the current configuration position $\boldsymbol{x}$. The initial positions of the material form a reference or original configuration ${}_0\mathrm{C}$ of a volume Ω the body is occupying. A snapshot of the material points taken later in time and give a new configuration for the material points in Ω, denoted by ${}_1\mathrm{C}$ [25, 11]. Inside a fixed orthonormal global coordinate system, this means explicitly for the initial conditions Equation (1.2a) and Equation (1.2b),

$$\boldsymbol{x}(\boldsymbol{X}, t_0) =: \boldsymbol{X} \tag{1.2a}$$

$$\dot{\boldsymbol{x}}(\boldsymbol{X}, t_0) =: \boldsymbol{V}_0(\boldsymbol{X}) \tag{1.2b}$$

where $\boldsymbol{V}_0$ denotes the initial deformation velocity vector at each point. In a continuum deformation, the deformation gradient tensor $\boldsymbol{\mathcal{F}}$ is used to relate a pre-deformation configuration of a solid body to its current one, Equation (1.3) [25, 20].

$$\mathcal{F}_{ij} := \frac{\partial x_i}{\partial X_j} \tag{1.3}$$

Considering $\boldsymbol{u}(\boldsymbol{X}, t)$ giving the deformation vector, also used for the infinitesimal stress and strain tensor definitions in Section 1.2.2, the change of a point from the reference configuration P_0 to the current one P_1 is given by Equation (1.4).

$$\boldsymbol{x}(\boldsymbol{X}, t) = \boldsymbol{u}(\boldsymbol{X}, t) + \boldsymbol{X} \tag{1.4}$$

Plugging Equation (1.4) into Equation (1.3), a connection between the displacement gradient tensor $\boldsymbol{\mathcal{H}}$ to the deformation gradient $\boldsymbol{\mathcal{F}}$ can be derived Equation (1.5),

$$\mathcal{F}_{ij} = \delta_{ij} + \underbrace{\frac{\partial u_i}{\partial X_j}}_{\mathcal{H}_{ij}} \tag{1.5}$$

where again $\boldsymbol{X}$ describes the points in the pre-deformation configuration, $\boldsymbol{x}$ the ones of the deformed, $\boldsymbol{u}(\boldsymbol{X}, t)$ the displacement vector and δ_{ij} the Kronecker delta, noting 1 if $i = j$ and 0 if $i \neq j$ [25]. Figure 1.1 shows a general representation of the above described quantities and their relationships between different continuum configurations that share a common global reference system $\boldsymbol{e}_i^{\mathrm{gl}}$.

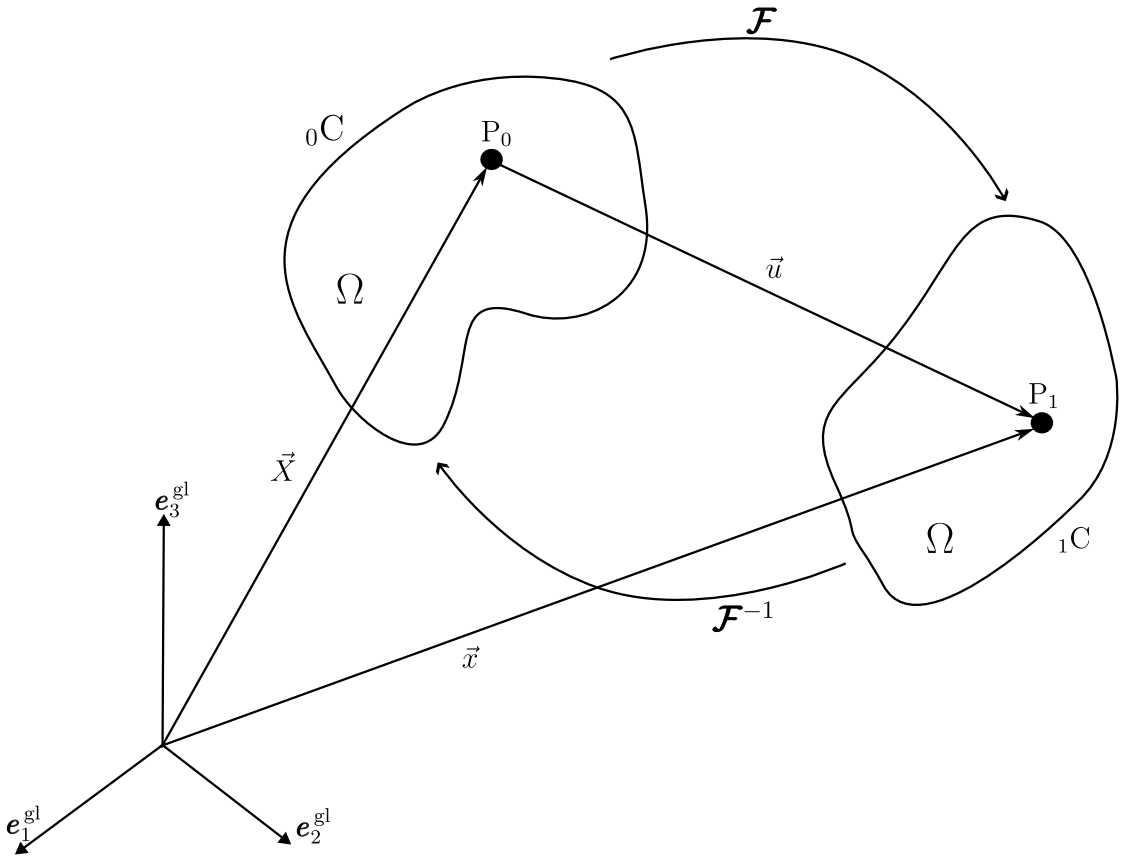

Figure 1.1: Sketch of a deformation of a continuous body

The connections displayed in Figure 1.1 as well as the definitions laid out in Section 1.2.2 are of high importance when dealing with the kinematics of the macroscopic solid body deformation in Section 2.3.2 and the polycrystalline viscoplasticity theory outlined in Section 2.3.1.

1.2.2 Stress, Strain and Strain-Rate

Stress, strain and strain-rate (time derivative of the strain) are the basic quantities used to describe the mechanics of deformation when a body transforms from one configuration to another. Note that the stress and strain tensors are field terms defined for each point in the solid body, using a fixed orthonormal reference frame. The explicit mention of the spatial coordinates is omitted for better readability. The following definitions have been taken and cross validated from [15, 10, 34, 7] to ensure consistency throughout this thesis. Furthermore, the notation of formulae has been adapted where the need arose.

Stress $\boldsymbol{\sigma}$ is the intensity of force $\boldsymbol{F} = (F_x, F_y, F_z)^\top$ at a point $\partial \boldsymbol{A} \to 0$. Because the definition of $\boldsymbol{\sigma}$ contains a force, which is in itself a vector, and an area, nine components

are needed to describe the symmetrical Cauchy stress tensor $\sigma_{ij} = \sigma_{ji}$ as Equation (1.6),

$$\sigma_{ij} := \frac{F_i}{A_j} \tag{1.6}$$

where the indices i, j noting the spatial coordinates $\{x, y, z\}$. If the stress is normal to the area on which it acts, (σ_{xx}, σ_{yy} and σ_{zz}), it is referred to as normal stress, that can be either compressive or tensile. If the force is parallel to the area it acts upon (σ_{yz}, σ_{zx}, σ_{xy},σ_{zy}, σ_{xz} or σ_{yx}), shear stress is observed. Only six independent components σ_{ij} exist, due the symmetry of $\boldsymbol{\sigma}$. Three for the normal and three for the shear stress. To follow usual notation in literature, normal stress components will be noted with just one index $\sigma_{x,y,z}$ and shear stress ones by the letter τ from here on forward.

There always exists a set of three axes 1, 2 and 3, called principal stress axes, along which the shear stresses vanish. The three principal stress components σ_p are defined as the roots $\sigma_1, \sigma_2, \sigma_3$ of the cubic Equation (1.7)

$$\sigma_p^3 - I_1\sigma_p^2 - I_2\sigma_p - I_3 = 0 \tag{1.7}$$

and are normal to the principal stress axes mentioned beforehand. In Equation (1.7) I_1, I_2, I_3 are independent of the orientation of the axes and are therefore called the three invariants of the stress tensor. In terms of the principal stresses, they are described by Equation (1.8).

$$\begin{aligned} I_1 &= \sigma_x + \sigma_y + \sigma_z = \sigma_1 + \sigma_2 + \sigma_3 \\ I_2 &= -(\sigma_x\sigma_y + \sigma_y\sigma_z + \sigma_z\sigma_x) + \tau_{xy}^2 + \tau_{yz}^2 + \tau_{zx}^2 = -(\sigma_1\sigma_2 + \sigma_2\sigma_3 + \sigma_3\sigma_1) \\ I_3 &= \sigma_x\sigma_y\sigma_z + 2\tau_{xy}\tau_{yz}\tau_{zx} - \sigma_x\tau_{zx}^2 - \sigma_y\tau_{zx}^2 - \sigma_z\tau_{xy}^2 = \sigma_1\sigma_2\sigma_3 \end{aligned} \tag{1.8}$$

The linear I_1 and quadratic I_2 invariants have particular physical significance for plasticity.

Another important stress definition is the deviatoric stress tensor $\boldsymbol{\sigma'}$, that is defined using the stress tensor of Equation (1.6) by Equation (1.9),

$$\sigma'_{ij} := \sigma_{ij} - \delta_{ij}\sigma_m \tag{1.9}$$

where δ_{ij}, denotes the Kronecker delta and $\sigma_m = \frac{1}{3}(\sigma_1 + \sigma_2 + \sigma_3)$ is the hydrostatic component of the stress. Note that the components of σ'_{ij} are not independent, as its trace does disappear.

Strain ε or γ is defined in the infinitesimal deformation theory, by the infinitesimal strain $\mathrm{d}\varepsilon = \mathrm{d}l/l$, where the change in length $\mathrm{d}l$ over one dimensional length l within a fixed coordinate system in the material configuration is evaluated. This leads to the natural or true strain ε_t, describing the total deformation amount of the initial, pre-deformation length l_0, by Equation (1.10),

$$\varepsilon_t := \int_{l_0}^{l_1} \mathrm{d}\varepsilon = \ln\left(\frac{l_1}{l_0}\right) \tag{1.10}$$

Conventional engineering strain ε, on the other hand, describes the amount of extension or contraction $\Delta l = l_1 - l_0$ per unit original length or height l_0, Equation (1.11).

$$\varepsilon := \frac{\Delta l}{l_0} \tag{1.11}$$

The material displacement field $\boldsymbol{u}(\boldsymbol{x}, t) = u_i \boldsymbol{e}_i$ gives a deformation vector $\boldsymbol{u}$ at each point $\boldsymbol{x}$ in space at time t, where u_i denotes the directional magnitudes of the deformation and $\boldsymbol{e}_i$ defines an orthonormal reference system for the observer. By assuming infinitesimally small deformations, a symmetrical strain tensor field $\boldsymbol{\varepsilon}$ can be expressed by the components ε_{ij}, giving Equation (1.12).

$$\varepsilon_{ij} := \frac{1}{2}\left(\frac{\partial u_i}{\partial x_j} + \frac{\partial u_j}{\partial x_i}\right) \tag{1.12}$$

Similar to denoting τ for the shear components of the Cauchy stress tensor $\boldsymbol{\sigma}$ in Equation (1.6), the engineering shear strains γ_{ij} can be seen as the six off-diagonal elements of $\boldsymbol{\varepsilon}$. They are explicitly defined by Equation (1.13) under the condition of $i \neq j$.

$$\gamma_{ij} := \frac{\partial u_i}{\partial x_j} + \frac{\partial u_j}{\partial x_i} \tag{1.13}$$

Strain-Rate $\dot{\varepsilon} = \Delta\dot{l}/l_0$ is defined using the time dependent length change $\Delta\dot{l}$ over length l_0 and can be expressed using the gradient of the deformation velocity $\dot{u}_i = \partial u_i/\partial t$, where $u_i = u_i(\boldsymbol{X}, t)$ shall describe the displacement field components of a spatial point $\boldsymbol{X}$ at a time t. The symmetric strain-rate tensor for small strains can be written as Equation (1.14).

$$\dot{\varepsilon}_{ij} = \frac{1}{2}\left(\frac{\partial \dot{u}_i}{\partial x_j} + \frac{\partial \dot{u}_j}{\partial x_i}\right) \tag{1.14}$$

2 Theory of Metal Deformation

The theory section is split into two main parts. While Section 2.2 focuses on the microscopic scale, Section 2.3 establishes a common ground for understanding plastic deformations. Section 2.1 gives a brief introduction into the crystal structure of metals and the definition of material defects, as they are the physical background for metal deformations and texture changes. The order of Section 2.1 to 2.3 is set by going over multiple orders of magnitude, starting from the atomic building blocks of metals leading to the macroscopic deformation theory. In literature, the macroscopic and microscopic length scales are commonly described together, as the theory of deformation and failure is intertwined with the propagation of defects in the material.

Keep in mind that in this thesis, the topic of chemical inhomogeneities, i.e. local changes in the type of atoms, as well as phase changes, are not considered for the plastic deformation calculations. The microstructure from Section 2.2 is treated as anisotropic regarding the orientation of the grain structure, but isotropic regarding the chemical element distribution.

2.1 Underlying Physical Concepts

Atoms are the building blocks of solid matter. Their arrangement and type of binding can lead to different material properties. For metals, the atom arrangements are described by close-packing of equal spheres, which are a result of the strong metallic attraction the atoms experience with each other. This model describes well a wide range of physical material properties, including deformations and material defects. Most metals crystallize either into Hexagonal Close Packed (HCP), Face Centered Cubic (FCC) or Body Centered Cubic (BCC) structures [6]. Typical metals in HCP configuration are zinc, magnesium or cadmium, in BCC alpha iron, vanadium or tungsten and in FCC copper, aluminium or lead [9].

2.1.1 Crystal Structure

Before the atomic structure of materials was known, minerals were described with their flat facets as the outstanding feature. Crystallographers classified the shapes and symmetry of crystals into 32 point groups, or crystal classes, which themselves are based on 7 crystal systems. Namely, cubic, tetragonal, hexagonal, trigonal, triclinic, monoclinic and orthorhombic [6, 7]. The primitive unit cells of the crystal systems are displayed in Figure 2.1, with their lattice constants a, b, c and angles α, β, γ.

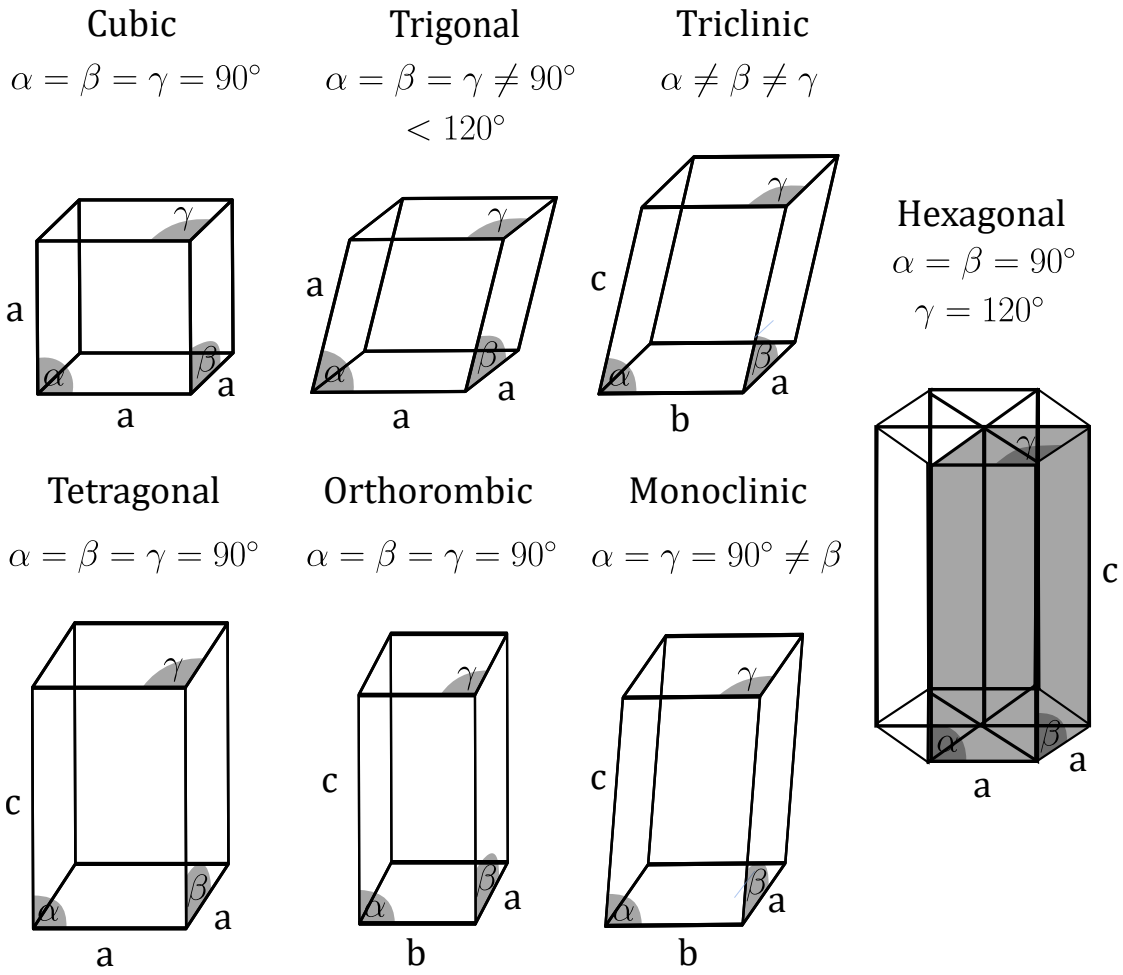

Figure 2.1: Primitive unit cells of the crystal-systems

The modern conception defines an ideal crystal as an infinite, periodic arrangement of structural elements. These structural elements of the lattice are called basis, which can consist either of single atoms or more complex configurations. For a 3D point group, where at least one point is fixed in space, there exist exactly 10 symmetry operations, namely 1, 2, 3, 4 and 6-fold symmetry axes as well as their respective rotary inversion axes, which are a combination of the rotational axes with a centre of inversion. The set of symmetry operations that transform the crystal classes into themselves creates a mathematical group. Assuming the spatial grid not to be bound by any stationary points, the translational symmetry groups, glide mirror planes, screw axes etc., extends the 32 crystal classes to 230 different space groups [7]. Considering symmetry operations, note that the basis does not need to have the full symmetry of the lattice. Taking the basis to be of spherical symmetry, which is the highest one possible, only 14 different space groups, the so-called Bravais lattices, exist [7].

Furthermore, it is important to recognize that due to thermodynamic laws, real crystals

are never perfect. Some atoms will always diverge from their equilibrium positions in larger structures, creating symmetry breaks in the lattice. Defects are normally classified by their dimension. Vacancies and interstitial atoms are point defects, whereas dislocations of lattice atoms are line defects and grain or phase boundaries are said to be of planar form [6]. Point, line and planar defects are briefly discussed with more detail in Section 2.1.1.

Planes and Directions

A plane consisting of multiple lattice points inside the crystal is referred to as a lattice plane. The orientation of such a plane can be classified by the intersections with the crystallographic axes. If these intersections are in the unit of lattice constants, each plane is defined by three numbers, where crystallographically parallel planes are integer multiples of these triples. This leads in crystallography to a reference system where all parallel lattice planes are referred to by using the same triple, namely the Miller indices $(h\,k\,l)$ [7]. Their construction is done by Equation (2.1), where the intercepts of the plane with the cubic crystal axes are measured in multiples m, n and q of the lattice constants of each direction. Have m, n and q, together with their least common multiple r, been determined, the multiplicative inverses $1/m$, $1/n$ and $1/q$ are calculated. By multiplying with r, the Miller indices of a set of parallel planes are found. If no intersection with an axis takes place, i.e. the plane is parallel to a surface plane of the crystal, the respective inverse is set to zero [6].

$$(h\,k\,l) := r \cdot \left[\frac{1}{m}, \frac{1}{n}, \frac{1}{q}\right] \tag{2.1}$$

In some lattices, the before mentioned method of plane identification can lead to different Miller indices for equivalent planes. To address all equivalent planes in a crystal, the notation $\{h\,k\,l\}$ is used instead of $(h\,k\,l)$. In a cubic reference frame, for example, $\{1\,0\,0\}$ would refer to all cubic sides with their respective parallel planes ($(1\,0\,0)$, $(0\,1\,0)$ and $(0\,0\,1)$) even though the sets of Miller indices are not integer multiples from each other [7].

Similar to crystallographic planes, directions in a crystal can also be identified via the Miller indices $[u\,v\,w]$, which are the set of the smallest integer numbers that create the direction vector in reference to the crystal axes. The set of crystallographically equivalent directions are noted by $\langle u\,v\,w\rangle$ [6, 7]. To give a visual example, Figure 2.2 displays the planes $(1\,0\,0)$, $(1\,1\,0)$ and $(1\,1\,1)$ of a cubic crystal structure together with their respective normal vectors $[1\,0\,0]$, $[1\,1\,0]$ and $[1\,1\,1]$ in Miller notation.

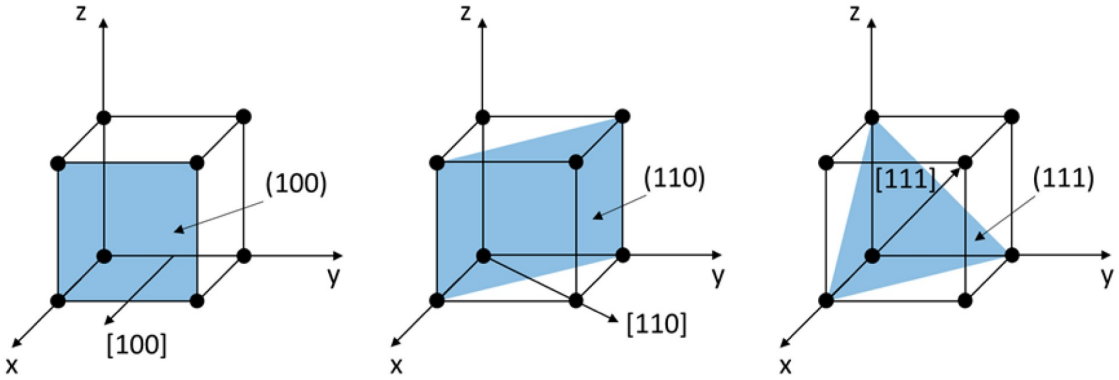

Figure 2.2: "Crystallographic planes" by Ott et al., [24], used under CC BY 4.0.

Structural Defects

Defects in the crystal structure, are formed during crystal growth or introduced by subsequent handling. They are most fundamental and also play an important role in giving metallic materials their respective properties. For example, metals have favourable conditions for many construction and load bearing applications, due to plastic deformation being the result of crystal defect creation and movement through the materials [9, 6]. See Section 2.1.2 on more information.

Impurities are one kind of point defects and include single atoms of a different material being deposited inside a crystal structure of another and are important for solid solution strengthening. Taking them aside, there exist two types of structural point defects: vacancies, as not occupied lattice places, and interstitial atoms. In metals, a vacancy can be thought of as a surface near atoms jumping onto the crystal surface, leaving an empty lattice space that is located inside the crystal through atom movements [6]. Such faults are often thought to be separated by distances in the order of one thousand atomic spacings and extend over volumetric areas of 100 to 1000 atoms [9]. If an atom is moved to an interstitial lattice site, a point defect pair (Frenkel defect) is created. In the near vicinity of a point defect, surrounding atoms are dislocated from their lattice space to adapt for the misplacement [6]. The typical form of line defects, atom misalignments, are commonly referred to as dislocations. Here, faults occur alongside a line where an abrupt discontinuity of the lattice takes place. This can either happen in the form of an edge or screw dislocation and is displayed in Figure 2.3, together with the Burgers vector $\boldsymbol{b}$ and the dislocation line vector $\boldsymbol{L}$, that follows along the line defect. In case of screw dislocations $\boldsymbol{b}$ will be in parallel to $\boldsymbol{L}$ whereas in the case of an edge dislocation $\boldsymbol{b}$ will be normal towards $\boldsymbol{L}$ [7].

The construction of $\boldsymbol{b}$ is done as follows: Are four lines drawn along the grid between the lattice points A, B, C and D (see small upper image in Figure 2.3), they will close when put together, so long as no line defect is present inside the loop. However, if an edge or screw dislocation is present, because the loop was drawn around $\boldsymbol{L}$, the difference needed to close the loop is given by the Burgers vector, as Figure 2.3 shows. By defining

the orientation of the loop, $\boldsymbol{b}$ will not only give the magnitude of the dislocation but also the direction of the misalignment [7].

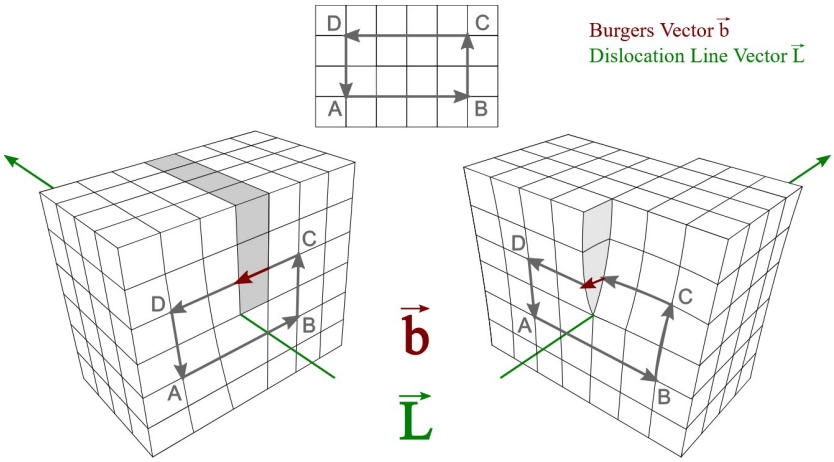

Figure 2.3: "Burgers vector in an edge dislocation (left) and in a screw dislocation (right)" by Martin Fleck, [4], used under CC BY-SA 4.0.

In the most simple case of line defects, the dislocation line will run throughout the whole crystal, from one surface to the other. Due to topological reasons, the dislocation line $\boldsymbol{L}$ can never end inside the crystal. It can only change its direction. However, in such a case, the relative orientation towards $\boldsymbol{b}$ will stay the same. This leads to the possibility of fully closed dislocation lines inside the crystal system [7]. Note, that dislocations are not static and can move, which results in the plastic deformation. The force $\boldsymbol{K}$ on a dislocation defined via its Burgers vector $\boldsymbol{b}$ and dislocation line $\boldsymbol{L}$, under a stress matrix $\boldsymbol{\sigma}$ of Equation (1.6), is given by the Peach-Koehler relation in Equation (2.2) [6].

$$\boldsymbol{K} = (\boldsymbol{\sigma} \cdot \boldsymbol{b}) \times \boldsymbol{L} \tag{2.2}$$

The plane along which a dislocation moves is called a glide or slip plane, with the direction of slip defined using the mentioned Burgers vector $\boldsymbol{b}$, as Section 2.2.2 lays out [6].

Planar defects include grain boundaries and stacking faults. While grain boundaries refer to interfaces between volumes of same crystal orientations and are of high importance in polycrystalline material (see Section 2.1.2 and 2.2.1), stacking faults can change the crystal order [7].

2.1.2 Single versus Poly-Crystals

The discussion of crystal structure in Section 2.1.1 does make it clear that the inner structure is of strong importance for the mechanical behaviour of materials. As a result of solidification from the melt, most solid state materials have a polycrystalline nature. This section shall lay out how single crystals differ from polycrystals. Details

on the microstructure of polycrystalline materials can be described from a mesoscopic perspective and is found in the follow-up Section 2.2. Throughout Section 2.3 the theory of macroscopic plastic deformation is briefly discussed based on the assumption of a homogeneous, ductile continuum without talking about the inner physical structure. However, to fully understand the mechanical properties of metals, the polycrystalline nature of the aggregate still has to be considered.

Single Crystal

In a perfect crystal, the atoms are positioned in equilibrium at their lattice placement within a periodic structure. Following current theory, the cohesive forces binding the atoms together are such that a perfect metal crystal would withstand much greater applied stress than is macroscopically observed. This discrepancy is attributed to faults in the lattice structure, mentioned in Section 2.1.1. Regarding plastic deformation, it is important to understand that dislocations can be seen as quasi-particles moving throughout the crystal as relative displacements of the atoms, which are in the order of 1 or 2 atomic spacings [9].

Should plastic deformations only occur homogeneously, similar to elastic ones, the crystal structure itself would have to change. This does not occur in nature, as it has been verified by X-ray examinations that the crystal structure stays intact during the deformation process. As a result, macroscopic deformations in single crystals can only occur by moving crystal areas by integer multiples along crystallographic planes, named slip- or glide-planes [6, 9] (see Section 2.2.2).

The overall shape change of a sample is the direct result of the positional movement from individual atoms in the underlying crystal structure. During an ongoing deformation, additional dislocations are being freed or created, whose movements result in an overall strain. The macroscopically observed plastic strain being irreversible is attributed to the trapping of dislocations at other faults, which are not mobile under the external stresses. Free dislocations are progressively impeded by the local disordering of the lattice at points where trapped dislocations accumulate. Note that the increase in potential energy of the deformed crystal is only a small fraction of the work being done by the applied stress, as the vast majority appears as vibrational energy of the atoms in or near moving dislocations and is dissipated as heat in the crystal [9].

Polycrystalline Aggregate

A metal, in the commonly used form for structural parts, is a compact aggregate of crystal grains with varying shapes and orientation, where each grain has grown from a separate nucleus and is considered a single crystal by itself [9]. The grain structure, refers to the arrangement of the grains in a metal, with a grain having a particular crystal structure [3], described in the preliminary Section 2.1.1. One important aspect of polycrystalline aggregates is the average size of the grains, as the grain size partly determines the properties of the metal. For example, smaller grain sizes increase the tensile strength and also tend to increase ductility [3].

Another important feature of polycrystalline materials, and the main focus of this thesis, is the orientation of the single crystallites towards the sample axes. While many technical materials may be considered macroscopically isotropic if the orientations of these grains are randomly oriented and their dimensions small compared to the sample as a whole, some material properties are not just simple averages over all grain orientations. This is the case because the single crystals themselves are anisotropic and exhibit directionally dependent behaviour [7, 9]. For example, polycrystalline properties that can to an approximation be seen as averages over the bulk structures, are the coefficient of thermal expansion or the elastic moduli. For the analysis of plasticity this does not necessarily hold, especially if the grains are larger compared to the sample and exhibit ordered orientations [9]. Further differences in behaviour shown by polycrystalline aggregates compared to single crystals are the result of the grain boundaries between the individual crystals, which are usually one to three atom diameters in width [3]. In these transition zones, the atoms take up equilibrium positions between the normal position of the adjacent lattices and have as a result higher free energy than the atom of the connected grains. As a consequence, they are main agents of viscous flow, intercrystalline fracture and are a potential source of dislocation generation but at the same time hindrances to the passage of others. Due to being at the centre of stress concentration, a dislocation arriving at a grain boundary can activate slip on a plane in a neighbouring crystal [9].

A sketch showing a polycrystalline surface and how it refers to the crystal structure from Section 2.1.1 is shown in Figure 2.4 below. The topic of crystallographic slip is discussed in Section 2.2.2.

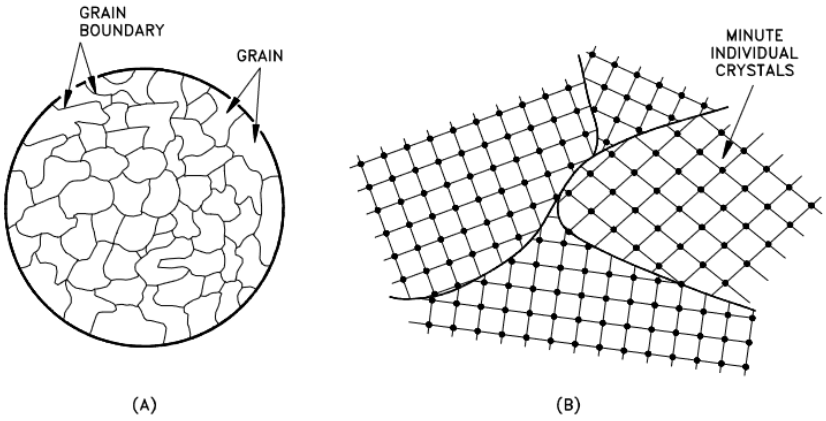

Figure 2.4: "Grain and boundaries (a) Microscopic (b) Atomic" by US Department of Energy, [3]. Public Domain.

Grain boundaries can also have a more direct influence. For example, re-crystallization, that causes movements as well as the creations of new grain boundaries, which leads to the de-hardening of deformed metallic bodies [9, 6]. While phase conversions and re-crystallization are not in the main focus of this thesis and are not discussed further, more information on grain orientations and their respective influence on the mechanical

behaviour of metals, is provided in Section 2.2.1 and 2.2.2.

2.2 Microstructural Material Considerations

Most metals used in load-bearing applications have a polycrystalline structure. This means that the aggregates are composed of a multitude of crystallites, called grains. The crystallographic orientation of these grains refers to how the atomic planes in a volume of crystals are positioned relative to a fixed reference frame and is called texture [26]. A metal may be regarded as macroscopically homogeneous and isotropic when the crystal grains forming the aggregate are distributed with random orientations. However, as a result of being plastically deformed, the individual crystallographic directions of the grains are rotated towards a common axis, producing a preferred orientation. A previously isotropic material of randomly oriented grains has therefore become anisotropic, resulting in its bulk material properties varying with the direction [6]. A preferred grain orientation, in regard to the sample, can be further influenced by thermomechanical processes [26]. Figure 2.5 shows a sketch of how such a preferred orientation might look like on a 2D surface. While in Figure 2.5a the arrangement of the grains is random in a way that no preferred orientation of the metal sample exits, Figure 2.5b shows how grain-oriented structure might develop in the Rolling-Direction of metal sheets [3].

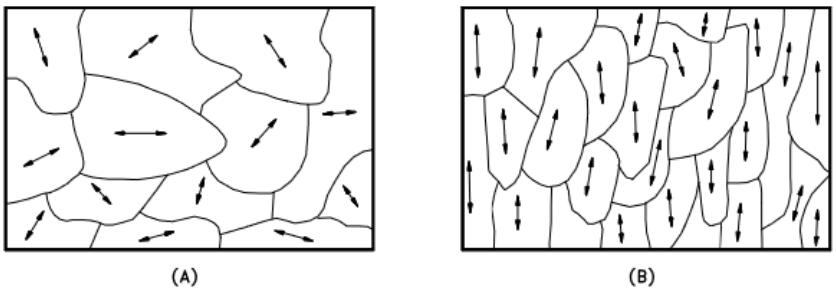

Figure 2.5: "Grain Orientation (a) random (b) preferred" by US Department of Energy, [3]. Public Domain.

Microstructure-level information from a sample might be extracted experimentally via different methods and measurement techniques. Even though the author of this thesis did not perform any experimental measurements personally, one commonly used technique for orientation mapping, Electron Back Scatter Diffraction (EBSD), shall be mentioned here, as this was used to extract texture data used for the simulated sample. EBSD microscopy can establish a direct link between the crystal orientations and the microstructure. Measuring a grain orientation at each grid point allows obtaining a crystallographic map, or texture map [26].

2.2.1 Texture

As mentioned in Section 2.1.2, many material properties in polycrystals are texture specific, ranging from its strength, ductility and toughness to a metal's magnetic permeability and electrical conductivity. While by classical definition a grain has a single distinct orientation, in practice, a grain may vary in a continuous or discontinuous manner, termed orientation perturbation. In particular, perturbations can appear near interfaces and in deformed structures, reflecting the distribution of a strain [26].

To describe the crystal orientation and display a texture map, it was already mentioned that a common global coordinate system must be defined as a reference for all grains in the aggregate, like shown in Figure 2.6 for a cubic crystal symmetry. The colour encoding of such a texture map displaying 3D rotations is commonly done via an Inverse Pole Figure, based on the concepts of stereographic projections and the crystal symmetry of Section 2.1.1. It is shortly described throughout the following paragraphs.

Coordinate systems

Two right-handed Cartesian coordinate systems are required to describe grain orientations in a polycrystal aggregate. While one relates to the crystal, the other one relates to the sample as a whole. The axes of the sample are chosen according to important surfaces or directions associated with the aggregate, which can be seen in Figure 2.6a. Relating to a rolled product, the Rolling-Direction (RD), as the name implies, describes the direction along which the sample was rolled, while the Normal-Direction (ND) relates to the thickness of the sheet metal. The Transverse-Direction (TD) relates to the width of the sheet metal.

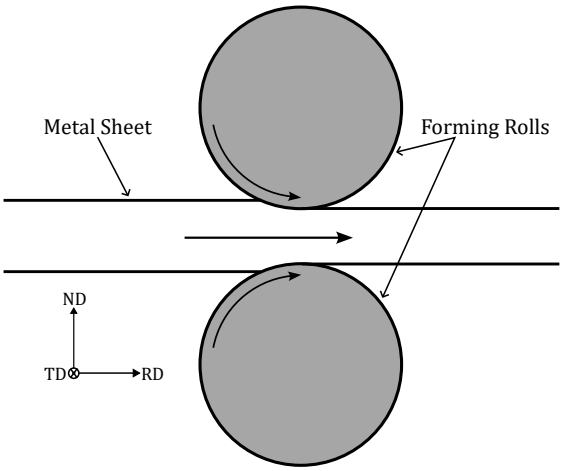

(a) Rolling of a polycrystalline metal sheet.

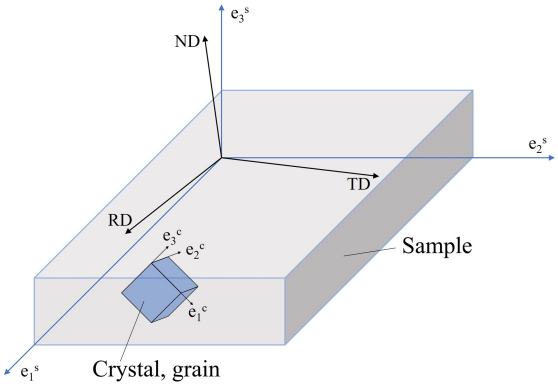

(b) "Coordinate systems of a rolled sheet" by Ott et al., [24], used under CC BY 4.0.

Figure 2.6: Relationship between the sample coordinate system with the spatial axes named Rolling-Direction (RD), Transverse-Direction (TD) and Normal-Direction (ND) to the crystallographic axes of a cubic single crystal.

Note that the displayed reference systems in Figure 2.6 are used throughout this thesis as crystallographic slip, described in Section 2.2.2, occurs in each grain and needs the same cubic crystal axes $\boldsymbol{e}^{\mathrm{c}}_{1,2,3}$, from Figure 2.6b.

In theory, the choice of the reference systems can be arbitrary, likewise to the sample axes $\boldsymbol{e}^{\mathrm{s}}_{1,2,3}$, it is also convenient for the crystal axes to refer to the body it is describing by making use of crystal symmetries. The crystal axes in the grain displayed in Figure 2.6b are specified using the crystal coordinate system, noted by the Miller indices, and may vary whether the metal is either of FCC, BCC (both cubic) or HCP type. In case of cubic symmetry, the indices [1 0 0], [0 1 0], [0 0 1] form an orthogonal frame [26], meaning this can be easily adopted for the use of FCC metals like aluminium. Considering this, the reference systems basis for the sample $\boldsymbol{e}^{\mathrm{s}}_{i}$ and crystal $\boldsymbol{e}^{\mathrm{c}}_{i}$ shall be defined by Equation (2.3a) and Equation (2.3b) respectively.

$$\boldsymbol{e}^{\mathrm{s}}_{1,2,3} := \{\mathrm{RD}, \mathrm{TD}, \mathrm{ND}\} \tag{2.3a}$$

$$\boldsymbol{e}^{\mathrm{c}}_{1,2,3} := \{[1\,0\,0], [0\,1\,0], [0\,0\,1]\} \tag{2.3b}$$

Having the sample and crystal reference systems specified, an orientation can then be defined as the position of the crystal coordinate system basis $\boldsymbol{e}^{\mathrm{c}}_{i}$ with respect to the sample coordinate system $\boldsymbol{e}^{\mathrm{s}}_{i}$ via Equation (2.4),

$$\boldsymbol{e}^{\mathrm{c}}_{i} = R_{ij} \cdot \boldsymbol{e}^{\mathrm{s}}_{j} \tag{2.4}$$

where $\boldsymbol{R}$ denotes the 3D rotation or orientation matrix, transforming from one orthonormal system to the other. Its components R_{ij} are constructed by the cosines of the angles α_{ij} between $\boldsymbol{e}^{\mathrm{c}}_{i}$ and $\boldsymbol{e}^{\mathrm{s}}_{j}$ leading to the rotation matrix Equation (2.5) [26].

$$R_{ij} := \cos \alpha_{ij} \tag{2.5}$$

As the angles α_{ij} of Equation (2.5) are not independent of each other, a reduction of variables can take place. Common rotation descriptor include Rodrigues vectors and Euler angles, with the second one described below [26].

Even though $\boldsymbol{R}$ relates the coordinate systems $\boldsymbol{e}^{\mathrm{s}}_{i}$ and $\boldsymbol{e}^{\mathrm{c}}_{i}$ via Equation (2.5), it is important to note that the specification of these reference systems are not usually unique and a number of solutions to Equation (2.4) might exist, depending on the symmetries for both the sample and the crystal. Considering a crystal of cubic symmetry, like FCC, means that there exist 24 different solutions, due to the number of existing symmetry operations for a cube. The full set of said rotation solutions can be obtained by premultiplying R_{ij} of Equation (2.5) by each of the 24 equivalent orientations. As mentioned, each of the 24 rotations refer to the same orientation, meaning generally any can be chosen to represent the texture. Often the selection of a particular crystallographically related one helps to both facilitate representation and allows for further physical insight into the obtained texture data [26].

Euler Angles and Euler Space

It was mentioned that the rotation matrix Equation (2.5) overdetermines the orientation, as only three independent variables are needed. The most commonly used set of rotations are given in Euler angles, which reside as coordinates in Euler space. The angles refer to three rotations done in sequence. Different notations exist for them, with the most prominent one being in the Bunge convention, formulated by the scientist of the same name [26]. Here, the rotations occur in the following sequence:

1. ϕ_1 rotates around $\boldsymbol{e}_3^{\mathrm{s}}$ (ND), transforming TD and RD to TD' and RD'
2. Φ rotates on the new axis $\boldsymbol{e}_1^{\mathrm{s}}$' (RD')
3. ϕ_2 rotates around $\boldsymbol{e}_3^{\mathrm{s}}$" (ND")

with ϕ_1, ϕ_2 and Φ being the Bunge convention Euler angles. Analytically, these three angles represent the rotation matrices $\boldsymbol{R}^{\phi_1}$ in Equation (2.6a), $\boldsymbol{R}^{\Phi}$ in Equation (2.6c) and $\boldsymbol{R}^{\phi_2}$ in Equation (2.6b) [26].

$$\boldsymbol{R}^{\phi_1} := \begin{pmatrix} \cos\phi_1 & \sin\phi_1 & 0 \\ -\sin\phi_1 & \cos\phi_1 & 0 \\ 0 & 0 & 1 \end{pmatrix} \tag{2.6a}$$

$$\boldsymbol{R}^{\Phi} := \begin{pmatrix} 1 & 0 & 0 \\ 0 & \cos\Phi & \sin\Phi \\ 0 & -\sin\Phi & \cos\Phi \end{pmatrix} \tag{2.6b}$$

$$\boldsymbol{R}^{\phi_2} := \begin{pmatrix} \cos\phi_2 & \sin\phi_2 & 0 \\ -\sin\phi_2 & \cos\phi_2 & 0 \\ 0 & 0 & 1 \end{pmatrix} \tag{2.6c}$$

The rotation matrix $\boldsymbol{R}$ from Equation (2.5) is now linked to ϕ_1, Φ and ϕ_2 by subsequently applying the rotations in Equation (2.6) as Equation (2.7) shows [26].

$$\boldsymbol{R} = \boldsymbol{R}^{\phi_2} \cdot \boldsymbol{R}^{\Phi} \cdot \boldsymbol{R}^{\phi_1} \tag{2.7}$$

Stereographic Projection and Inverse Pole Figures

The orientation of any 3D vector in a crystal, like a crystallographic direction or a plane normal, can be described as a point on the unit reference sphere. Provided that the sphere is attached to an external reference frame, the position of the pole on the sphere also provides information on the crystallographic orientation, even though, the crystal will still have one degree of freedom left. It can still rotate around its own axis [26]. The representation of the unit sphere into a 2D plane can be done via a stereographic, equal-area or a gnomonic projection. Note that this thesis will work with the first type of projection, as this is the one most commonly used in crystallography and metallurgy alike, as it preserves the angular relationships in the crystal. The main application of

such projections in texture analysis lies in the creation of Pole Figure (PF) and Inverse Pole Figure (IPF) maps, respectively [34, 26].

A crystal can be represented by a set of normals to their respective crystallographic plane. To create a stereographic projection for representing a 3D angular relationship on a plane, first a crystal of set symmetry is put in the origin of the unit sphere that circumscribes it. Next, the plane normals in the crystal intersect the sphere at specific points, called poles, and form a spherical projection, leading to the symmetry of the crystal itself being carried onto said sphere. In particular, this means that the respective reference sphere is being divided by the crystal symmetry planes into spherical triangles. As implied, the amount of the so-called spherical unit triangles depends on the type of crystal and may vary between 48, 24 and 8 for cubic, hexagonal and orthorhombic systems, respectively. For a final step, to create a 2D representation, the spherical poles are projected from the south pole of the unit sphere onto the bottom plane, creating the stereographic projection from one half of the sphere for the PF. The axes of PFs are typically taken to be of the polycrystalline aggregate $\boldsymbol{e}^{\mathrm{s}}_{1,2,3}$, e.g. RD,ND,TD, as predefined poles of multiple crystals are plotted together [26].

The stereographic projection of the cubic planes onto the surface seen in Figure 2.7, can be accomplished by calculating the 2D coordinates pairs (X, Y) of the cubic crystal planes $\{1\,0\,0\}$ and $\{1\,1\,1\}$, using the projection formulae Equation (2.8),

$$(X, Y) := \left(\frac{x}{z+1}, \frac{y}{z+1} \right) \tag{2.8}$$

that use the Cartesian coordinate set (x, y, z). Figure 2.7 displays a stereographic projection for a cubic symmetry, containing an inlay for a typical IPF colour encoding.

It is often more favourable to use IPF texture maps instead of representing the crystal orientation in the specimen system by a PF. They give the reverse relationship by projecting one of the sample axes $\boldsymbol{e}^{\mathrm{s}}_i$ to the crystal $\boldsymbol{e}^{\mathrm{c}}_i$. This leads to the texture as an orientation of RD, ND or TD being displayed in reference to a local grain's crystal planes, e.g. $(1\,1\,1)$, $(1\,0\,1)$ and $(0\,0\,1)$ via a colouring. The rotation matrix R_{ij} is then defined in terms of the sample axe's orientation [26]. Figure 2.7 shows the stereographic triangles created by the crystallographic planes projected through Equation (2.8) onto the $\boldsymbol{e}^{\mathrm{c}}_1$-$\boldsymbol{e}^{\mathrm{c}}_2$ plane.

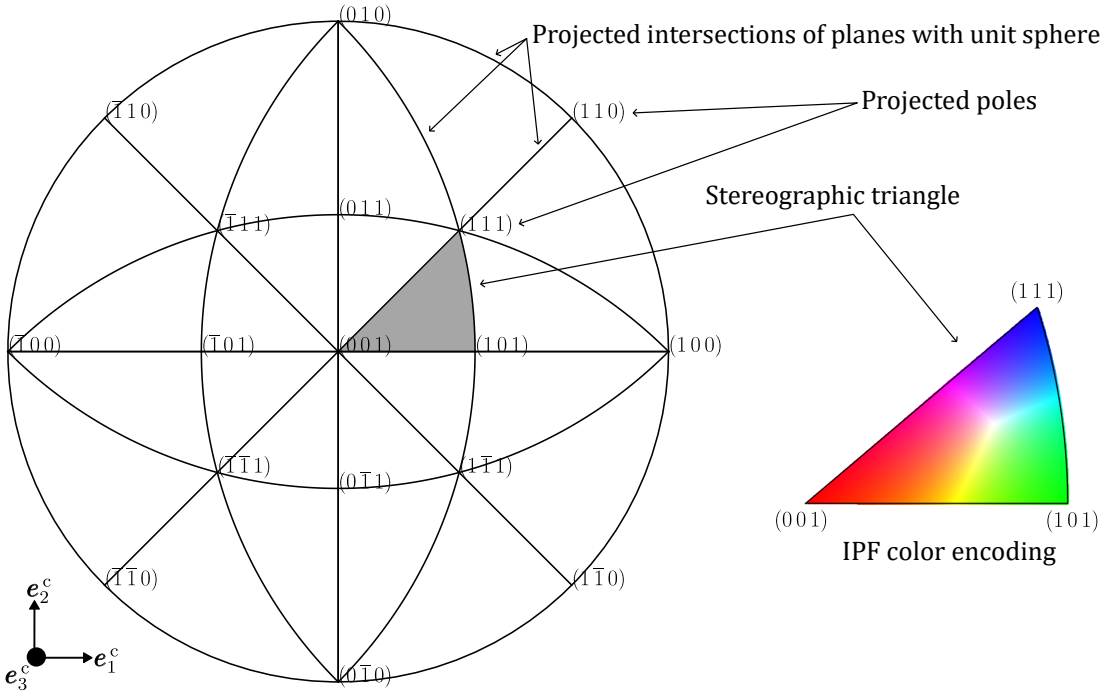

Figure 2.7: Stereographic triangles of cubic crystal planes projected, with an IPF colour encoding, for projected sample axes onto the local crystals (1 1 1), (1 0 1) and (0 0 1) planes.

2.2.2 Microstructure Evolution and Slip Systems

During the deformation of the polycrystalline aggregate, each grain will be affected by its neighbours via interactions taking place across the grain boundaries. If adjacent grains exhibit different crystallographic and morphologic rotation trends, it can be expected that local stresses induced at grain boundaries will affect the slip activity inside the grain [34]. Further, note that grains oriented crystallographically favourable for deformation undergo plastic deformation under load, which forces grains that are less favourably oriented to carry a higher stress [8].

Section 2.2.2 and 2.1.2 established that plastic deformation of crystalline materials occurs by atoms gliding along each other, keeping the crystal structure intact. Should slip only occur on part of the plane, as a result from movement of dislocations through the lattice, a boundary between the slipped and not slipped portions, which is called a dislocation line, remains [10]. This means that the direction of dislocation movement is defined by a set of crystallographic parallel planes and directions, called slip system. To follow the nomenclature of [34] in this thesis, a set of crystallographic equivalent slip systems (e.g. the 12 FCC slip systems $\{1\,1\,1\}\langle 1\,\bar{1}\,0\rangle$ in Table 2.1) will be referred to as a slip mode henceforth. Slip planes usually consist of the most densely packed atomic planes in the crystal lattice, with the directions of slip being the crystallographic directions with the shortest distance between like atoms [10]. The most densely packed atomic planes

and directions are listed in Table 2.1 for Face Centered Cubic, Body Centered Cubic and Hexagonal Close Packed crystals. The amount of slip systems per mode is calculated by multiplying the number of slip directions with the number of non-parallel planes [6].

crystal	slip plane	slip direction	non-parallel planes	slip directions per plane	slip systems
FCC	$\{1\,1\,1\}$	$\langle 1\,\bar{1}\,0\rangle$	4	3	12
BCC	$\{1\,1\,0\}$	$\langle \bar{1}\,1\,1\rangle$	6	2	12
	$\{1\,1\,2\}$	$\langle 1\,1\,\bar{1}\rangle$	12	1	12
	$\{1\,2\,3\}$	$\langle 1\,1\,\bar{1}\rangle$	24	1	24
HCP	$\{0\,0\,0\,1\}$	$\langle 1\,1\,\bar{2}\,0\rangle$	1	3	3
	$\{1\,0\,\bar{1}\,0\}$	$\langle 1\,1\,\bar{2}\,0\rangle$	3	1	3
	$\{1\,0\,\bar{1}\,1\}$	$\langle 1\,1\,\bar{2}\,0\rangle$	6	1	6
	$\{1\,1\,\bar{2}\,2\}$	$\langle \bar{2}\,1\,1\,3\rangle$	6	2	12

Table 2.1: Slip modes consisting of the most densely packed planes and directions with the shortest atom distances for Face Centered Cubic (FCC), Body Centered Cubic (BCC) and Hexagonal Close Packed (HCP) crystal structures. Table after [6].

Reference Systems for Slip

In order to be able to assess, if a certain slip system in the crystal is active under an applied load, the stress influence on a said slip system needs to be calculated and compared to the threshold value needed to get the dislocations moving. As was mentioned before, a slip system is defined via a direction of slip and the plane the slip occurs along. The slip direction of the dislocation movement aligns with the Burgers vector $\boldsymbol{b}$, which also gives the magnitude of the slip. The slip plane, on which the dislocation movement happens, is defined through the plane normal $\boldsymbol{n}$, in the crystal reference system $\boldsymbol{e}_i^{\mathrm{c}}$. This means a reference system for the complete slip system $\boldsymbol{e}_i^{\mathrm{sl}}$ is defined by Equation (2.9),

$$\boldsymbol{e}_{1,2}^{\mathrm{sl}} := \left\{ \frac{\boldsymbol{b}}{|\boldsymbol{b}|}, \boldsymbol{n} \right\} \tag{2.9}$$

where $\boldsymbol{e}_3^{\mathrm{sl}}$ completes the orthonormal basis. Now, the orientation of the slip system in reference to the crystal axes is applicable, allowing for transforming tensorial quantities like the stress σ_{ij}^c Equation (1.6) and strain ε_{ij}^c Equation (1.12) into the slip system sl. This is shown in Equation (2.10) for calculating the Resolved Shear Stress (RSS) τ^{sl} and gives the Schmid-tensor m_{ij} as a basis transformation [34]. As Section 1.2.2 explains, the shear stress components in the stress tensor are commonly referred to via the letter τ. Note sum convention and index notation.

$$\tau^{\mathrm{sl}} := \sigma_{12}^{\mathrm{sl}} = \underbrace{\frac{1}{2}(b_i n_j + b_j n_i)}_{m_{ij}} \sigma_{ij}^c \tag{2.10}$$

Figure 2.8 shows a graphical representation of the above-mentioned procedure of the basis transformation for the stress tensor in the single crystal reference system. Note, in a polycrystalline material, many single grains are available in the aggregate, each one experiencing a different stress tensor, dependent on its position in the sample geometry and the direction of load. Refer to Section 3 for further information.

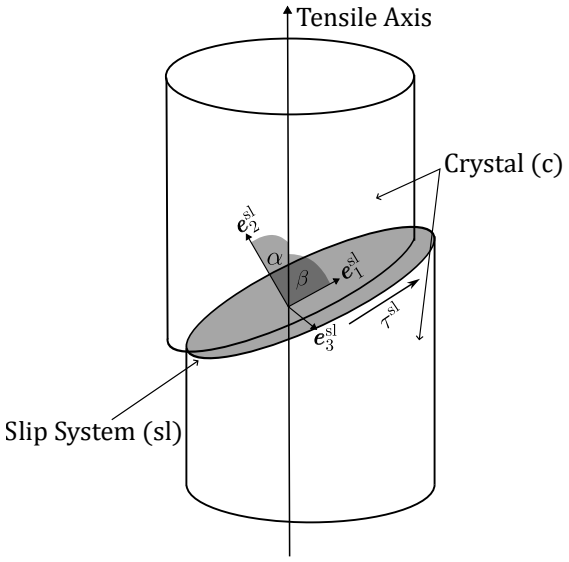

Figure 2.8: Slip system inside a single crystal.

Should only σ_{33}^c be non-zero, Equation (2.10) reduces to the well known form Equation (2.11) by directly referring to the angles α, β between $\boldsymbol{n}$, $\boldsymbol{b}$ and the tensile axis respectively. The product of $\cos\alpha\cos\beta$ is also sometimes referred to as the Schmid factor [10, 35].

$$\tau^{\mathrm{sl}} = \sigma_{33}^c \cos\alpha \cos\beta \tag{2.11}$$

Note that in most crystals, slip occurs with equal ease forward or backward, meaning $\pm\tau^{\mathrm{sl}}$ are equally likely to initiate a dislocation movement. An exception being BCC, where the stress required to cause slip in one direction is less than that for the opposite direction [10]. Another important property of the Schmid tensor derives from the normality between $\boldsymbol{b}$ and $\boldsymbol{n}$, as this defines the trace of the Schmid's tensor to be zero, which leads to the plastic strain associated with dislocation being incompressible [34].

To find out if a stress on a crystal initiates a dislocation movement in a slip system (sl), the RSS τ^{sl} needs to be compared with a threshold value, the Critical Resolved Shear Stress (CRSS) $\hat{\tau}^{\mathrm{sl}}$, as mentioned. This critical condition required to accommodate plastic deformation by activation of dislocation glide is given by the Schmid law Equation (2.12),

$$\text{slip system is } \begin{cases} \text{active}, & \text{if } \tau^{\mathrm{sl}} = \hat{\tau}^{\mathrm{sl}} \\ \text{in-active}, & \text{if } \tau^{\mathrm{sl}} < \hat{\tau}^{\mathrm{sl}} \end{cases} \tag{2.12}$$

with the case $\tau^{\mathrm{sl}} > \hat{\tau}^{\mathrm{sl}}$ being impossible as $\hat{\tau}^{\mathrm{sl}}$ is the maximal possible shear stress on the current slip system [34].

Other Influences

The above paragraphs in Section 2.2.2 have only talked about crystallographic slip, as this is the predominant process for plastically deforming metals and the one this thesis is focusing on. Nonetheless, it has to be noted that there also exist other possibilities of plastic deformation which also preserve the crystal structure. Namely, shape changes through diffusion and mechanical twinning. While diffusion plays an important part in high temperature creep, twinning is often of special importance at low temperatures [6]. The investigated polycrystalline aluminium alloy in this thesis is deformed in a more moderate temperature range and at low strain-rates. As a result of high stacking fault energy, deformation twinning rarely occurs in polycrystalline and single crystalline aluminium [41]. No further explanation of these effects shall be given here. Non-Schmid effects for slip that are the result of atomistic effects and important for BCC materials [31, 39] are neglected in this thesis as well.

2.2.3 Hardening on the Microscopic Scale

The increase of a material's resistance towards further deformation at increasing internal strain, as the macroscopically observed strain- or work-hardening is the result of internal dislocation accumulation. Referring to Section 1.2.2 σ and ε shall denote a one dimensional stress and strain. Strain-hardening is divided into 4 different stages [27]:

Stage I describes that single crystals of close packed metals will deform on a single slip system with little strain-hardening [27]. Experimentally it has been shown by Fourie and Murphy in [5], that at a small but finite hardening-rate $\frac{\mathrm{d}\sigma}{\mathrm{d}\varepsilon}$, an accumulation of dislocation line length occurs, with the predominant storage mechanism being dislocation dipoles. The first hardening stage is caused by storage of these dislocation dipoles as well as multipoles on the primary slip system (see Table 2.1) and known as easy glide, due to the fact that large amounts of strain can accumulate without much hardening taking place. The term CRSS here directly refers to the Schmid law Equation (2.12) and Schmid factor Equation (2.11) for modelling, if dislocation movement in a slip system happens. After a certain amount of strain, single crystals transition from a low hardening-rate to a much larger one, entering the second stage of work-hardening, as dislocation activity on secondary systems has started [27].

Stage II was first characterized by an approximately linear stress-strain curve being observed in the strain-hardening region of the stress-strain curve (see Figure 2.10), but was later redefined as athermal hardening, through the high strain-hardening-rate, caused by storage of dislocation tangles on multiple slip systems. It exhibits a self-similar scaling behaviour of the dislocation substructure [27]. Note, that the hardening-rate here only has a mild dependence on the strain-rate and temperature. However, it might vary by a

factor of 2 with the single crystal orientation. Furthermore, it is important to note that this high hardening-rate can still occur while a single slip system is supplying the imposed strain, which means that a grain can be hardening in stage II, even while still deforming macroscopically by single slip [27]. Athermal hardening also occurs in tensile tests of $\langle 1\,1\,1 \rangle$ oriented single crystals which deform on 6 slip systems, in $\langle 1\,0\,0 \rangle$ single crystals which deform on 8 slip systems and in polycrystals, where at least 5 independent slip systems must be active in order to accommodate the imposed arbitrary strain [27]. The work-hardening-rate in stage II is essentially constant, with common theory describing it by assuming the line length of stored dislocations per unit strain being proportional to the reciprocal of the mean free path between existing dislocations [27].

Stage III is observed by a parabolic characteristic in the stress-strain curve that is the result of a monotonically decreasing hardening-rate at increasing flow stress, until a saturation stress, where no net-hardening occurs, is reached. In contrast to the athermal hardening stage, stage III is highly temperature and slightly strain-rate sensitive. It is associated with dynamic recovery, meaning the recovery or loss of dislocation line length during plastic straining [27]. Due to the dynamic recovery, which is caused by the reduction of the dislocation line length during straining, the hardening-rate gets lowered. In polycrystalline aluminium at room temperature, stage III is the only observable stage of strain-hardening, with the second stage being observed at lower temperatures [27].

Stage IV is caused by the accumulation of dislocation debris, which can be thought of as a by-product of dynamic recovery and is associated with large strain-hardening. The classical large strain metal working process is rolling of sheets [27] (see Figure 2.6a). Note, that while the onset of instabilities commonly observed at larger strain generally results in a reduced load carrying capacity of the plastically deformed material, the fourth hardening stage clearly increases the load bearing capacity. This is due to the fact that large strain-hardening occurs without significant changes to the dislocation movement's obstacles, the transition of the strain-rate sensitivity from the third hardening stage to the fourth is a smooth function of the flow stress [27].

To calculate the strain-hardening, that is observed for the macroscopic length scale in Section 2.3.3, a model giving the Critical Resolved Shear Stress (CRSS) for each slip system as an incremental function of the applied shear in the crystal is needed. This CRSS can then be compared with the Resolved Shear Stress (RSS) calculated via Schmid's tensor Equation (2.10), for evaluating if a slip system is still active at a higher internal strain by Schmid's law Equation (2.12). The most physical approach, for describing the above-mentioned stages, is by directly tracking the dislocation behaviour in the material [27, 34]. Here, the resistance of the four hardening stages are directly referred to by four explicit additions to the CRSS, regarding their different barrier mechanisms. The advantage of this kind of modelling the strain-hardening is that it accounts explicitly for the thermal activation of the dislocations, as well as the dependence of the yield stress on strain rate and temperature. This direct approach has been successfully applied to a wide range of

materials (Mg, Be, Zr, Ti, Al etc.) [34] and is usable for high strain-rate and temperatures. For example, a dislocation based hardening model been used for FEM-coupled impact deformations calculations at high temperatures by Zecevic and Knezevic in [39], giving accurate results for the predicted flow stress at high magnitudes. However, such models need multiple fitting parameters, e.g. for dislocation interaction and annihilation, requiring extensive experimental trials. This, and the thereby required focus on a single material, alloy and heat treatment state, reduces the model versatility markedly.

Voce hardening law

The phenomenological Voce hardening law, named after the researcher that first described it in [38], as [37] mentions, is used in this thesis to model microscopic hardening and calculate the CRSS. Following, a sketch of the derivation for the three parameter Voce hardening law is shown, which is based on the book chapter by Tomé et al. [34] of page 111 and following. The underlying concept here is that the dislocation density rate is the sum of a storage and annihilation term of the dislocations. On the one hand, it is assumed that the storage is inversely proportional to the mean free path of the dislocations before they get stopped and stored (refer to stage II hardening). This mean free path itself is taken to be inversely proportional to the square root of the dislocation density ϱ. On the other hand, the annihilation of the dislocations is taken to be directly proportional to the density of the dislocations and to increase with the accumulated plastic deformations until a steady state between the storage and annihilation of dislocation is reached. This means no net-hardening will take place any more, reaching stage III hardening, which leads to the dislocation density evolution Equation (2.13) by a plastic strain ε,

$$\frac{\mathrm{d}\varrho}{\mathrm{d}\varepsilon} = k_1\sqrt{\varrho} - k_2\rho \tag{2.13}$$

where k_1 and k_2 denote proportionality constants. Under the so-called Taylor-law Equation (2.14), the yield stress σ is proportional to the mean free path between dislocations [34]. In Equation (2.14) σ_0 denotes an initial stress, μ the shear modulus and α a constant. Note, the Taylor-law holds over a wide range of dislocation densities ϱ with values of α being between 0.5 to 1.0 and conceals much of the inherent complexity of detailed dislocation theory [27].

$$\sigma = \sigma_0 + \alpha\mu b\sqrt{\varrho} \tag{2.14}$$

Equation (2.14) leads to Equation (2.15a) and calculating $\mathrm{d}\varrho/\mathrm{d}\varepsilon$ by considering $\sigma = \sigma(\varepsilon)$ results in Equation (2.15b) [34].

$$\varrho = \left(\frac{\sigma - \sigma_0}{\alpha\mu b}\right)^2 \tag{2.15a}$$

$$\frac{\mathrm{d}\varrho}{\mathrm{d}\varepsilon} = \frac{2(\sigma - \sigma_0)}{(\alpha\mu b)^2}\frac{\mathrm{d}\sigma}{\mathrm{d}\varepsilon} \tag{2.15b}$$

Placing the derivations of Equation (2.15) into the assumptions of Equation (2.13) results in a differential equation for the hardening rate by describing the evolution of the flow

stress σ with plastic strain ε Equation (2.16)

$$\frac{\mathrm{d}\sigma}{\mathrm{d}\varepsilon} = k_1 \frac{\alpha\mu b}{2} - k_2 \frac{\sigma - \sigma_0}{2} = k_1' - k_2'\sigma \tag{2.16}$$

where k_1' and k_2' denote the so-called Kocks-Mecking parameters. The differential Equation (2.16) can be solved by using the exponential ansatz. After setting as boundary conditions an initial yield stress $\sigma|_{\varepsilon=0} = \sigma_0$, an initial hardening-rate $\frac{\sigma}{d\varepsilon}|_{\varepsilon=0} = \Theta_0$ and a saturation stress $\sigma|_{\varepsilon=\mathrm{inf}} = \sigma_0 + \sigma_1$, the three parameter hardening law Equation (2.17) is obtained [34].

$$\sigma(\varepsilon) = \sigma_0 + \sigma_1 \left(1 - \exp\left(-\varepsilon \frac{\Theta_0}{\sigma_1}\right)\right) \tag{2.17}$$

This Voce hardening law Equation (2.17) now gives the flow stress σ as a function of accumulated strain ε. An extension to the three parameter hardening law Equation (2.17) was proposed by Tomé et al. in [35], called the extended Voce law, that is assumed to apply to the hardening of each individual slip system (sl). It includes an additional parameter to account for the sustained hardening in stage IV for large strains, rather than simple saturation [34, 35]. Equation (2.18) is characterized by an evolution of the threshold stress $\hat{\tau}^{\mathrm{sl}}$ (CRSS) with accumulated shear strain γ^{sl} in each grain,

$$\hat{\tau}^{\mathrm{sl}} = \tau_0^{\mathrm{sl}} + \left(\tau_1^{\mathrm{sl}} + \Theta_1^{\mathrm{sl}}\Gamma\right)\left[1 - \exp\left(-\Gamma\left|\frac{\Theta_0^{\mathrm{sl}}}{\tau_1^{\mathrm{sl}}}\right|\right)\right] \tag{2.18}$$

where $\Gamma = \sum_{\mathrm{sl}} |\gamma^{\mathrm{sl}}|$ is accumulated shear in the grain, τ_0^{sl} the initial threshold stress, Θ_0^{sl} the initial-, Θ_1^{sl} the asymptotic-hardening-rate and $\tau_0^{\mathrm{sl}} + \tau_1^{\mathrm{sl}}$ the back-extrapolated flow stress. The extended Voce law reduces to Equation (2.17) in case of $\Theta_1^{\mathrm{sl}} = 0$ [34].

Considering the possibility of self and latent hardening, a coupling coefficient $h^{\mathrm{sl,sl'}}$ empirically accounts for the obstacles that the dislocations in a slip system sl' pose to the ones in slip system sl. The increase of the threshold stress $\Delta\bar{\tau}^{\mathrm{sl}}$, due to shear activity $\Delta\gamma^{\mathrm{sl'}}$, can be calculated incrementally by Equation (2.19),

$$\Delta\bar{\tau}^{\mathrm{sl}} := \frac{\mathrm{d}\hat{\tau}^{\mathrm{sl}}}{\mathrm{d}\Gamma} \sum_{\mathrm{sl'}} h^{\mathrm{sl,sl'}} |\Delta\gamma^{\mathrm{sl'}}| \tag{2.19}$$

where $\mathrm{d}\hat{\tau}^{\mathrm{sl}}/\mathrm{d}\Gamma$ is given by the derivative of Equation (2.18). A conventional hardening response for a slip system is observed for $\tau_0^{\mathrm{sl}} > 0$, $\tau_1 \geq 0$ and $\Theta_0 \geq \Theta_1 \geq 0$, which means an increasing flow stress at decreasing hardening-rate, tending to linear saturation. An example on how conventional hardening for a slip system described by Equation (2.18) might look is provided in Figure 2.9 [34].

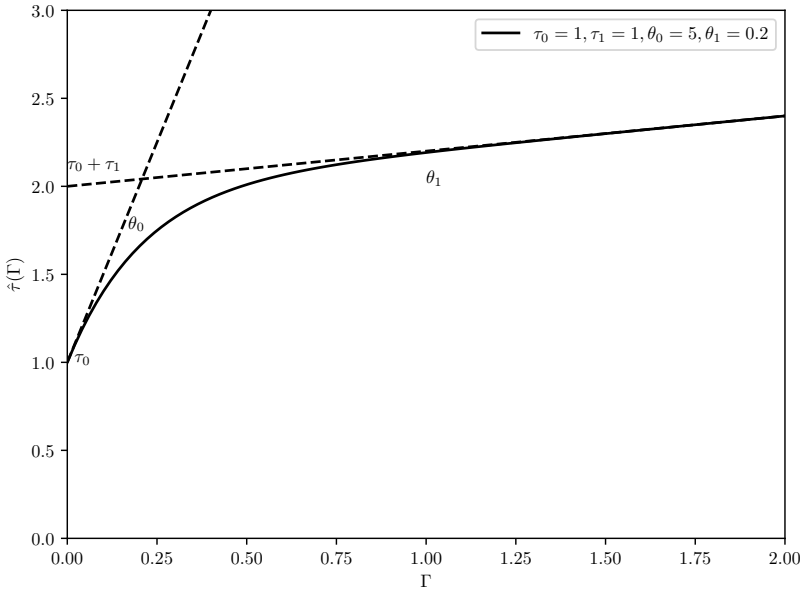

Figure 2.9: Conventional hardening example of extended Voce hardening law. The evolution of the threshold stress $\hat{\tau}$ in a slip system is given as a function of the accumulated shear Γ in the grain.

One advantage of the extended Voce hardening is that it gives a straightforward connection between the macroscopically observed hardening in a stress-strain curve and slip systems. For polycrystalline materials, the overall hardening that occurs can be defined as a weighted average over all grains [34].

2.3 Macrostructural Material Considerations

The mechanical behaviour of materials encompasses the response of materials to external forces in general. This includes mechanical testing to determine material properties as well as plasticity and the treatment of several modes of failure [10]. Theory of plasticity is the name given to the mathematical study of stress and strain in plastically deformed metal solids under constant strain-rates. For handling time-dependent aspects, i.e. non-constant strain rates, a generalization of the plastic theory within the strain-rate-sensitive range, called viscoplasticity, can be used [15]. In the following Section 2.3.1, a dive into the topic of polycrystalline viscoplasticity with the Visco-Plastic Self-Consistent (VPSC)-approach is provided, that is used as the material model for the solid deformation calculations of the sample in Section 2.3.2. This model, based on self-consistent homogenization of single-crystal viscoplastic behaviour, is used to provide a texture-sensitive material response inside the solid body deformation boundary problem solved by Finite Element Method (FEM) by giving the polycrystalline relationship between stress and the corresponding plastic strain-rate response [28].

The stress-strain relation, that can be macroscopically obtained via a tensile test of a sample or read-out from the sample deformation simulation, is explained in Section 2.3.3.

2.3.1 Polycrystalline Viscoplasticity Model

The model used in this thesis for calculating viscoplastic stress-strain-relations of polycrystalline metals is the VPSC approach, that was numerically implemented by Lebensohn and Tomé in [18], which is based on the principles of Visco-Plastic Self-Consistent theory for polycrystal deformation developed by Molinari et al. in [22] (Lebensohn et al. [17]). In the underlying assumption, VPSC treats each grain as an inhomogeneity inside a Homogeneous Effective Medium (HEM). This leads to a linear interaction equation to relate stress and strain rate in the grain with the overall stress and strain of the HEM [18]. Due to the local position of the grains being neglected in VPSC, the geometry of the polycrystalline aggregate is not regarded. To address this, Seguardo et al. [28] extended the approach into a material model for use in solid body FEM deformation calculation. Later adaptations, made by Zecevic et al. [39], even allow for the use in high-strain-rate deformations, which was verified for impact simulations of tantalum. In the mesoscopic VPSC approach for use in FEM, a polycrystal is being defined at each of the solid body's material points [28]. For detailed technical information, on how this model interacts with the FEM calculations, see Section 3.3.

The VPSC model allows for predicting texture development for arbitrary deformations of crystalline materials. As mentioned, it calculates active deformation modes present in each grain independently of one another by only evaluating their active contribution to the overall material behaviour [18]. Mathematically, this mean-field polycrystalline model, describes the microstructure evolution by imposing a velocity gradient $\boldsymbol{\mathcal{L}}$ over the HEM representing a polycrystal. Following, an induced velocity gradient over each grain is calculated. Note, the grains themselves are not defined at an atomistic crystal level, but at a mesoscopic scale, by a weighted, ellipsoid with varying orientation and shape inside the HEM [34]. A detailed mathematical outlay about the theory on VPSC is provided in the book by Tomé et al. [34]. The following paragraphs contain the important constitutive relations for using the adapted VPSC approach of [28] as a material model for the viscoplastic stress-strain relations of a solid body deformation provided by the theory in Section 2.3.2.

Viscoplastic Relations

VPSC implies that the single-crystal relations in the polycrystal can be expressed in terms of the Cauchy deviatory stress tensor $\boldsymbol{\sigma}'$ and the viscoplastic strain rate $\dot{\boldsymbol{\varepsilon}}_{\mathrm{vp}}$. By considering a grain at each material point $\boldsymbol{x}$ of the polycrystal, the rate sensitive approach of crystal plasticity gives Equation (2.20) for the non-linear relation between $\dot{\boldsymbol{\varepsilon}}_{\mathrm{vp}}$ and $\boldsymbol{\sigma}'$. The sum in Equation (2.20) runs over all N_{sl} slip systems (sl) from all slip modes, where $\boldsymbol{m}^{\mathrm{sl}}$ is the Schmid tensor and $\dot{\gamma}^{\mathrm{sl}}$ the local shear rate of the corresponding the slip

system [28].

$$\dot{\boldsymbol{\varepsilon}}_{\mathrm{vp}}(\boldsymbol{x}) := \sum_{\mathrm{sl}=1}^{N_{\mathrm{sl}}} \boldsymbol{m}^{\mathrm{sl}}(\boldsymbol{x}) \dot{\gamma}^{\mathrm{sl}}(\boldsymbol{x}) \tag{2.20}$$

Equation (2.20) can be extended to the explicit form of Equation (2.21a), by the CRSS $\bar{\tau}^{\mathrm{sl}} := \sum \Delta \bar{\tau}^{\mathrm{sl}}$ incrementally calculated from Equation (2.19), a normalization factor $\dot{\gamma}_0$ and the so-called rate-sensitivity exponent n. The conditions of Equation (2.21b) for a $\mathcal{X} \in \mathbb{R}$ denote the sign function, to take the polarity of the mechanisms into account [28, 34]. Note, that Equation (2.21a) would also consider all the mechanical twinning systems, however as mentioned in Section (2.2.2) [28], they are neglected as a deformation mode for the simulations in this thesis.

$$\dot{\boldsymbol{\varepsilon}}_{\mathrm{vp}}(\boldsymbol{x}) = \dot{\gamma}_0 \sum_{\mathrm{sl}=1}^{N_{\mathrm{sl}}} \boldsymbol{m}^{\mathrm{sl}}(\boldsymbol{x}) \left(\frac{|\boldsymbol{m}^{\mathrm{sl}}(\boldsymbol{x}) : \boldsymbol{\sigma}'(\boldsymbol{x})|}{\bar{\tau}^{\mathrm{sl}}(\boldsymbol{x})} \right)^n \times \mathrm{sgn}(\boldsymbol{m}^{\mathrm{sl}}(\boldsymbol{x}) : \boldsymbol{\sigma}'(\boldsymbol{x})) \tag{2.21a}$$

$$\mathrm{sgn}\,(\mathcal{X}) := \begin{cases} -1, & \text{if } \mathcal{X} < 0 \\ 0, & \text{if } \mathcal{X} = 0 \\ 1, & \text{if } \mathcal{X} > 0 \end{cases} \tag{2.21b}$$

Linearization Scheme

The numerical implementation of VPSC offers different choices for the linearization. While Seguardo et al. [28] used an affine linearization, the simulations in this thesis worked with an effective-n approximation (an adaptation of the secant linearization scheme) for explicitly setting a parament n^{eff}. The relevant relations are as follows:

Assuming the same rate-sensitivity n for all slip systems, gives Equation (2.22a) for the viscoplastic compliance $\boldsymbol{M}^{\mathrm{gr}}$ and Equation (2.22b) for the back-extrapolated strain-rate $\boldsymbol{\varepsilon}^{0,\,\mathrm{gr}}$. As mentioned, the viscoplastic strain-rate per grain $\dot{\boldsymbol{\varepsilon}}^{\,\mathrm{gr}}$ is given through a grain average by Equation (2.21a) [17, 34]. Note $\boldsymbol{M}^{\,\mathrm{gr}}$ to be a tensor of rank four.

$$\boldsymbol{M}^{\,\mathrm{gr}} := \dot{\gamma}_0 \sum_{\mathrm{sl}}^{N_{\mathrm{sl}}} \frac{\boldsymbol{m}^{\mathrm{sl,\,gr}} \otimes \boldsymbol{m}^{\mathrm{sl,\,gr}}}{\bar{\tau}^{\mathrm{sl,\,gr}}} \left(\frac{\boldsymbol{m}^{\mathrm{sl,\,gr}} : \boldsymbol{\sigma}'^{\,\mathrm{gr}}}{\bar{\tau}^{\mathrm{sl,\,gr}}} \right)^{n-1} \tag{2.22a}$$

$$\dot{\boldsymbol{\varepsilon}}^{0,\,\mathrm{gr}} = 0 \tag{2.22b}$$

A linear approximation is assumed for the strain-rate $\dot{\boldsymbol{\varepsilon}}$ and stress $\boldsymbol{\sigma}'$ between each statistical-representative grain (gr), through Equation (2.23),

$$\dot{\boldsymbol{\varepsilon}}^{\mathrm{gr}}_{\mathrm{vp}} = \boldsymbol{M}^{\,\mathrm{gr}} : \boldsymbol{\sigma}'^{\,\mathrm{gr}} \tag{2.23}$$

via a linearized viscoplastic compliance tensor $\boldsymbol{M}^{\mathrm{gr}}$ and a back-extrapolated strain-rate $\dot{\boldsymbol{\varepsilon}}^{0,\,\mathrm{gr}}$ of said grain [17, 34]. Note that $\dot{\boldsymbol{\varepsilon}}^{0,\,\mathrm{gr}}_{\mathrm{vp}}$, defined by Equation (2.22b), describes a 'secant' linearization [34], while the constitutive equations in Segurado et al. [28] use an 'affine' linearization for $\dot{\boldsymbol{\varepsilon}}^{0,\,\mathrm{gr}}_{\mathrm{vp}}$.

The aforementioned statistical grain (gr) represents the set of grains with same crystal orientation, inside a statical compatible neighbourhood in the polycrystal [28]. The index (gr) in $\boldsymbol{m}^{\mathrm{sl,\,gr}}$, $\tau^{\mathrm{sl,\,gr}}$ and $\dot{\boldsymbol{\varepsilon}}_{\mathrm{vp}}^{\mathrm{gr}}$ henceforth denote average values of the quantities $\boldsymbol{m}^{\mathrm{sl}}(\boldsymbol{x})$, $\tau^{\mathrm{sl}}(\boldsymbol{x})$ and $\dot{\boldsymbol{\varepsilon}}_{\mathrm{vp}}(\boldsymbol{x})$ from the statistical grain of associated orientation and hardening state [28, 34]. The behaviour of the linear heterogeneous medium can be homogenized similarly at the polycrystal level. Linear Equation (2.24) relates the effective quantities of the polycrystalline strain-rate $\dot{\boldsymbol{\varepsilon}}_{\mathrm{vp}}^{\mathrm{px}}$ and deviatoric stress $\boldsymbol{\sigma}'^{\mathrm{px}}$ by a secant viscoplastic compliance tensor $\boldsymbol{M}^{\mathrm{px}}$ of an a priori unknown HEM that represents the behaviour of polycrystal (px) [28, 34].

$$\dot{\boldsymbol{\varepsilon}}_{\mathrm{vp}}^{\mathrm{px}} = \boldsymbol{M}^{\mathrm{px}} : \boldsymbol{\sigma}'^{\mathrm{px}} \tag{2.24}$$

Interaction Equation Localized Behaviour

Local deviations of the grain averages to the HEM quantities (i.e.: $\widetilde{\boldsymbol{\sigma}}'^{\mathrm{gr}} := \boldsymbol{\sigma}'^{\mathrm{gr}} - \boldsymbol{\sigma}'^{\mathrm{px}}$ and $\widetilde{\dot{\boldsymbol{\varepsilon}}}^{\mathrm{gr}} := \dot{\boldsymbol{\varepsilon}}^{\mathrm{gr}} - \dot{\boldsymbol{\varepsilon}}^{\mathrm{px}}$) can be calculated via an interaction tensor $\widetilde{\boldsymbol{M}}$, by Equation (2.25) [28].

$$\widetilde{\dot{\boldsymbol{\varepsilon}}}^{\mathrm{gr}} = -\widetilde{\boldsymbol{M}} : \widetilde{\boldsymbol{\sigma}}'^{\mathrm{gr}} \tag{2.25}$$

The tensor $\widetilde{\boldsymbol{M}}$, as noted by Equation (2.26), is dependent on the symmetric viscoplastic Eshelby-tensor $\boldsymbol{S}^{\mathrm{gr}}(\boldsymbol{M}^{\mathrm{px}})$ of the grain, which is also a function of the secant viscoplastic compliance tensor $\boldsymbol{M}^{\mathrm{px}}$. Equation (2.26) includes an adjustable effective parameter n^{eff} and the identity matrix $\boldsymbol{I}$. [17, 34].

$$\widetilde{\boldsymbol{M}} := n^{\mathrm{eff}}(\boldsymbol{I} - \boldsymbol{S}^{\mathrm{gr}})^{-1} : \boldsymbol{S}^{\mathrm{gr}} : \boldsymbol{M}^{\mathrm{px}} \tag{2.26}$$

The secant linearization Equation (2.27a), relates the polycrystalline deviatoric stress $\boldsymbol{\sigma}'^{\mathrm{px}}$ to the one a grain is exhibiting $\boldsymbol{\sigma}'^{\mathrm{gr}}$ via a stress localization tensor $\boldsymbol{B}^{\mathrm{gr}}$, which is defined in Equation (2.27b) [34].

$$\boldsymbol{\sigma}'^{\mathrm{gr}} = \boldsymbol{B}^{\mathrm{gr}} : \boldsymbol{\sigma}'^{\mathrm{px}} \tag{2.27a}$$

$$\boldsymbol{B}^{\mathrm{gr}} := (\boldsymbol{M}^{\mathrm{gr}} + \widetilde{\boldsymbol{M}})^{-1} : (\boldsymbol{M}^{\mathrm{px}} + \widetilde{\boldsymbol{M}}) \tag{2.27b}$$

Equation (2.28) gives the relation between the average magnitudes of deviatory stress $\boldsymbol{\sigma}'^{\mathrm{px}}$ and the strain-rate $\dot{\boldsymbol{\varepsilon}}_{\mathrm{vp}}^{\mathrm{gr}}$ of the grain. It can be derived by using the stress localization Equation (2.27a) in Equation (2.23) [28]. Again, note the linearization scheme from Equation (2.22).

$$\dot{\boldsymbol{\varepsilon}}_{\mathrm{vp}}^{\mathrm{gr}} = \boldsymbol{M}^{\mathrm{gr}} : \boldsymbol{B}^{\mathrm{gr}} : \boldsymbol{\sigma}'^{\mathrm{px}} \tag{2.28}$$

Volumetric averages, noted by $\langle\cdot\rangle$, can now be taken, while the condition that the average of the strain-rates of the statistical-representative grains over the polycrystal has to coincide with the macroscopic quantities, i.e.: Equation (2.29), is enforced [28].

$$\dot{\boldsymbol{\varepsilon}}_{\mathrm{vp}}^{\mathrm{px}} := \left\langle \dot{\boldsymbol{\varepsilon}}_{\mathrm{vp}}^{\mathrm{gr}} \right\rangle \tag{2.29}$$

Self-Consistent Equations and Iterative Approach

The self-consistent equations for the polycrystal relation tensor $\boldsymbol{M}^{\mathrm{px}}$ are obtained via Equation (2.30), by averages over all statistical representative grains [28].

$$\boldsymbol{M}^{\mathrm{px}} := \langle \boldsymbol{M}^{\mathrm{gr}} : \boldsymbol{B}^{\mathrm{gr}} \rangle \tag{2.30}$$

All relevant relations are calculated for each grain at each polycrystalline material point of the solid body deformation problem. While the standard VPSC-model can be started with either an imposed strain-rate, an imposed stress or even mixed boundary conditions, the adapted version for use in FEM is designed for stress-imposed boundary conditions only, resulting from a strain increment on the element. In this framework, a VPSC calculation starts with the uniform initial stress guess $\boldsymbol{\sigma'}^{\mathrm{gr}} = \boldsymbol{\sigma'}^{\mathrm{px}}$ for the grains by taking the finite element trial stress for $\boldsymbol{\sigma'}^{\mathrm{px}}$. Starting the initial guess of $\boldsymbol{\sigma'}^{\mathrm{gr}}$, the corresponding initial guesses for $\dot{\boldsymbol{\varepsilon}}_{\mathrm{vp}}^{\mathrm{gr}}$ and $\boldsymbol{M}^{\mathrm{gr}}$ can be obtained via Equation (2.21a) and Equation (2.22a). Following, initial guesses for the polycrystal interaction tensor $\boldsymbol{M}^{\mathrm{px}}$ are obtained as averages over the local ones. Together with the applied stress, the initial guess for the polycrystal strain rate $\dot{\boldsymbol{\varepsilon}}_{\mathrm{vp}}^{\mathrm{px}}$, Equation (2.24), as well as the symmetric Eshelby tensor $\boldsymbol{S}$ is obtained [17, 28]. The ellipsoidal shape of the statistical grains and the viscoplastic tangent stiffness is updated, with details here provided by Lebensohn et al. in [17]. Subsequently, the interaction tensor $\widetilde{\boldsymbol{M}}$ and the localization tensor $\boldsymbol{B}^{\mathrm{gr}}$ are updated by Equation (2.26) and Equation (2.27b) respectively. These tensors are used to obtain a new estimate of $\boldsymbol{M}^{\mathrm{px}}$ by solving iteratively the self-consistent Equation (2.30). If convergence is achieved on $\boldsymbol{M}^{\mathrm{px}}$, a new estimate for average grain stresses $\boldsymbol{\sigma'}^{\mathrm{gr}}$ can be obtained by the localization Equation (2.27a). If the recalculated grain stresses are different from the input values (within a certain tolerance), a new calculation is started until convergence is reached [17, 28]. After the iterative procedure, the average shear rates $\dot{\gamma}^{\mathrm{sl,\,gr}}$ of the slip system (sl) in each grain (gr) are calculated by Equation (2.31),

$$\dot{\gamma}^{\mathrm{sl,\,gr}} = \dot{\gamma}_0 \left(\frac{|\boldsymbol{m}^{\mathrm{sl,\,gr}} : \boldsymbol{\sigma'}^{\mathrm{gr}}|}{\bar{\tau}^{\mathrm{sl,\,gr}}} \right) \times \mathrm{sgn}\left(\boldsymbol{m}^{\mathrm{sl,\,gr}} : \boldsymbol{\sigma'}^{\mathrm{gr}}\right) \tag{2.31}$$

where $\dot{\gamma}_0$ is a normalizing factor, $\boldsymbol{m}^{\mathrm{sl,\,gr}}$ the Schmid tensor, $\boldsymbol{\sigma'}^{\mathrm{gr}}$ the deviatoric stress and $\bar{\tau}^{\mathrm{sl,\,gr}}$ the current CRSS for slip system activation. Note that the increase of the CRSS is calculated by the iterative formulation in Equation (2.19). It makes use of the time step Δt dependence noted in Equation (2.32) for the change of the shear strain $\Delta\gamma^{\mathrm{sl'}}$ in slip system sl' [28]. Refer to Section 2.2.3 for details.

$$|\Delta\gamma^{\mathrm{sl'}}| := \dot{\gamma}^{\mathrm{sl'}} \Delta t \tag{2.32}$$

Together with FEM this model simultaneously accounts for the strength of the actual deformation mechanisms active at single-crystal level, the polycrystalline character of the aggregate microstructure and its evolution with deformation under specific boundary conditions applied to the sample, as Seguardo et al. mentioned in [28]. Details on the implementation of VPSC inside the FEM-solver are provided in Section 3.3, after the explanation of FEM in Section 3.2.

2.3.2 Solid Body Deformation

For solving a boundary value problem of a solid body deformation via FEM as described in section 3.2, the kinematics of the sample body in space has to be considered. The most general problem is the result of rigid body motion and an independent deformation [25]. For the following explanation, the problem is simplified and assumed to be only deformation at constant strain rate.

To describe this mathematically, consider a homogeneous, isotropic, elastic body whose material points in the current positions $\boldsymbol{x}$, occupy a domain $\Omega \subset \mathbb{R}^3$, inside a boundary $\mathcal{R}$ that is separated into two parts. The first one $\mathcal{R}_1$ is fixed in space, meaning points on $\mathcal{R}_1$ are not displaced, while the second one $\mathcal{R}_2$ is exhibiting a surface load $\boldsymbol{f}^S(\boldsymbol{x}) = (f_1^S, f_2^S, f_3^S)^\top$. Furthermore, the body shall be acted upon by a volume load $\boldsymbol{f}^B(\boldsymbol{x}) = (f_1^B, f_2^B, f_3^B)^\top$. For solving the deformation problem, the displacement $\boldsymbol{u}(\boldsymbol{x}) = (u_1, u_2, u_3)^\top$ of the points in their current configuration from their reference configuration under the loads $\boldsymbol{f}^B$ and $\boldsymbol{f}^S$ is searched. By assuming the body to be linearly elastic and that the deformations are small, the following Partial Differential Equation (PDE) (2.33) holds for the stress-tensor field $\boldsymbol{\sigma}(\boldsymbol{x})$ of Equation (1.6) and the small strain-tensor field $\boldsymbol{\varepsilon}(\boldsymbol{u})$ of Equation (1.12),

$$\sigma_{ij} = \lambda \frac{\partial u_k}{\partial x_k} \delta_{ij} + \mu \varepsilon_{ij}(\boldsymbol{u}) \tag{2.33}$$

where μ and λ are positive constants and δ_{ij} is the Kronecker delta [11]. Now to consider the equilibrium of the forces inside Ω as well as the boundary conditions on $\mathcal{R}$.

Equilibrium Forces and Boundary Conditions

In a rectangular Cartesian coordinate system, the equilibrium equations under a volume load $\boldsymbol{f}^B$ inside the domain Ω is given by the equilibrium Equation (2.34), over the local spatial derivative $\partial/\partial x_j$ of the tensorial stress field σ_{ij}, as defined by Equation (1.6) [11]. Note again sum convention and index notation, i.e. sum over i, j from 1 to 3.

$$-\frac{\partial \sigma_{ij}}{\partial x_j} =: f_i^B, \text{ in } \Omega \tag{2.34}$$

The boundary conditions of the elasticity problem, as defined in the beginning of Section 2.3.2, are given by Equation (2.35a) and (2.35b) for their respective boundaries $\mathcal{R}_{1,2}$,

$$u_i = 0, \text{ on } \mathcal{R}_1 \tag{2.35a}$$

$$\sigma_{ij} n_j =: f_i^S, \text{ on } \mathcal{R}_2 \tag{2.35b}$$

where n_j are the components of the outward surface normal [11].

Applying Green's Theorem

The Partial Differential Equation (PDE) (2.33) together with its boundary conditions of Equation (2.35) and the equilibrium condition from Equation (2.34), can be rewritten as the integral Equation (2.41) by the following steps.

Considering $\boldsymbol{v}$ to be an arbitrary deformation $\boldsymbol{u}$ that satisfies Equation (2.35a), then Equation (2.36) holds, due to the symmetry of $\boldsymbol{\sigma}$ and the definition of $\boldsymbol{\varepsilon}$ for small strains [11]. Note that indices can be rearranged due to the summation.

$$\sigma_{ij}\varepsilon_{ij}(\boldsymbol{v}) = \frac{1}{2}\left(\sigma_{ij}\frac{\partial v_i}{\partial x_j} + \sigma_{ij}\frac{\partial v_j}{\partial x_i}\right) = \sigma_{ij}\frac{\partial v_j}{\partial x_i} \tag{2.36}$$

Using Equation (2.36) together with Green's theorem gives Equation (2.37) for the boundary value problem, where n_i are the components of the surface normal to the boundary $\mathcal{R}$ [11]. In the following integral equations, $\mathrm{d}S$ and $\mathrm{d}V$ shall denote infinitesimal surface and volume elements, on the boundary $\mathcal{R}$ or in the volume Ω, respectively.

$$\int_\Omega \sigma_{ij}\varepsilon_{ij}(\boldsymbol{v})\,\mathrm{d}V = \underbrace{\int_\Omega \sigma_{ij}\frac{\partial v_j}{\partial x_i}\,\mathrm{d}V = \int_\mathcal{R} \sigma_{ij}n_i v_j\,\mathrm{d}S - \int_\Omega \frac{\partial \sigma_{ij}}{\partial x_i}v_j\,\mathrm{d}V}_{\text{Green's theorem}} \tag{2.37}$$

Rearranging Equation (2.37) results in Equation (2.38), by considering the equilibrium condition of Equation (2.34) for the body forces $\boldsymbol{f}^B$ inside the domain Ω [11].

$$\int_\Omega \sigma_{ij}\varepsilon_{ij}(\boldsymbol{v})\,\mathrm{d}V = \int_\Omega \underbrace{-\frac{\partial \sigma_{ij}}{\partial x_i}}_{f_i^B} v_j\,\mathrm{d}V + \int_\mathcal{R} \sigma_{ij}n_i v_j\,\mathrm{d}S \tag{2.38}$$

The boundary integral over $\mathcal{R}$ can be considered to only have a contribution from $\mathcal{R}_2$ by enforcing $v_j = 0$ along $\mathcal{R}_1$, as this directly enforces the Dirichlet boundary of Equation (2.35a). This means the boundary integral can be expressed by the surface loads $\boldsymbol{f}^S$ on $\mathcal{R}_2$ of Equation (2.35b), resulting in Equation (2.39) [11].

$$\int_\Omega \sigma_{ij}\varepsilon_{ij}(\boldsymbol{v})\,\mathrm{d}V = \int_\Omega f_i^B v_i \mathrm{d}V + \int_{\mathcal{R}_2} f_i^S v_i\,\mathrm{d}S \tag{2.39}$$

Considering that the divergence of the deformation $\boldsymbol{v}$ to be the trace of the strain tensor $\boldsymbol{\varepsilon}(\boldsymbol{v})$ gives Equation (2.40).

$$\frac{\partial u_k}{\partial x_k}\,\delta_{ij}\varepsilon_{ij}(\boldsymbol{v}) = \frac{\partial u_l}{\partial x_l}\frac{\partial v_m}{\partial x_m} \tag{2.40}$$

Equation (2.40) can be used together with Equation (2.33) (multiplied by $\varepsilon_{ij}(\boldsymbol{v})$), to obtain Equation (2.41) from Equation (2.39),

$$\underbrace{\int_\Omega \left[\lambda\frac{\partial u_k}{\partial x_k}\frac{\partial v_m}{\partial x_m} + \mu\varepsilon_{ij}(\boldsymbol{u})\varepsilon_{ij}(\boldsymbol{v})\right]\mathrm{d}V}_{a(\boldsymbol{u},\boldsymbol{v})} = \underbrace{\int_\Omega f_i^B v_i \mathrm{d}V + \int_{\mathcal{R}_2} f_i^S v_i\,\mathrm{d}S}_{L(\boldsymbol{v})} \tag{2.41}$$

where λ and μ are constants, defined through the modulus of elasticity and the contraction ratio of the elastic material [11].

Equation (2.41) is the starting point to obtain the terms a and L for the variational form of the energy functional in Equation (3.11), for the Finite Element Method (FEM) described in Section 3.2 [11]. For considering polycrystalline aggregates at the material points using the VPSC-approach, see Section 3.3.1.

Note, generally plastic incompressibility is assumed, when simulating solid body deformations. By considering all volume changes of Ω to be reversible, the determinant of the deformation gradient $\boldsymbol{\mathcal{F}}$ is constant for a plastic deformation step [25, 20]. Therefore, together with mass conservation, the plastic incompressibility assumption leads to a constant global material mass density [20].

Considering Anisotropic Material using coupled VPSC

Equation (2.41) is the integral reformulation of the Partial Differential Equation (2.33) that describes a static configuration change at no specified length scale for the material points of a solid body in space (refer to Section 1.2.1) under the set boundary conditions. A detailed outlay on computationally using Equation (2.41) to obtain a solution for Partial Differential Equation (2.33) using FEM is provided Section 3.2. However, in Section 2.3.2 no information was defined about any inner structure of said body. As this thesis uses a multiscale approach for calculating the microstructure evolution and the resulting material response to the deformation, such information still has to be coupled to the configuration change. The mathematics for using VPSC for the material responses is sketched in Section 3.3 with a technical overview of the interaction between the FEM-solver and the VPSC microstructure model seen in Section 3.3.3.

2.3.3 Stress-Strain Curve Evaluation

From the stress and strain definitions in Section 1.2.2 it becomes already apparent that those two are deeply connected with each other for a said material. In case of small strains, the deformation is elastic and reverses if the load is removed. At high enough stresses, a non-recoverable plastic deformation occurs [10], which is also explicitly seen by looking at a typical one dimensional stress-strain curve for a ductile material, as Figure 2.10 provides for aluminium. There, the Ultimate Tensile Strength (UTS) is defined at the highest value of the engineering stress, and for ductile materials describes the point where the necking starts. Typically, the onset of plastic deformation is associated with the first deviation of the stress-strain curve from linearity. However, as more accurate strain measurements lead to an earlier detection of non-linearity, the elastic limit is usually given via an offset yield strength σ_{Y}. Here, the idea is that if the material had been loaded to this stress and afterwards been unloaded, the stress-strain path of unloading would follow along a straight offset line, which results in a plastic strain of $\varepsilon = 0.2\,\%$ [10]. The UTS has been marked in Figure 2.10 together with the point of material fracture as well as the regions of material necking and strain-hardening, mentioned in Section 2.2.3.

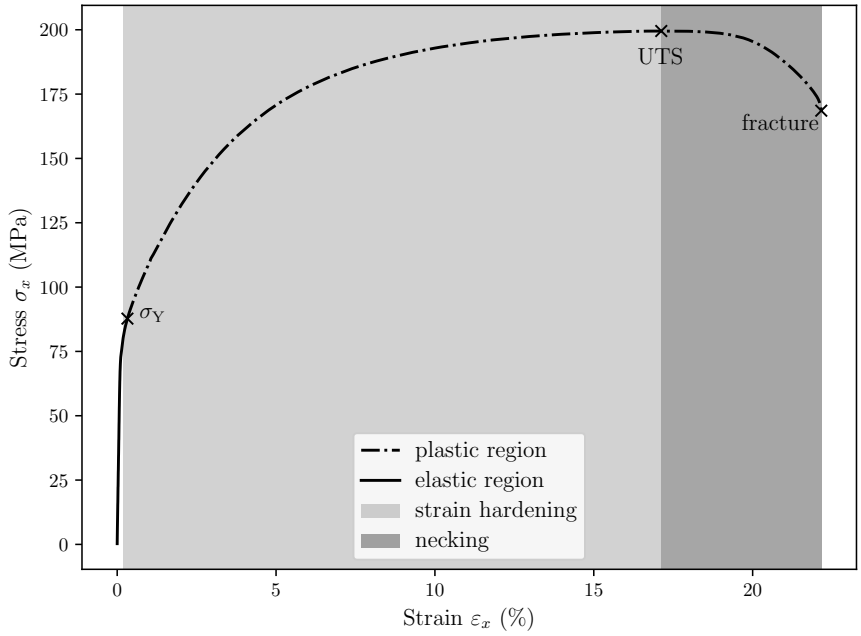

Figure 2.10: Typical stress-strain curve of an aluminium sample, measured at LKR.

The area under the curve of Figure 2.10 gives information on the elastically and plastically absorbed energy. Experimentally, the usual way to acquire a stress-strain curve like shown in Figure 2.10 is by measuring tension of a rod (tension test) or compression of a short cylindrical block (compression test) and tracking the deformation at an applied load [9]. Details, on how these experiments are commonly performed can be read in literature (e.g. [10, 6]) but are omitted in this thesis. Further note, that this thesis focuses on the plastic region of material deformations.

While the elastic region exhibits a linear relationship between stress and strain, as Hook's law describes, it can be observed in Figure 2.10 that at Room Temperature (RT) the metal's resistance to further deformation increases. This process is dependent on the previous history of plastic strain, leading, under some assumptions, to the degree of hardening being a function of the plastic work. For the mathematical description of this strain- or work-hardening, on a macroscopic scale, isotropic material might be assumed. The total plastic work per unit volume during a finite deformation is then calculated as an integral of the stress taken along the strain path [9, 15]. For the derivation of such isotropic hardening, found in [9], it is further considered that the elastic part of the total external work is recoverable elastic energy. Note that the assumption of isotropic hardening is not always true for a real metal, since the plastic yielding depends on the distribution of microscopic internal stresses, and these themselves on the strain history.

The scalar, effective plastic strain quantity $\varepsilon_{\mathrm{p}}^{\mathrm{eff}}$ is defined by Equation (2.42a) through the integral over the time t, where the plastic strain rate tensor $\dot{\boldsymbol{\varepsilon}}_{\mathrm{p}}$ is given by the difference between the total strain rate tensor $\dot{\boldsymbol{\varepsilon}}$ to the elastic one $\dot{\boldsymbol{\varepsilon}}_{\mathrm{el}}$. In terms of the non-principal

strains, $\varepsilon_{\mathrm{p}}^{\mathrm{eff}}$ can be expressed by Equation (2.42b) [10, 20].

$$\varepsilon_{\mathrm{p}}^{\mathrm{eff}} = \int_{t_0}^{t_1} \sqrt{\frac{2}{3}\dot{\boldsymbol{\varepsilon}}_{\mathrm{p}} : \dot{\boldsymbol{\varepsilon}}_{\mathrm{p}}}\, \mathrm{d}\, t \tag{2.42a}$$

$$\dot{\boldsymbol{\varepsilon}}_{\mathrm{p}} = \dot{\boldsymbol{\varepsilon}} - \dot{\boldsymbol{\varepsilon}}_{\mathrm{el}} \tag{2.42b}$$

The Von Mises or effective stress σ^{eff} is a function of the applied stresses that determine if yielding (i.e. plastic deformation) occurs [10, 20]. In terms of Equation (2.43), where $\sigma_{x,y,z}$ are the diagonals of the stress tensor $\boldsymbol{\sigma}$, whose the off-diagonals are denoted using τ_{xy}, τ_{yz} and τ_{zx}. Refer to Section 1.2.

$$\sigma^{\mathrm{eff}} = \frac{1}{\sqrt{2}}\sqrt{(\sigma_x - \sigma_y)^2 + (\sigma_y - \sigma_z)^2 + (\sigma_z - \sigma_x)^2 + 6(\tau_{xy}^2 + \tau_{yz}^2 + \tau_{zx}^2)} \tag{2.43}$$

A deeper look into the topic of strain-hardening is provided under Section 2.2.3, where dislocation density terms are taken to derive the extended Voce hardening law used to describe polycrystalline hardening in this thesis.

3 Computational Methods, Equipment and Material Data

The deformation calculations of the sample geometries are done by the proprietary FEM-software LS-DYNA®, which is a program originally developed for stress analysis of structures subjected to a variety of impact loading [19] and is in use at LKR for metal forming calculations. The theory relevant for this macroscopic deformation of the sample is provided in Section 2.3.2, with the details regarding the plastic deformation computation, laid out in Section 3.2. LS-DYNA® enables the use of custom User Defined Material Model (UMAT) for calculating material responses. This makes it possible to use a material model that takes the stress responses of polycrystal aggregates and their microstructure evolution into account. To calculate the polycrystalline behaviour in this thesis, an adaptation of the VPSC [18] standalone program, VPSC-FEM, developed by Seguardo et al. in [28] is used. The underlying theory of this approach was briefly outlined in Section 2.3.1.

Note that calculating the microstructural polycrystalline response and the total sample deformation by different programs, separates the needed in-/output into two different sets of data. Microstructural information, like the Voce hardening parameters, their slip modes and the initial polycrystalline texture, are provided directly to VPSC-FEM, while the sample geometry (or mesh) as well as the applied deformation path is given in LS-DYNA® input files. Figure 3.1 schematically displays the steps that have been taken for each of the simulations shown in Section 4. The first step, Data Acquisition, was done by colleagues at the LKR and included the macroscopic material tests as well as microstructural Electron Back Scatter Diffraction (EBSD) measurements and preliminary texture optimizations through a clustering technique. These preparations were needed to obtain the Voce parameters that correspond to certain temperatures for the slip mode by running an optimization algorithm to fit the FEM coupled VPSC simulations to the measurement data. Details on these topics are listed in Section 3.4.2

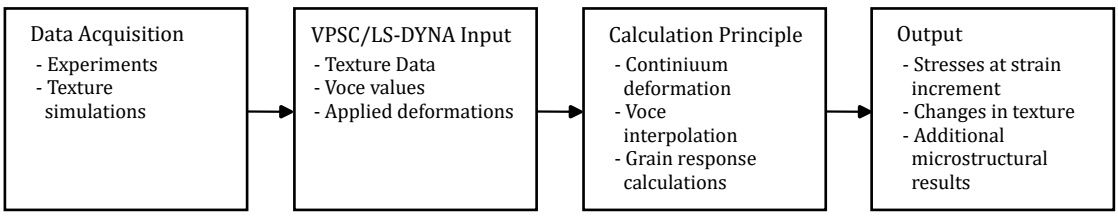

Figure 3.1: Workflow for the multiscale simulations.

Technical information regarding the linking of VPSC-FEM as an UMAT for LS-DYNA®

can be read in Section 3.1, with additional numerical information regarding VPSC-FEM in Section 3.3.

3.1 Technical Details

The FEMsolver LS-DYNA® is a proprietary software, that is only available as a precompiled solver. For providing a custom material routine, the UMAT is needed to be a precompiled binary by being either a shared object (.so) or a dynamic link library (.dll) [19]. VPSC-FEM is being provided as a shared object through a precompiled module, which was created from LKR's version of VPSC-FEM by using the Fortran compiler ifort, with instructions given by a Makefile. At execution, LS-DYNA® takes the shared object file from a provided directory and links it to the current execution. This method provides a flexible approach by having a binary executable only installed once [19]. Figure 3.2 provides a schematic of the dependencies.

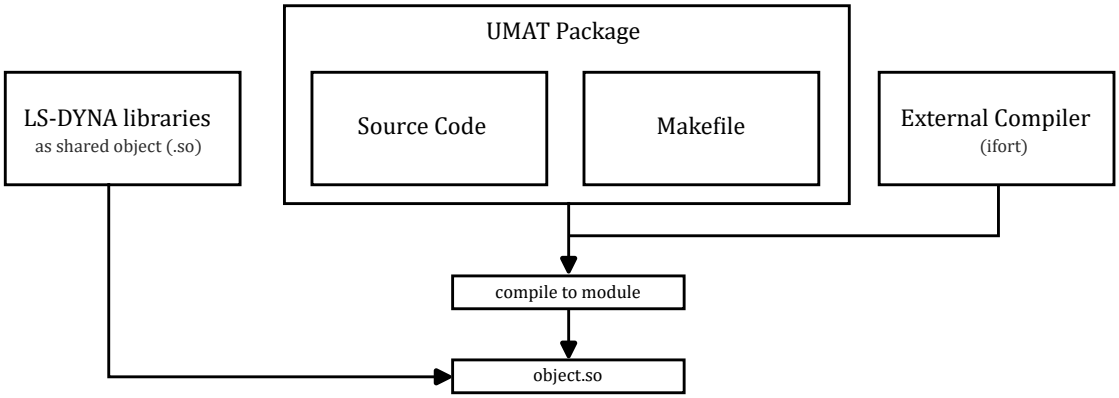

Figure 3.2: Technical connection between UMAT and LS-DYNA®, as laid out in more detail within the LSTC user-manual [19].

Simulations were done on LKR's HPE Blade Cluster for numerical simulations, which is a 64 bit Linux system running on 16 ProLiant BL460c Gen9 Blades, each consisting of 16 Intel® Xenon® CPU E-2667 v4 at 3.20 GHz and 132 GB RAM. Parallelization of the LS-DYNA® solver is accomplished using the platform-MPI standard. LS-DYNA® as well as VPSC-FEM are written in the programming language Fortran. Evaluating and presenting the results was achieved via the programming language Python3. The graphical representations of the mesh geometries are displayed using the program LS-PrePost® version 4.9. The optimization were controlled using the analysis tool LS-OPT®, version 7.0.2.

3.2 Finite Element Method (FEM)

The Finite Element Method (FEM) is a general technique for numerically solving differential and integral equations in science and engineering. Like in any numerical method for solving a PDE, the basic idea is to discretize the given continuous problem that has infinitely many degrees of freedom to obtain a discrete problem or system of equations with only finitely many unknowns [11]. One numerical method for solving PDEs is the Finite Difference Method (FDM), where the discrete problem is obtained by replacing derivatives with difference quotients involving the values of the unknown variable at specified finitely many points. In contrast to FDM, the FEM discretization process is fundamentally different. In FEM, the starting point is a reformulation of the given differential equation as an equivalent variational problem. More specifically, the solution u of the boundary value PDE is also the solution of a minimization problem and the subsequent variational problem [11]. For basic cases of elliptic PDEs a minimization problem in the form Equation (3.1) needs to be solved for u,

$$\text{Find } u \in \mathbb{V} \text{ such that } F(u) \leq F(v) \, \forall \, v \in \mathbb{V} \tag{3.1}$$

where $\mathbb{V}$ is a given set of admissible functions, $F : \mathbb{V} \to \mathbb{R}$ is a functional and $\mathbb{R}$ the set of real numbers. Often the arbitrary test functions $v \in \mathbb{V}$ represent a continuously varying quantity, like a temperature or displacement, in a deformation problem. $F(v)$ is the total energy associated with v and a solution to the PDE in question is obtained as a function in $\mathbb{V}$ that minimizes the total energy of the considered system. The variational formulation is said to be a weak formulation of the boundary value PDE, and its solution u to be the weak solution of the PDE, as it is not eminently clear that u is also a classical solution to the PDE [11].

Due to the dimension of $\mathbb{V}$ being infinite, the general problem can still not be solved exactly. To obtain a problem solvable by computational methods, the idea of FEM is to replace $\mathbb{V}$ of Equation (3.1) by a finite-dimensional subset $\mathbb{V}_h$, consisting of simple functions that only depend on a limited number of parameters, which is equivalent to a large (non)linear systems of equations [11]. Usually $\mathbb{V}_h \subset \mathbb{V}$ is chosen, meaning $v \in \mathbb{V}_h$ automatically implies $v \in \mathbb{V}$, which corresponds to the classical Ritz-Galerkin method, where the functions in $\mathbb{V}_h$ are piecewise polynomial. A more general start than from a minimization problem for the variational problem is provided by the so-called Galerkin methods. The choice of the finite element subspace $\mathbb{V}_h$ is essentially the choice of the finite element discretization [11].

3.2.1 Continuous Problems of Elliptic Type

By considering an abstract formulation of the FEM for elliptic problems, it is possible to give a unified treatment to many problems in mechanics and physics, including the solid body deformation problem that was discussed in Section 2.3.2 [11].

Let $\mathbb{V}$ be a Hilbert space with a scalar product $(.,.)_{\mathbb{V}}$ with a corresponding norm $||\cdot||_{\mathbb{V}}$. Suppose $a(.,.)$ to be a bi-linear form on $\mathbb{V} \times \mathbb{V}$ that is symmetric and continuous. Furthermore, a shall be $\mathbb{V}$-elliptic. Together with a linear form L on $\mathbb{V}$ that is also

continuous, Equation (3.2a) then notes the abstract form of the minimization problem written in Equation (3.1). More precisely, Equation (3.2a) searches for an element $u \in \mathbb{V}$ that satisfies the minimization criteria of a functional F given through Equation (3.2b) [11].

$$F(u) = \min_{v \in \mathbb{V}} F(v) \tag{3.2a}$$

$$F(v) := \frac{1}{2} a(v, v) - L(v) \tag{3.2b}$$

Equation (3.3) searches for a $u \in \mathbb{V}$ via an abstract formulation of the variational problem. The proof of the equivalence between minimization Equation (3.2a) and the variational Equation (3.3) can be found in literature, e.g. the book by C. Johnson [11]. It states that a unique solution $u \in \mathbb{V}$ only fulfils Equation (3.2a), if u satisfies Equation (3.3) as well.

$$a(u, v) = L(v) \, \forall \, v \in \mathbb{V} \tag{3.3}$$

3.2.2 Ritz-Galerkin Discretization

For computational purposes, a continuous domain Ω within its boundary $\mathcal{R}$ has to be discretized. By defining a number of M nodal-points (nodes) n_i, Ω can be meshed into N non-overlapping finite elements by connecting the nodes accordingly, e.g. resulting in three-dimensional brick or triangulation elements representing the domain. A finite element k is uniquely defined by the nodes located on (or within) its boundary, where each node has an associated, so-called shape function [15, 11].

As was mentioned in the beginning of Section 3.2, the discretization by the Ritz-Galerkin method, takes a finite (M-dimensional) subspace $\mathbb{V}_h$ of $\mathbb{V}$. Considering $\{\varphi_1, \ldots, \varphi_M\}$ to be a basis for $\mathbb{V}_h$ gives any $v \in \mathbb{V}_h$ the unique representation of Equation (3.4),

$$v = \sum_{j=1}^{M} \eta_j \varphi_j \tag{3.4}$$

where $\eta_j \in \mathbb{R}$. Typically, piecewise polynomial and globally continuous functions are chosen for $\mathbb{V}_h$. An example being to define $\mathbb{V}_h$ as a space consisting of all continuous functions that are affine on every element and vanish on $\mathcal{R}$ by Equation (3.5).

$$\varphi_j(n_i) = \delta_{ij} \tag{3.5}$$

where δ_{ij} denotes the Kronecker delta and $i, j \in [1, M]$. The parameters, to describe $v \in \mathbb{V}_h$, can then directly be chosen as the values $v(n_i)$ of v at the current node n_i, i.e. setting $\eta_j = v(n_j)$ in Equation(3.4) [11].

Using a Ritz-Galerkin discretization, the form of the minimization problem Equation (3.1), is directly given via Equation (3.6), for the boundary value PDE in question [11].

$$\text{Find } u_h \in \mathbb{V}_h \text{ such that } F(u_h) \leq F(v) \, \forall \, v \in \mathbb{V}_h \tag{3.6}$$

Following the arguments of Section 3.2.1, the discrete form of the equivalent abstract variational problem Equation (3.3) can be written as Equation (3.7),

$$a(u_h, v) = L(v) \; \forall \, v \in \mathbb{V}_h \tag{3.7}$$

which is solved for a $u_h \in \mathbb{V}_h$ for obtaining a solution of the discrete minimization problem in Equation (3.6) [11]. Continuing, as v in Equation (3.7) needs to hold for any arbitrary test function it is replaced with any basis function φ_j of its unique representation Equation (3.4), creating the equivalent Equation (3.8) [11].

$$a(u_h, \varphi_j) = L(\varphi_j), \;\; j \in [1, M] \tag{3.8}$$

Using the linear representation of u_h by the basis $\{\varphi_i\}_{i=1}^{M}$ of $\mathbb{V}_h$ and $\xi_i \in \mathbb{R}$, displayed in Equation (3.9), gives the variational problem through Equation (3.10a) [11].

$$u_h = \sum_{i=1}^{M} \xi_i \varphi_i \tag{3.9}$$

Equation (3.10a) can be rewritten as matrix Equation (3.10b), by using the components l_j and C_{ij} of the vector $\boldsymbol{l}$ and the positive definite[1] matrix $\boldsymbol{C}$ respectively [11]. $\boldsymbol{C}$ is a $M \times M$ matrix, of elements $C_{ij} = a(\varphi_i, \varphi_j)$, while ξ and l are M-vectors with elements $\xi_i = u_h(n_i)$ and $l_i = (f, \varphi_i)$.

$$\sum_{i=1}^{M} \underbrace{a(\varphi_i, \varphi_j)}_{C_{ij}} \xi_i = \underbrace{L(\varphi_j)}_{l_j} \tag{3.10a}$$

$$\boldsymbol{C}\boldsymbol{\xi} = \boldsymbol{l} \tag{3.10b}$$

If Equation (3.10b) is applied to an elasticity problem, $\boldsymbol{C}$ and $\boldsymbol{l}$ are referred being the symmetric stiffness matrix and the load vector respectively. In practice, the elements in the stiffness matrix are computed by summing up the contributions $\boldsymbol{C}_k$ of all N different elements k, where $\boldsymbol{C}_k$ is the so-called element stiffness matrix for k, consisting of the components $a_k(\varphi_i, \varphi_j)$. Correspondingly, the same is done for the global load vector $\boldsymbol{l}$, where $\boldsymbol{l}_k$ is the load vector of element k. This process is called assembling of $\boldsymbol{C}$ and $\boldsymbol{l}$ [11]. The solution $\{\xi_i\}_{i=1}^{M}$ of the linear system of equations from Equation (3.10b) now needs to be calculated computationally, using different variants of the Gaussian elimination or iterative method.

3.2.3 Application to Elasticity

For the elastic problem of a solid body deformation, the functional F in Equation (3.2b) represents the total potential energy, given via the terms $\frac{1}{2}a(v, v)$ and $L(v)$ of the internal elastic energy and the load potential respectively. This means that in mechanics, FEM's

[1] i.e. all eigenvalues are greater 0 [12]

conditional Equation (3.1) corresponds to the principle of minimum potential energy, while the variational reformulation corresponds to the principle of virtual work [11].

It can be seen from the balance Equation (2.39), that the full energy functional F^{def} for the continuum deformation described in Section 2.3.2 is then given by Equation (3.11). Following, bold letters are again used to indicate that $\boldsymbol{v} = (v_1, v_2, v_3)\top$ and $\boldsymbol{u} = (u_1, u_2, u_3)^\top$ note displacement vector fields[2]. Note index notation and sum convention.

$$F^{\text{def}} = \frac{1}{2} \underbrace{\int_\Omega \sigma_{ij}(\boldsymbol{v}) \varepsilon_{ij}(\boldsymbol{v}) \, \mathrm{d}V}_{a(\boldsymbol{v},\boldsymbol{v})} \underbrace{- \int_\Omega f_i^B v_i \mathrm{d}V - \int_{\mathcal{R}_2} f_i^S v_i \, \mathrm{d}S}_{L(\boldsymbol{v})} \tag{3.11}$$

However, Equation (2.39) is actually an intermediate step to obtain the variational formulation of the equilibrium Equation (2.34) from the deformation Partial Differential Equation (2.33) problem, with its boundary conditions listed in Equation (2.35). Section 2.3.2 directly closed with the variational Equation (2.41) that is used to obtain the deformation through computational means by solving Equation (3.7) through the presented, discrete approach from Section 3.2.2. The solution at the Dirichlet boundary for the PDE is directly given by the set value on the boundary.

3.3 VPSC as UMAT

Originally, VPSC-FEM is an adaptation of VPSC for use as an UMAT model for the FEM software ABAQUS® that was developed by Seguardo et al. [28] and later extended by Zecevic et al. [39, 40] into a multipurpose general material model that is also able to calculate high-strain rate impacts. In LKR, an adapted version of the extended ABAQUS® VPSC-FEM version by Zecevic et al. is used, where a tailored interface converts the values of the microstructural calculations into an LS-DYNA® UMAT compatible format.

3.3.1 Localized Kinematics and Rotations

The VPSC material model of Section 2.3.1, is devised to work under the small-strain approximation of finite deformations. Following, a linear decomposition of the polycrystal's total strain increment $\Delta\boldsymbol{\varepsilon}$ can be performed by defining an elastic $\Delta\boldsymbol{\varepsilon}_{\text{el}}$ and viscoplastic $\Delta\boldsymbol{\varepsilon}_{\text{vp}}$ part, giving Equation (3.12) [28].

$$\Delta\boldsymbol{\varepsilon} := \Delta\boldsymbol{\varepsilon}_{\text{el}} + \Delta\boldsymbol{\varepsilon}_{\text{vp}} \tag{3.12}$$

The relations for the elastic and plastic share of the incremental strains $\Delta\boldsymbol{\varepsilon}$ to an incremental overall Cauchy stress $\Delta\boldsymbol{\sigma}$ is given by Equation (3.13a) and Equation (3.13b), where $\boldsymbol{C}$ denotes the stiffness-tensor at the polycrystalline material point [28]. Both strain increments $\Delta\boldsymbol{\varepsilon}_{\text{el}}$ and $\Delta\boldsymbol{\varepsilon}_{\text{vp}}$ are calculated within the VPSC approach, as it also considers the criterium of yielding for the elastic limit, meaning the model gives a total

[2] i.e. $\boldsymbol{v}, \boldsymbol{u} \in [\mathbb{V}(\Omega)]^3$, with $\mathbb{V}$ denoting a Hilbert space for the bounded domain Ω of the body [11]

strain increment of a polycrystal, by being only provided the total stress increment $\Delta\boldsymbol{\sigma}$ the solid body deformation sample is locally exhibiting [28].

$$\Delta\boldsymbol{\varepsilon}_{\mathrm{el}} := \boldsymbol{C}^{-1} : \Delta\boldsymbol{\sigma} \tag{3.13a}$$

$$\Delta\boldsymbol{\varepsilon}_{\mathrm{vp}} := \Delta\boldsymbol{\varepsilon}_{\mathrm{vp}}(\Delta\boldsymbol{\sigma}) \tag{3.13b}$$

Defining a rotating local coordinate system given by the unit vectors $\boldsymbol{e}_\alpha$, with $\alpha \in \{1, 3\}$, allows for calculating the polycrystalline behaviour, as described in [28]. The rotational evolution of the unit vectors $\boldsymbol{e}_\alpha$ is given by Equation (3.14) and needs to be accounted for by the FEM-model,

$$\dot{\boldsymbol{e}}_\alpha = \dot{\boldsymbol{\omega}} \cdot \boldsymbol{e}_\alpha \tag{3.14}$$

where $\dot{\boldsymbol{\omega}}$ is the total rotation-rate of the polycrystalline material point [28]. Integrating the rotation-rate in a time increment of Δt gives an incremental rotation matrix $\Delta\boldsymbol{R}$ for rotating the local reference system from time t to a future point in time $t + \Delta t$. $\boldsymbol{R}^{t+\Delta t}$ in Equation (3.15a) denotes the rotation matrix from the local coordinate system's original orientation at time t_0 to its current orientation of basis vectors $\boldsymbol{e}^{t+\Delta t}$ at time $t + \Delta t$, as Equation (3.15b) shows [28].

$$\boldsymbol{R}^{t+\Delta t} := \Delta\boldsymbol{R} \cdot \boldsymbol{R}^t \tag{3.15a}$$

$$\boldsymbol{e}_\alpha^{t+\Delta t} := \boldsymbol{R}^{t+\Delta t} \cdot \boldsymbol{e}_\alpha^{t_0} \tag{3.15b}$$

Similar to the strain increment of Equation (3.12), the local velocity-gradient $\boldsymbol{\mathcal{L}}$ is decomposed into elastic $\boldsymbol{\mathcal{L}}_{\mathrm{el}}$ and viscoplastic $\boldsymbol{\mathcal{L}}_{\mathrm{vp}}$ components by Equation (3.16).

$$\boldsymbol{\mathcal{L}} := \boldsymbol{\mathcal{L}}_{\mathrm{el}} + \boldsymbol{\mathcal{L}}_{\mathrm{vp}} \tag{3.16}$$

The gradients $\boldsymbol{\mathcal{L}}_{\mathrm{el}}$, $\boldsymbol{\mathcal{L}}_{\mathrm{vp}}$ are defined by Equation (3.17a) and Equation (3.17b) respectively, by making use of the strain rates $\dot{\boldsymbol{\varepsilon}}_{\mathrm{el}}$, $\dot{\boldsymbol{\varepsilon}}_{\mathrm{vp}}$ as well as total rotation-rate of the polycrystalline material point $\dot{\boldsymbol{\omega}}$ [28].

$$\boldsymbol{\mathcal{L}}_{\mathrm{el}} := \dot{\boldsymbol{\varepsilon}}_{\mathrm{el}} + \dot{\boldsymbol{\omega}} \tag{3.17a}$$

$$\boldsymbol{\mathcal{L}}_{\mathrm{vp}} := \dot{\boldsymbol{\varepsilon}}_{\mathrm{vp}} \tag{3.17b}$$

For convenience, Seguardo et al. [28] assigned the full rotation rate $\dot{\boldsymbol{\omega}}$ to the elastic part of the velocity gradient via Equation (3.17a).

Assuming the plastic strains to be much larger than the elastic ones, the deformation can be considered to be isochoric, i.e. the determinant of the deformation gradient $\boldsymbol{\mathcal{F}}$ is constant [28]. Refer to Section 2.3.2. The polycrystal elastic stiffness and the viscoplastic strain increment are calculated by the means of the VPSC approach, in the system of the rotated basis $\boldsymbol{e}_\alpha$. In order to express these magnitudes in the global reference system $\boldsymbol{e}_i^{\mathrm{gl}}$ introduced in Section 1.2.1, $\boldsymbol{R}^{t+\Delta t}$ is needed. Explicitly, this means that the strain increment $\Delta\boldsymbol{\varepsilon}$ for the solid body deformation is obtained by rotation Equation (3.18) from the strain increment in the local coordinate system $\boldsymbol{\varepsilon}^{\mathrm{px}}$, which the VPSC approach has calculated through the means given in Section 2.3.1.

$$\Delta\boldsymbol{\varepsilon} = (\boldsymbol{R}^{t+\Delta t})^\top \cdot \Delta\boldsymbol{\varepsilon}^{\mathrm{px}} \cdot \boldsymbol{R}^{t+\Delta t} \tag{3.18}$$

Finally, the stress $[\boldsymbol{\sigma}^{\,\mathrm{px}}]_R$ expressed in the rotated axes $\boldsymbol{e}_\alpha$, that needs to be given at each time step $t+\Delta t$ for the VPSC approach, is calculated from current stress $\boldsymbol{\sigma}^t$ the FEM model provides at time t for the element in question, via Equation(3.19) [28]. The Cauchy stress deviator $\boldsymbol{\sigma}'$, first introduced in Section 1.2, can be obtained via Equation (1.9) from the stress tensor $\boldsymbol{\sigma}$.

$$[\boldsymbol{\sigma}^{\,\mathrm{px}}]_R^{t+\Delta t} = \boldsymbol{R}^{t+\Delta t} \cdot \underbrace{(\boldsymbol{\sigma}^t + \boldsymbol{C} : ([\Delta\dot{\boldsymbol{\varepsilon}} - \Delta\dot{\boldsymbol{\varepsilon}}_{\mathrm{vp}}]\Delta t))}_{[\boldsymbol{\sigma}^{\,\mathrm{px}}]^{t+\Delta t}} \cdot (\boldsymbol{R}^{t+\Delta t})^\top \tag{3.19}$$

Note that while this approach theoretically allows for non-constant strain-rates $\dot{\boldsymbol{\varepsilon}}$, the simulations in this thesis are not time-dependent as a constant global strain is applied, which was mentioned in the beginning of Section 2.3.2. Nonetheless, may the strain-rate still vary locally from element to element due to the sample geometry and the applied direction of loading.

3.3.2 Element Stiffness Matrix

The following discussion for the element stiffness matrix notation by Segurado et al. [28] focuses on the small-strain notation. However, Segurado et al. note that this is also applicable for finite deformations by replacing the small-strain variables with their large-deformation ones in the localized rotated system $\boldsymbol{e}_\alpha$, discussed in Section 3.3.1.

A VPSC polycrystal (px) shall be defined at each finite-element k, each inside a localized rotational system $[\boldsymbol{e}_\alpha]_k$. Note, Section 3.2.2 has mentioned the global stiffness matrix to be calculated iteratively over each element k. The load increment is controlled by the time and after the deformation problem has been solved at time t, the solution for the next increment requires the polycrystal to provide a tangent stiffness matrix $\boldsymbol{C}_k^{\mathrm{tg}} := \Delta\boldsymbol{\sigma}_k/\Delta\boldsymbol{\varepsilon}_k$, in order for the FEM-model to compute an initial guess for the nodal displacements at $t+\Delta t$ [28]. The predicted strain increments for each element are the initial guesses for the localized VPSC calculation, together with the stress $[\boldsymbol{\sigma}^t]_k$ and the internal state variables, i.e. orientation $[\boldsymbol{R}^{t+\Delta t}]_k$, morphology and the hardening state of each statistical representative grain in the HEM [28]. The stress $[\boldsymbol{\sigma}^{\,\mathrm{px}}]_R^{t+\Delta t}$ in the localized rotational system, used for the VPSC calculations of Section 2.3.1, which obtains local microstructure evolution and the polycrystals stress response, is calculated by Equation (3.19). The choice of the elastic stiffness $\boldsymbol{C}_k$ for the current polycrystal (px), i.e. the current element k, consisting of the statistical representative grains (gr), is obtained by the elastic self-consistent estimate of Equation (3.20),

$$\boldsymbol{C}_k = \left\langle [\boldsymbol{C}_k^{\mathrm{gr}}]^{-1} : [\boldsymbol{B}_k^{\mathrm{gr}}]^{-1} \right\rangle^{-1} \tag{3.20}$$

where $\boldsymbol{C}_k^{\mathrm{gr}}$ and $\boldsymbol{B}_k^{\mathrm{gr}}$ are the elastic stiffness and stress localization tensors of the grains (gr) [28]. Finally, the tangential stiffness the VPSC-based UMAT provides to the FEM model is calculated by Equation (3.21),

$$\boldsymbol{C}_k^{\mathrm{tg}} = [\boldsymbol{C}_k^{-1} + \Delta t \boldsymbol{M}^{\,\mathrm{px}}]^{-1} \tag{3.21}$$

where $\boldsymbol{M}^{\,\mathrm{px}}$ is the result for the polycrystal relation tensor, calculated by Equation (2.30), that has achieved convergence.

3.3.3 Overview UMAT-FEM Interaction

Figure 3.3 provides a graphical representation, both of the dependencies between the VPSC-UMAT and the FEM framework of LS-DYNA®, that were discussed in Section 3.3.2. Furthermore, Figure 3.3 clarifies that VPSC and LS-DYNA® need independent micro- or macrostructural material information. For example: crystalline properties and slip modes are provided for VPSC, while the mesh and boundary conditions are needed for FEM. Accordingly, the UMAT and the Finite Element Method (FEM) solver both produce separated output as well.

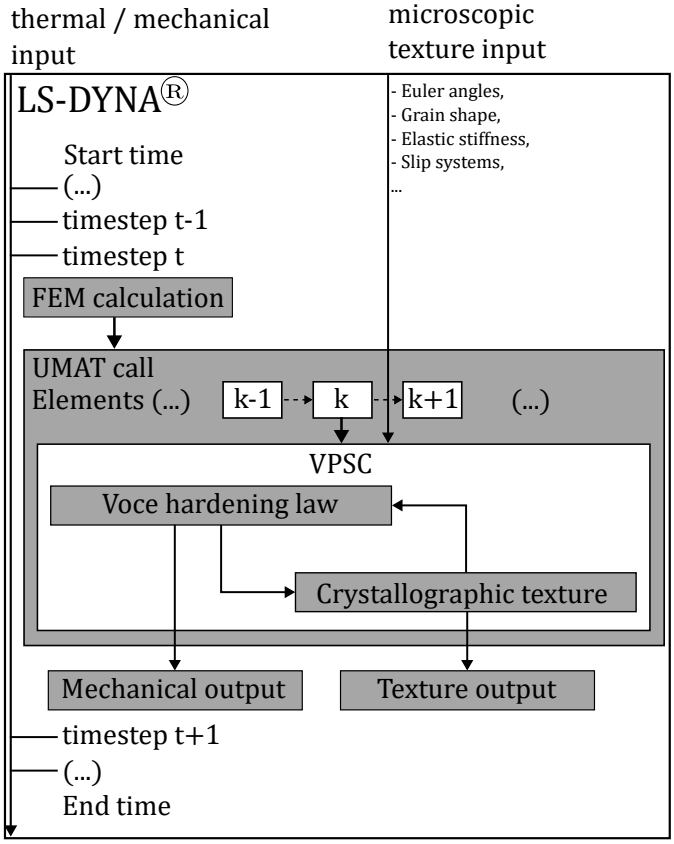

Figure 3.3: VPSC-FEM as UMAT with Voce hardening law inside the macroscopic FEM simulation.

3.4 Material Data and Reference Systems

The material used was a industrially produced EN AW-5754 cold rolled metal sheet with a thickness of 1.5 mm.[3] This alloy consists of an aluminium basis, with a small amounts (2.6 % to 3.6 %) of magnesium [13].

[3] acronyms stand for European Norm (EN) and Aluminium Wrought (AW)

3.4.1 Reference Systems and Samples

The choice of the reference systems discussed in Section 1 and Section 2 can be arbitrary. For the material measurement, multiple tensile test specimen were cut-out at an 45° rotation around ND in the RD-TD plane of the rolled aluminium sheet sample. Analytically, the tensile specimen's local coordinate system $\boldsymbol{e}^{\mathrm{ts}}_{1,2,3}$ is therefore directly related to the metal sheet sample by applying the rotation matrix $\boldsymbol{R}(45°)$, defined by Equation (2.6a), onto $\boldsymbol{e}^{\mathrm{s}}_{1,2,3}$. Figure 3.4 displays a sketch of the rolled metal and the position of the cut-out tensile test specimens, as well as a mark on the cross-section of the specimens that were EBSD-measured. For details regarding the mechanical tests as well as the EBSD, refer to Section 3.4.2.

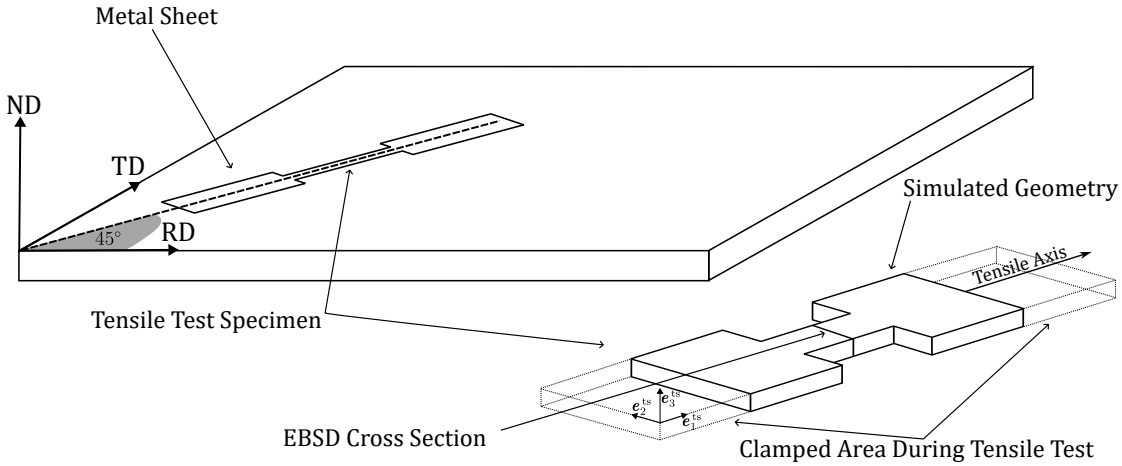

Figure 3.4: Sketch of cut-out for the tensile tests from the rolled aluminium sheet, with EBSD-measurements performed at sample cross-sections, as was done by LKR.

3.4.2 Material Tests and Measurements

All material measurements were done by personnel at LKR, with minimal involvement of the thesis author. Processed texture data was provided for the simulations in this thesis, together with the flow stress curves of the tensile tests. Below are given some details on the testing and measuring, as well as the data manipulations that had to be done beforehand.

The Mechanical Testing composed of uniaxial tensile tests at a controlled constant strain-rate $\dot{\varepsilon}$ of $0.01\,\mathrm{s}^{-1}$ using a DIL805A/D/T quenching and deformation dilatometer, with specimens being deformed until fracturing occurred. Tensile tests were taken for pre-set specimen temperatures T_s of 100 °C, 150 °C, 200 °C and 250 °C as well as at Room Temperature (RT) . Temperatures were regulated by a hollow inductive heating and cooling coil during the testing, with cooling being accomplished by directing nitrogen through the interior of said coil directly onto the specimen. Current specimen temperature

was recorded by the DIL805A/D/T during the tests through a soldered thermocouple, mounted onto the middle of the tapered specimen part. The uncertainty of the temperature measurements are given by the standard deviation of the recorded temperature in every time-step. An additional tensile test at a pre-set constant strain-rate of $0.01\,\mathrm{s}^{-1}$ was carried out to provide the reference data referred to as verification experiment later in Section 4, where the specimen was first heated up and during the tensile load and linearly cooled down from approximately $(250.2 \pm 0.4)\,^{\circ}\mathrm{C}$ to $(60.5 \pm 0.9)\,^{\circ}\mathrm{C}$ in 29.2 s and UTS was observed after 21.9 s at $(106.0 \pm 0.9)\,^{\circ}\mathrm{C}$. Figure 3.5 displays the experimental setup of the temperature controlled tensile tests, with one of the specimen shown in Figure 3.5a and the complete configuration before initiating the tests in Figure 3.5b.

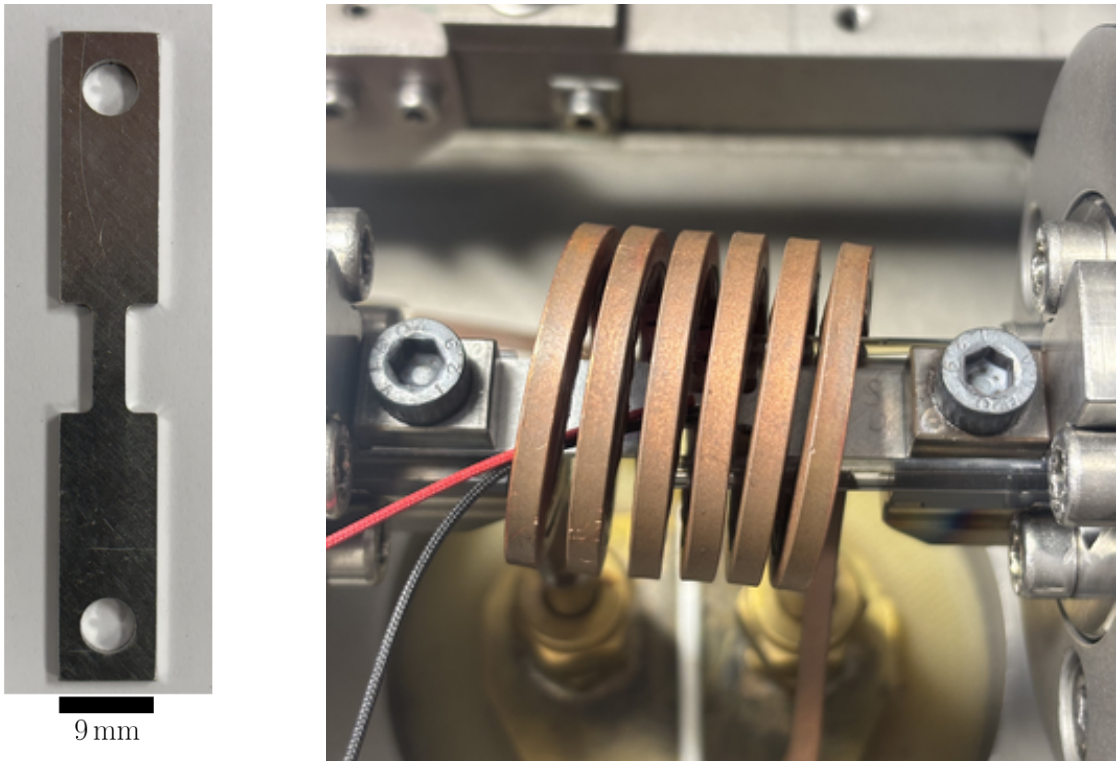

(a) Specimen (b) Heating/cooling coil with specimen and thermocouple

Figure 3.5: Pre-deformed tensile test EN AW-5754 specimen (a) with setup for temperature controlling inside DIL805A/D/T (b).

The EBSD Measurements of the samples were taken in the cross-section in the middle of the sample, by a Tescan Mira 3 field emission scanning electron microscope, operated with an acceleration voltage of 20 kV at a working distance of 20 mm, using the highest settable beam intensity. Images were taken using a velocity EBSD camera from EDAX utilizing a view-field of $(500 \times 370)\,\mu\mathrm{m}^2$ at a step-size of 0.25 µm. The texture data were exported as grain files using the software OIM analysis version 8.6, after a performed

clean-up using the NPAR routine and one iteration of grain dilatation with a grain tolerance angle of 5°, a minimum grain size of 2 px and a neighbour confidence index correlation with a minimum value of 0.1. One such measurement was taken of a pre-tensile specimen, with the obtained textures rotated to be in-plane of the metal sheet, RD-TD.

3.4.3 Pre-processing of Texture Data

To ensure a correct interpretation of the measured EBSD data, some pre-processing steps are required. First, the measured sample coordinate axes of the metal sheet deviate slightly from the manufacturing process directions (RD, TD and ND) due to sample preparation and the measurement setup. This was corrected by symmetrically aligning the pole figures around the 45° axis using the alignment algorithm described in [24]. Afterwards, to minimize computational costs, the 3221 identified individual grain orientations were reduced to 104. This was done by using the clustering algorithm developed by Theil in [33] and the subsequent work [16] for texture/EBSD data (using a cluster radius of 0.4). It was demonstrated in [14, 21], that about 100 grains are sufficient to represent a texture of a FCC crystal aggregate. This same initial texture was used for all presented simulations and was applied to all elements in the sample geometry. Below, Figure 3.6a shows the Inverse Pole Figure (IPF)-map measured of a initial, non-deformed tensile specimen, by projecting the Normal-Direction to the local crystallographic planes. Figure 3.6b and Figure 3.6c display the Pole Figure (PF) of the full measured texture and the reduced one provided for the simulations respectively. Note, each of the grains in the PFs to have an assigned weight, corresponding to the area such (clustered-)orientations occupy on the IPF-map, which is not shown here.

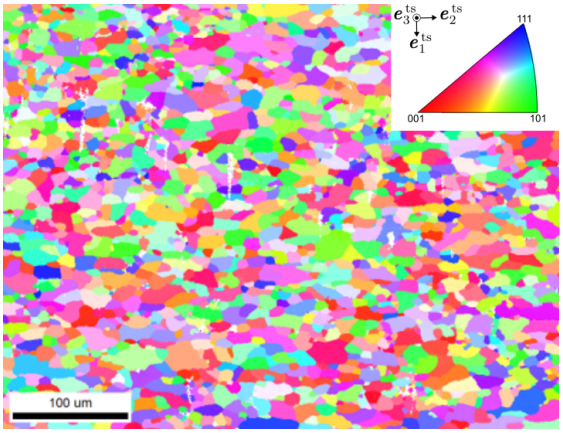

(a) IPF-map of projected ND (e_3^{ts})

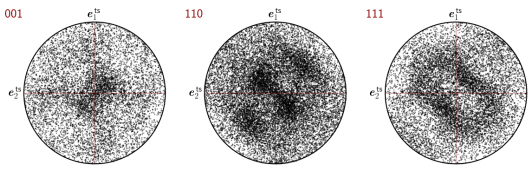

(b) PF of original, aligned texture

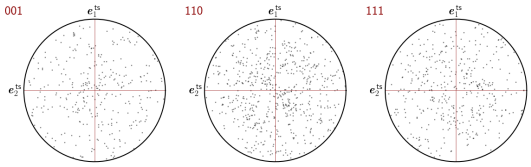

(c) PF of reduced input texture

Figure 3.6: EBSD orientation (texture) map of EN AW-5754 tensile specimen cut-out (a), together with the PF of the original (b) and the representative clustered texture (c), each showing the projected poles of crystallographic planes {0 0 1}, {1 1 0}, {1 1 1} to the e_1^{ts}-e_2^{ts} plane.

3.5 Voce Support Points Optimizations

As support points for the temperature interpolation, Voce hardening parameters that best describe the macroscopic material behaviour at a certain fixed temperature of the tensile tests were searched. For this purpose, VPSC-FEM simulations of the tensile tests were run under the supervision of the probabilistic analysis tool LS-OPT® version 7.0.2 for varying Voce values. By iteratively comparing the load/(force)-displacement curve of the tensile specimen with the data obtained from the corresponding simulations, a parameter set $\tau_0, \tau_1, \theta_0, \theta_1$, of the single active FCC slip mode is obtained at each temperature, that best describes the observed macroscopic stress-strain curve for the provided initial texture.

The main steps of the optimization included: First, an estimated set of start parameters was defined manually, then LS-OPT® run 8 LS-DYNA® tensile test simulations, using the VPSC-UMAT with varying combinations of Voce values, obtained via a linear metamodel sampling. After completion, each of the resulting load-displacement curves were compared to the tensile test measurement data with the Partial Curve Mapping (PCM) algorithm. For the optimization, the Leapfrog Optimizer for Constrained minimization (LFOPC) algorithm, with the default values given in LS-OPT® was chosen. After the first iteration, new estimations of parameter combinations were provided for another round of 8 LS-DYNA® runs. The termination criteria was set, if either the PCM discrepancy d fell below the value of 0.0010, when comparing load-displacement curves or if a maximum number of 3 such iterations has been executed. Finally, a verification run was executed with the best fitting estimate of the Voce parameters, which is based on the values screened in the iterations beforehand. The starting parameters for the optimizations as well as their constraints were manually set in the beginning according to experience from previous runs. A brief summary regarding the optimization approach used, is laid out in Section 3.5.1.

3.5.1 Optimization Method and Curve Discrepancy

The beginning of Section 3.5 mentions the settings used for the optimization tool, whose implications are briefly outlined in the following paragraphs. Note, more detailed information regarding the inner-workings of the analysis tool LS-OPT® to be found in the User's Manual by Stander et al. [32].

LFOPC in LS-OPT® refers to the Leapfrog Optimizer for Constrained minimization algorithm by Snyman [30], a gradient method that generates a dynamic trajectory path, from any given starting point, towards a local optimum [32, 30]. The leap-frog refers to a method that seeks the minimum of a function consisting of n variables by considering a particle in a n dimensional force field. The potential energy of the particle at point $x(t)$ is taken at a time t, as a function $f(x)$, which needs to be minimized. Therefore, the method requires the solution of the equations of motion for a particular particle with initial velocity and position. An approximated trajectory of the particle is following computed by using the so-called leap-frog (Euler-forward/Euler-backward) method [29, 30]. The constraint to the optimization problem is included by a penalty function that needs to be minimized.

PCM was chosen because it preserves the arc length. It can compare two curves of unequal geometric length and hysteresis but ignores noise by mapping one the points of one curve onto the other [32]. In more detail, PCM calculates the volume/area between a curve a and a longer one, a'. The volume between a and a' is taken as a measure of the discrepancy d. LS-OPT® calculated d by first sentimentalizing a and a' into pieces, defined as a straight line connection between two consecutive points, which means a curve consisting of m points results in $m-1$ segments [32]. For each segment i, a segmental length $\tilde{s}_i$ calculated is calculated, that is scaled and normalized regarding to the shorter curve a. A curve segment i on a then corresponds to a segment i on a' of same length. Through the resizing of segments i from a' the individual mismatch errors, i.e. pointwise distances δ_i, between the scaled points and normalized point pairs (X, Y) of curves a and a' are calculated by Equation (3.22a). The volume component ν_i of each segment is following calculated by Equation (3.22b). Summing ν_i up over all m points, gives a total, normalized curve mismatch error for the discrepancy $d(a, a')$ between the two curves a and a' by Equation (3.22c) [32].

$$\delta_i = \sqrt{(X' - X)^2 + (Y' - Y)^2} \tag{3.22a}$$

$$\nu_i = \frac{\delta_i + \delta_{i-1}}{2} \cdot \tilde{s}_i,\ \nu_1 = 0;\ i \in [2, m] \tag{3.22b}$$

$$d(a, a') = \sum_{i=1}^{m} \nu_i \tag{3.22c}$$

Note, mismatch errors much lower than one are said to be expected, for reasonably matching curves [32].

3.5.2 Interpolation at Temperature Change

The Voce values are provided for the different slip modes, through a new input file of name given in the VPSC's main settings file (vpsc7.in). This additional microstructural input file is phrased at the FEM-software's call of the UMAT and contains a set of Voce values τ_0, τ_1, θ_0 and θ_1 at a given temperature T. Each set refers to an indexed slip mode, which consists of multiple crystallographically equivalent slip systems, as explained in Section 2.2.2. These Voce values are used as support points to linearly interpolate for any occurring temperatures, that might not have been especially provided, in-between. Information regarding the slip systems are given in the crystal properties file of VPSC [34] and any there defined hardening parameters are ignored in the CRSS calculation, as they are superseded by the temperature Voce value list of the new input file. The input data file for the Voce values needs to conform to the schema depicted in Figure 3.7. Note, the range of the given temperature Voce values is expected to be set accordingly for the material and specific problem to be simulated. Similar to VPSC, the implementation expects one such file for each phase in the polycrystalline material.

```
$ - Lines starting with $ will be ignored as comments
$ - One Voce value block is read in per slip system
$ - Each block beginning must be marked with *
$ - The order of slip systems must be the same as given in the single
$   crystal properties file, that is named in vpsc7.in
$ The support point block consist of the follwing structure:
*slip mode 1
temperature tau0 tau1 thet0 thet1
temperature tau0 tau1 thet0 thet1
 ...
*slip mode 2
 ...
```

Figure 3.7: Required format of input file for Voce parameters of slip modes at certain temperatures.

For handling the Voce value support point blocks, a Fortran type was developed, where an instance of the type is initialized for each provided Voce parameter input file.

3.5.3 Calculating the CRSS

The CRSS calculation is an adaptation of the implemented extended Voce hardening law subroutine used by VPSC. However, instead of the same Voce values being supplied for all slip systems of a certain slip mode of a polycrystal at a phase, an interpolation for each of the 4-Voce values is done first: Between two provided temperature Voce values of the input file (see Figure 3.7) as support points, a direct linear interpolation takes place to obtain an estimated Voce hardening for a slip mode. The linear interpolation gives estimated values $\tau_0^{\mathrm{sl}}(T^k)$, $\tau_1^{\mathrm{sl}}(T^k)$, $\theta_0^{\mathrm{sl}}(T^k)$ and $\theta_1^{\mathrm{sl}}(T^k)$ for a slip system (sl) at temperature T^k of the current element k. The idea is for the grain average flow-stress curve, of the polycrystal to describe the materials behaviour approximately, if a texture-evolution and a tensile test measurement had taken place at this exact temperature. Afterwards, the usage of the CRSS follows the same procedure, as was originally implemented in VPSC. Another important difference to the original VPSC implementation is that the calculation of the CRSS is done directly by Equation (2.18), using the new estimated values, instead of the original incremental approach by Equation (2.19). It further is noted, that therefore latent hardening through $h^{\mathrm{sl,sl'}}$ is not considered. Should the temperature of k fall below or exceed the temperature range of the Voce support points given for the slip modes, the highest/lowest temperature set given is used, to proceed with the CRSS calculation and a warning message is logged. To prevent memory corruption if multiple instances of the CRSS calculation are called in the parallelized environment and to enable easier further expansion, the interpolation calls are embedded directly into the data type that hold the information provided by the Voce value input file of Figure 3.7, i.e. an object-oriented programming approach was chosen.

The new system of Voce value handling is enabled by a flag in the LS-DYNA® input files that is passed down to the UMAT call. The new method is used for the cooling simulation but not the optimizations simulations, as they are meant to be at fixed temperatures.

3.6 Simulation Input

Section 3.6.1 is dedicated to the input data relevant for LS-DYNA®, while Section 3.6.2 lists the microstructural information needed for the VPSC UMAT calls.

3.6.1 FEM Simulation

The global coordinate system for FEM $\boldsymbol{e}^{\mathrm{gl}}_{1,2,3}$ was set to be the one of the tensile specimens ($\boldsymbol{e}^{\mathrm{ts}}_{1,2,3}$), i.e. it was rotated by 45° around ND for the tensile axis to face in the x-direction ($\boldsymbol{e}^{\mathrm{gl}}_{1}$). This becomes apparent if Figure 3.4 of the sample cut-out and Figure 3.8 of the simulated geometry are compared and allows to provide the initial texture of the material from the cross section as described in Section 3.4.2, after the pre-processing of Section 3.4.3 has been done. Because the upper and the lower part of the tensile specimen are hold firmly in place by the tensile test machine (clamped down areas in Figure 3.4), the mesh needed to reflect the reduced degrees of freedom for these areas. This was done by simulating only the free-standing part of the specimen and applying corresponding Dirichlet boundary conditions. No displacement was set to occur for all nodes on boundary area $\mathcal{R}_0$, i.e. they were fixed in space ($\rightarrow \boldsymbol{u}_0 = \vec{0}$).

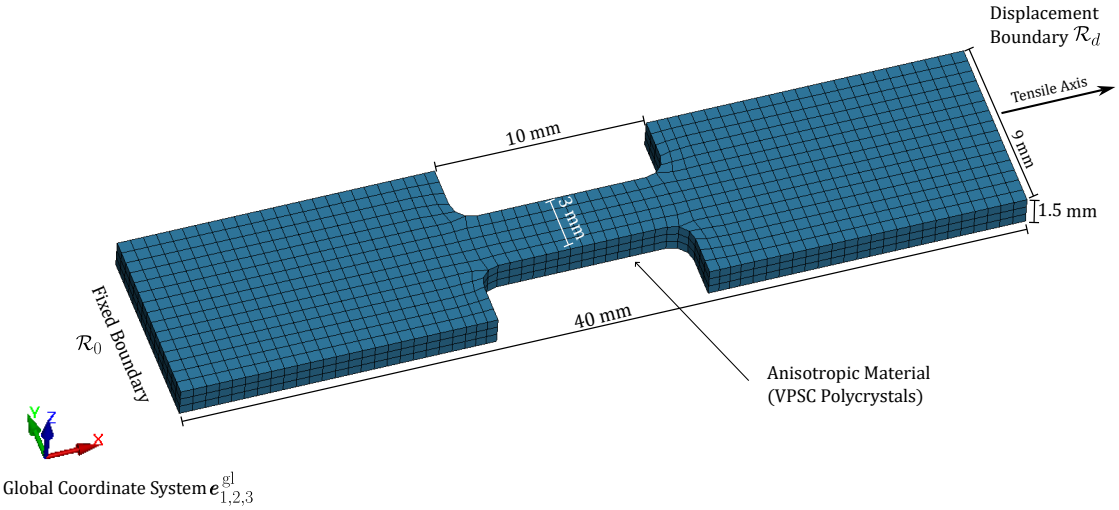

Figure 3.8: Simulated geometry using VPSC with boundaries and measurements.

However, to avoid unrealistic transitions of textures changes in the elements of the boundary nodes, which would result from the reduced degrees freedom for said nodes, only the middle top ($x, y = 0$ with $u_{1,2} = 0$) and bottom nodes ($x, y, z = 0$ with $u_{1,2,3} = 0$) had additional boundaries applied, allowing small movements of the clamped specimen part.

A constant velocity boundary condition, set by a displacement vector $\boldsymbol{u}_d$ in x-direction, is applied at time t_{sim} on the boundary surface elements of $\mathcal{R}_d$. Equation (3.24), defining $\boldsymbol{u}_d$, is given by the assumption that most of the deformation is going to happen at the thinnest part of the specimen, which had a pre-deformation length $l_0 = 10\,\text{mm}$ along the tensile direction ($\boldsymbol{e}_1^{\text{gl}}$). The 1D true strain $\varepsilon_t = \ln \frac{l_0+u}{l_0}$, occurring through a deformation of length l_0 by u, is given by Equation (3.23) through the 1D strain-rate $\dot{\varepsilon} = \frac{\partial \varepsilon}{\partial t}$,

$$\varepsilon_t = \ln \frac{l_0 + u}{l_0} = \int_{t_0}^{t_1} \dot{\varepsilon}\, \mathrm{d}t \tag{3.23}$$

where the true strain in the time from t_0 to t_1 is searched. Partially integrating Equation (3.23) and noting $\dot{\varepsilon}$ to be constant, i.e. $\frac{\partial \dot{\varepsilon}}{\partial t} = 0$, leads to the current displacement u_1, which is applied along the tensile direction. Following, Equation (3.24) gives the vector $\boldsymbol{u}_d$ at the simulated time $t_{\text{sim}} = t_1 - t_0$,

$$\boldsymbol{u}_d(t_{\text{sim}}) = \begin{pmatrix} l_0 \cdot \exp\left(\dot{\varepsilon} \cdot t_{\text{sim}}\right) - l_0 \\ 0 \\ 0 \end{pmatrix} \tag{3.24}$$

where $\dot{\varepsilon}$ is set to $0.01\,\text{s}^{-1}$ for fitting the applied controlled constant strain-rate of the tensile tests.

Solely the polycrystalline VPSC-UMAT, was responsible for the anisotropic material behaviour. For obtaining the Voce support points, fittings of the load-displacement curves, as described in Section 3.5, were done for the 5 tensile tests of controlled temperature.

As a verification simulation, a uniaxial tensile test simulation was afterwards repeated for the case of non-constant temperatures. By linearly decreasing the temperature of the tensile specimen experimentally at each time step and setting it for the simulation, the proposed method interpolated corresponding Voce hardening values for the current element temperature at each time step. Note, the verification specimen was assumed to be at uniformly cooled, as was done for the verification experiment of Section 3.4.2. Exact hardening parameters were interpolated from the provided support points, obtained from the optimizations. The verification simulation modelled the verification experiment until the time of occurring UTS, i.e. before the start of necking. Refer to Section 2.3.3.

The mechanical time step size for simulations performed by the optimizer was set to $\Delta t = 0.3\,\text{s}$. However, due to the instabilities observed in the verification run of the $T_s = 250\,^{\circ}\text{C}$ case, the same material parameters were used to rerun the tensile test simulation using the in the end obtained values for τ_0, τ_1, θ_0 and θ_1 (refer to Section 3.5), with a time step size of $\Delta t = 0.1\,\text{s}$. For the verification experiment simulation of the cooled tensile test, a fixed linear temperature decrease at every mechanical time step of $\Delta t = 0.3\,\text{s}$, starting from $250.2\,^{\circ}\text{C}$ and ending at $106.0\,^{\circ}\text{C}$ was applied uniformly to all finite elements for $21.9\,\text{s}$. The same mesh of 2490 hexahedral linear elements and boundary conditions were used for all simulations.

3.6.2 VPSC Input

The VPSC-input provided isotropic hardening, i.e. $h^{\mathrm{sl,sl'}} = 1$ for all of the 12 $\{1\,1\,1\}\langle 1\,\bar{1}\,0\rangle$ slip systems (sl) of FCC, when referring to Equation (2.19). An effective rate sensitivity exponent $n_{\mathrm{eff}} = 10$ was set. The single crystal elastic constants $C_{11} = 107.3\,\mathrm{GPa}$, $C_{12} = 60.08\,\mathrm{GPa}$ and $C_{44} = 28.3\,\mathrm{GPa}$ were used for all simulations, which were taken from [36] and correspond to their determined values for pure aluminium at 300 K (26.85 °C). The initial texture consisted of 104 weighted grain orientations obtained from the preprocessing, described in Section 3.4.3

The Voce parameter constraints for LFOPC, used by LS-OPT®, were roughly predetermined from previous optimization runs.

4 Results

Section 4.1 gives an overview of the full measurement data sets of the tensile tests, which were used as reference for the simulations done. Following, Section 4.2 provides the results for the Voce parameters as well as their application to the case of non-constant temperature. Finally, Section 4.3 lists additional results from the FEM-simulations, directly comparing the different simulation cases with each other.

4.1 Tensile Test

Figure 4.1a shows the fully measured force(load)-displacement curves by the DIL805A/D/T at Room Temperature (RT), while Figure 4.1b to Figure 4.1e display the measurements at a corresponding pre-set temperature T_s of the specimen. In the verification experiment for the hardening parameter estimation, the tensile test was performed under a linear cool down. Figure 4.1f gives the load curve of the verification experiment and the current specimen temperature at the corresponding displacement.

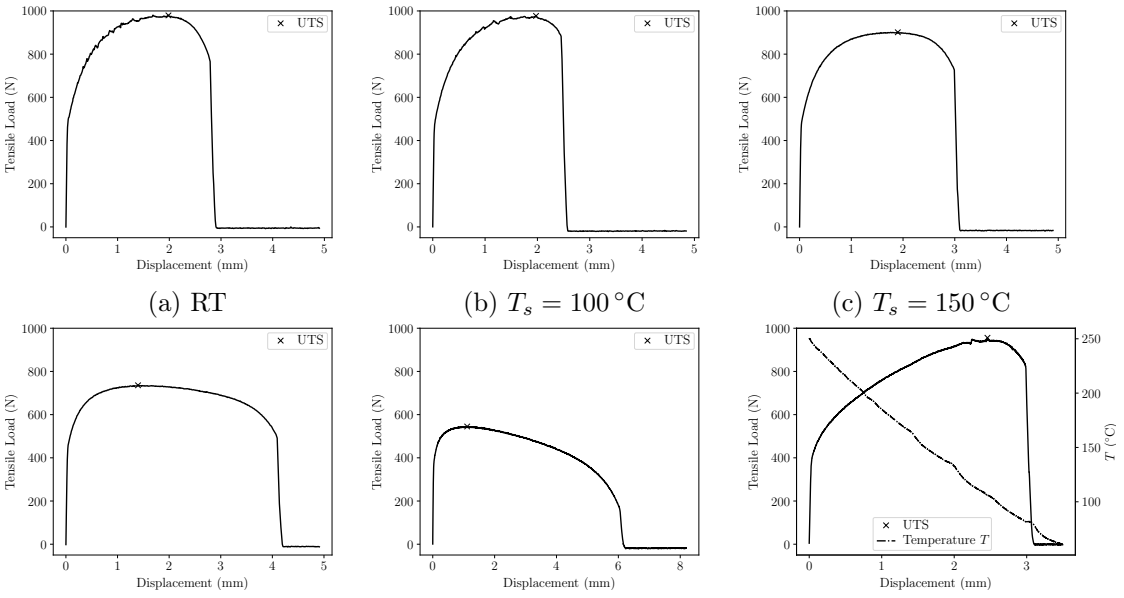

(a) RT (b) $T_s = 100\,°\mathrm{C}$ (c) $T_s = 150\,°\mathrm{C}$

(d) $T_s = 200\,°\mathrm{C}$ (e) $T_s = 250\,°\mathrm{C}$ (f) Verification experiment

Figure 4.1: Force-displacement curves at different temperatures at a constant controlled strain rate of $0.01\,\mathrm{s}^{-1}$, with marked Ultimate Tensile Strength (UTS).

All tensile test specimen were uni-axial loaded until fracture occurred. However, as reference data for the simulations of Section 4.2, loading is only considered until the UTS has been reached.

4.2 Simulation Result Validation

Section 4.2.1 lists the results from the optimizer LS-OPT®. Section 4.2.2 focuses on the simulation of the non-constant temperature to model the verification experiment.

4.2.1 Fitting of Load Curves

Regarding the optimization strategy, the following approach was chosen for the presented results: First, the values τ_0, τ_1, θ_0 and θ_1 were evaluated independently for the RT, $T_s = 150\,°\text{C}$ and $250\,°\text{C}$ cases. Afterwards, the model for the RT case was reused to estimate Voce values for $T_s = 100\,°\text{C}$. For the $T_s = 200\,°\text{C}$ case, the obtained Voce values from $250\,°\text{C}$ to $150\,°\text{C}$ were set for the constraint boundaries.

Following, Table 4.1 provides the corresponding average temperature $\bar{T}$ of the specimen during the tensile test, i.e. the temperatures the Voce values (τ_0, τ_1, θ_0, θ_1) were actually optimized for. The fluctuations of $\bar{T}$ are noted by the standard deviation of the time measurement series. PCM discrepancies d, calculated by LS-OPT® for comparing the simulation result to the corresponding measured load curve, are listed in Table 4.1 as well.

T_s	$\bar{T}$ (°C)	τ_0 (MPa)	τ_1 (MPa)	θ_0 (MPa)	θ_1 (MPa)	d
RT	23.7 ± 0.2	80.20	73.98	746.45	23.25	0.0030
100 °C	100.3 ± 0.9	79.49	72.28	732.72	32.40	0.0010
150 °C	150.3 ± 0.7	73.14	68.63	682.75	28.10	0.0002
200 °C	200.2 ± 0.4	66.80	49.32	551.59	13.97	0.0001
250 °C	249.9 ± 0.4	57.48	28.80	457.18	8.47	0.0080

Table 4.1: Obtained Voce support points of the best fit and PCM discrepancy d.

Figure 4.2 includes the load-displacement curves of the pre-set specimen temperatures T_s in Figure 4.1a to Figure 4.1e, up to the beforehand marked UTS. The optimized curves of the verification run shown in Figure 4.2 are the result of the tensile test simulations done with the in Table 4.1 listed Voce values (τ_0, τ_1, θ_0, θ_1). The simulated tensile force F_x is given by the total force of the $\mathcal{R}_0$ nodes in the tensile axis direction. It is important to note, while all tensile test simulations through LS-OPT® have been performed with a mechanical time step of $\Delta t = 0.3\,\text{s}$, this discretization proved to be too coarse for the $T_s = 250\,\text{s}$ case. A jump in the force(load)-displacement curve is observed in the verification run in this case, which lead to the tensile test simulation being repeated with a step size of $\Delta t = 0.1\,\text{s}$, shown here, using the same Voce values.

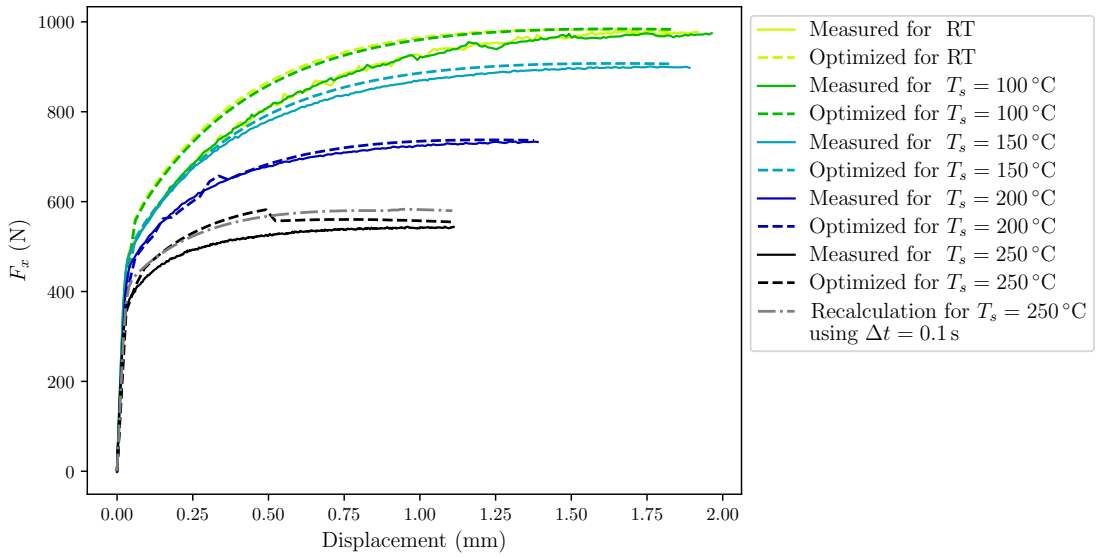

Figure 4.2: Total force F_x over all fixed nodes in tensile axis from best fitted simulations, compared with the strain-hardening loads from tensile test measurements.

Scaling the obtained Voce parameters of Table 4.1 to their respective set for the LFOPC algorithm (displayed in Figure 4.3) provides an impression whether the parameter space was set large enough and how the different constraints compare.

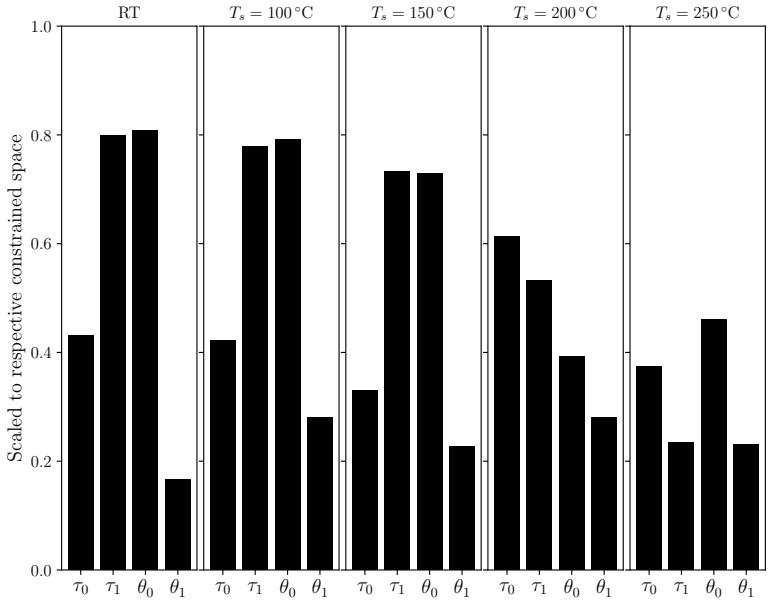

Figure 4.3: Optimized Voce values for the constant temperatures optimizations via LS-OPT®, scaled to their respective constrained spaces.

Table 4.2 shows the correlation matrices of the optimized variables as calculated by LS-OPT®. The dependencies are extracted from the simulation results of the 24 simulations done by the 3 optimization iterations, i.e. 24 different sets of Voce values sampled in the constrained spaces of Figure 4.3 are evaluated for each optimization case. Refer to Section 3.5. The correlations between τ_0, τ_1, θ_0 and θ_1 refer to the influence changing one Voce parameters had on both the calculated PCM discrepancy d and on estimated values for the other parameters. Note, on the one hand, that the correlations are symmetric, and on the other hand, that the correlations between a variable with itself are equal to 1. The defined constrained spaces for LFOPC give different variations of sampled sets between the optimization cases.

	τ_1	θ_0	θ_1	d
τ_0	0.02	−0.01	0.03	−0.54
τ_1		0.10	−0.11	−0.38
θ_0			−0.15	−0.31
θ_1				−0.24

(a) RT and $T_s = 100\,°\mathrm{C}$

	τ_1	θ_0	θ_1	d
τ_0	0.07	0.00	−0.04	−0.29
τ_1		0.07	0.08	−0.43
θ_0			0.04	−0.01
θ_1				−0.24

(b) $T_s = 150\,°\mathrm{C}$

	τ_1	θ_0	θ_1	d
τ_0	−0.07	−0.01	0.05	−0.36
τ_1		0.02	−0.06	−0.17
θ_0			0.07	0.10
θ_1				−0.26

(c) $T_s = 200\,°\mathrm{C}$

	τ_1	θ_0	θ_1	d
τ_0	0.05	0.03	−0.04	0.09
τ_1		0.00	0.05	0.63
θ_0			−0.02	0.40
θ_1				0.05

(d) $T_s = 250\,°\mathrm{C}$

Table 4.2: Correlation matrices for the Voce values τ_0, τ_1, θ_0, θ_1 and their influence on the PCM discrepancy d for the corresponding measured force(load)-displacement curves. Calculated by LS-OPT® using all performed tensile test simulations of the optimization iterations.

4.2.2 Application of Interpolation Method

The cooling simulation and the verification experiment had a controlled/pre-defined steady temperature decline from 250.2 °C to 106.0 °C over a time of 21.9 s. For each temperature change, a new set of Voce parameters was provided to the UMAT. This was done by linearly interpolating between the Voce support points listed in Table 4.1, which leads to a reevaluated CRSS at the corresponding T by Equation (2.18). Refer to Section 3.5.2. The Voce support points are plotted together with the currently estimated values in Figure 4.4.

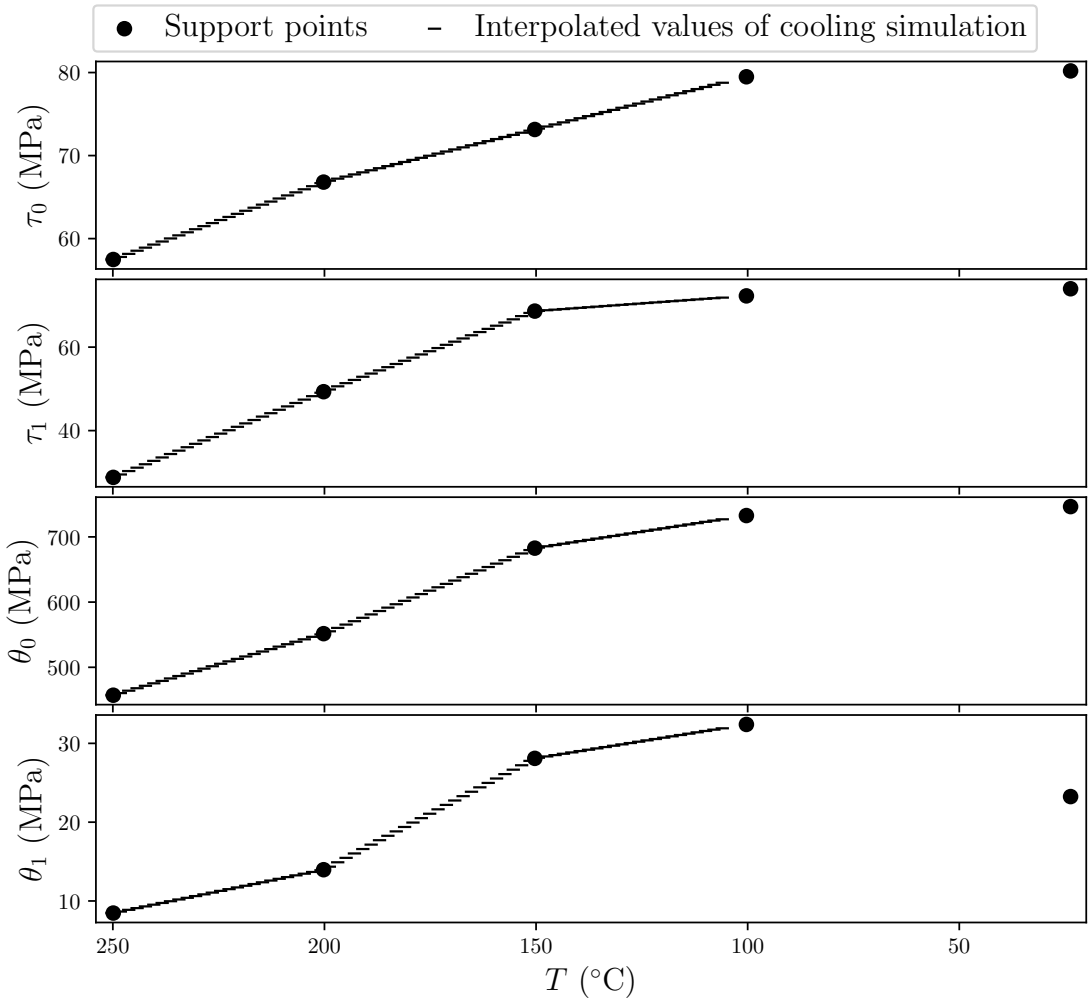

Figure 4.4: Voce value sets (τ_0, τ_1, θ_0, θ_1) estimated for cooling simulation between support points (Table 4.1) at temperature T, plotted for every 5th evaluation.

Due to the controlled strain rate, the cooling in the verification experiment leads to a specific temperature T at each displacement. Equation (3.24) correlates the linear temperature decrease directly to a displacement reached at the simulated time step. Therefore, cross plots between temperature at displacement can be created and are displayed in Figure 4.5a for both the experiment and the cooling simulation. The force(load)-displacement curve of the simulated cooled tensile test are displayed together with the measured one of the verification experiment in Figure 4.5b. As is done in Figure 4.2, the tensile force F_x of the simulation is given by the total force of the $\mathcal{R}_0$ nodes in the tensile axis direction.

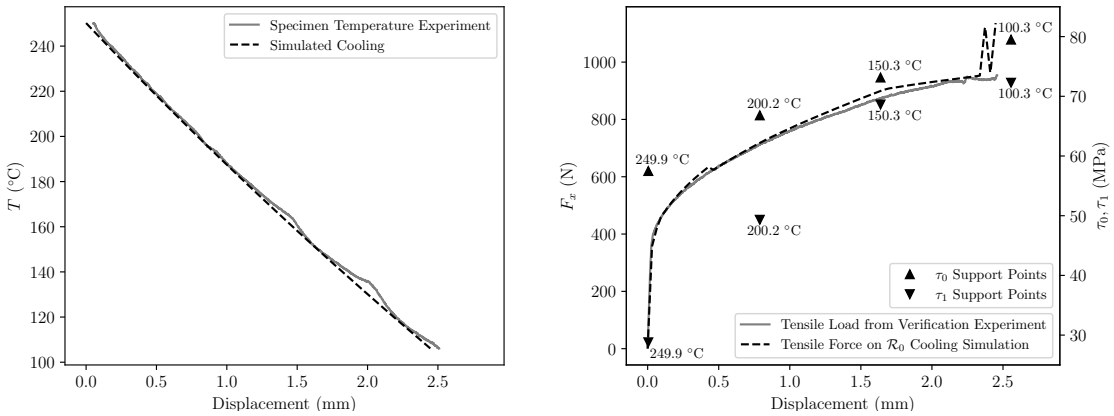

(a) Temperature T of cooling experiment at displacement and set T in simulation.

(b) Force(load)-displacement with estimated and fitted values of τ_0 and τ_1.

Figure 4.5: Comparison of data from verification experiment (cooled tensile test) and the corresponding simulation using the interpolated Voce hardening values.

The CRSS for the slip systems is reevaluated using a different Voce hardening parameter set at every temperature change. To highlight this, Figure 4.5b includes the support points for τ_0 and τ_1 of Table 4.1 and the interpolations done in between.

4.3 Additional Simulation Results

Figure 4.6a to Figure 4.6e display a contour plot of the effective plastic strains $\varepsilon_{\mathrm{p}}^{\mathrm{eff}}$, defined by Equation (2.42a), at the first simulated state of the deformation. The colour scaling is provided in Figure 4.6f. Figure 4.6g to Figure 4.6k display a contour plot of the effective plastic strains at a later state. The time t_{sim} may vary slightly due to the set variable time step size, depending on solution convergence. The respective colour scaling are provided in and Figure 4.6f and Figure 4.6l. Note, following plots for $T_s = 250\,^{\circ}\mathrm{C}$ in Section 4.3 show the $\Delta t = 0.1\,\mathrm{s}$ simulation.

Following, the Von Mises stress $\varepsilon_{\mathrm{p}}^{\mathrm{eff}}$, given by Equation (2.43), is displayed per element in the contour plots of Figure 4.7a to Figure 4.7e for the first printed deformation step, while Figure 4.7g to Figure 4.7k show a later state. Again are respective colour scales provided in Figure 4.7f and Figure 4.7l.

Note that the VPSC UMAT calculated the material stress response for the FEM provided strain in each element. Refer to Section 2.3.1 and Section 3.3.2 for details.

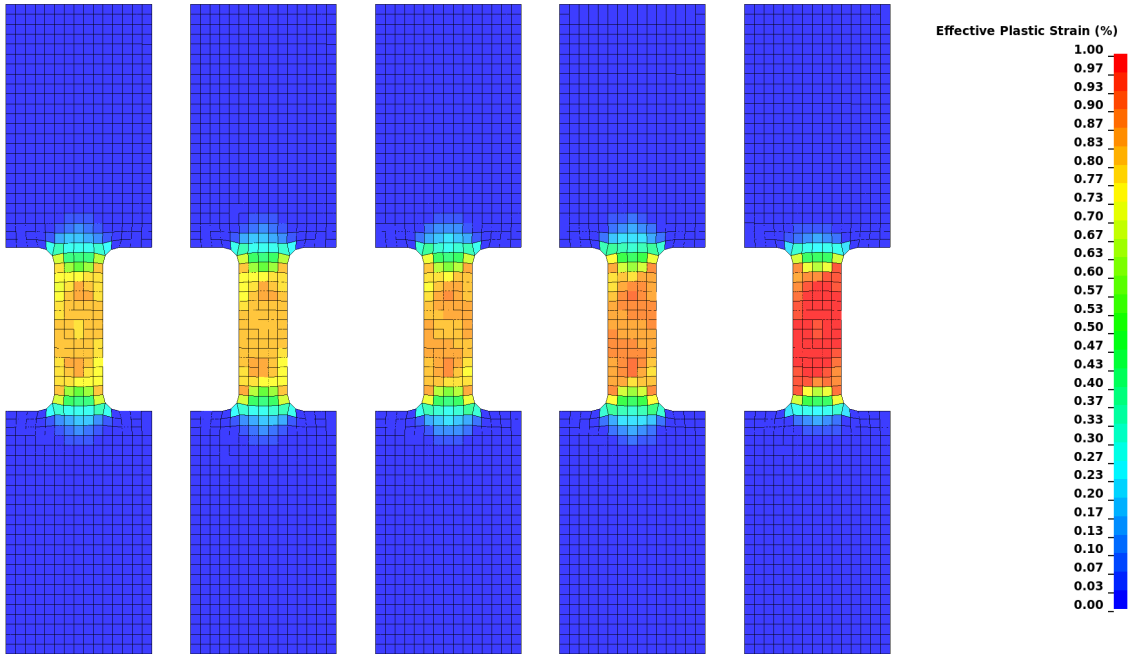

(a) $t_{\text{sim}} = 1.2\,\text{s}$ RT Max: 0.88 % (b) $t_{\text{sim}} = 1.2\,\text{s}$ $T_s = 100\,^{\circ}\text{C}$ Max: 0.88 % (c) $t_{\text{sim}} = 1.2\,\text{s}$ $T_s = 150\,^{\circ}\text{C}$ Max: 0.91 % (d) $t_{\text{sim}} = 1.2\,\text{s}$ $T_s = 200\,^{\circ}\text{C}$ Max: 0.95 % (e) $t_{\text{sim}} = 1.2\,\text{s}$ $T_s = 250\,^{\circ}\text{C}$ Max: 1.38 % (f) Colour scale $\varepsilon_{\text{p}}^{\text{eff}}$ (%) for (a-e)

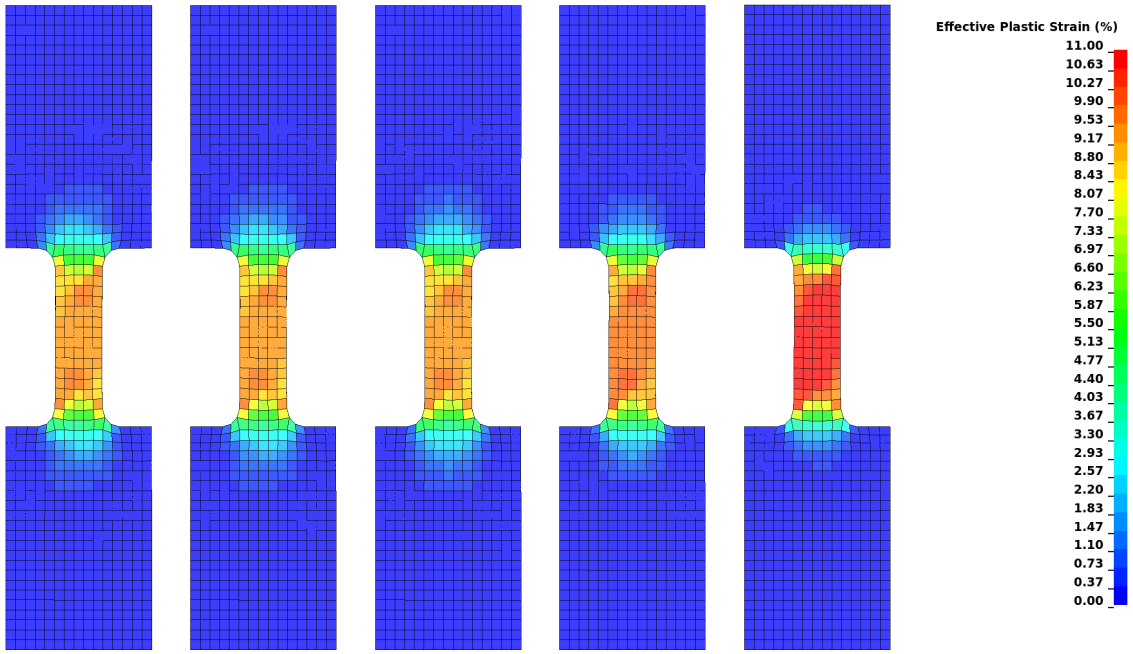

(g) $t_{\text{sim}} = 10.2\,\text{s}$ RT Max: 10.11 % (h) $t_{\text{sim}} = 10.2\,\text{s}$ $T_s = 100\,^{\circ}\text{C}$ Max: 10.10 % (i) $t_{\text{sim}} = 10.2\,\text{s}$ $T_s = 150\,^{\circ}\text{C}$ Max: 10.09 % (j) $t_{\text{sim}} = 10.2\,\text{s}$ $T_s = 200\,^{\circ}\text{C}$ Max: 10.39 % (k) $t_{\text{sim}} = 10.3\,\text{s}$ $T_s = 250\,^{\circ}\text{C}$ Max: 11.34 % (l) Colour scale $\varepsilon_{\text{p}}^{\text{eff}}$ (%) for (g-k)

Figure 4.6: Effective plastic strains $\varepsilon_{\text{p}}^{\text{eff}}$ resulting from Voce values obtained for pre-set temperatures T_s and Room Temperature (RT) after first plotted state (a-e) and after appr. 10 s (g-k). Respective colour scales in (f) and (l).

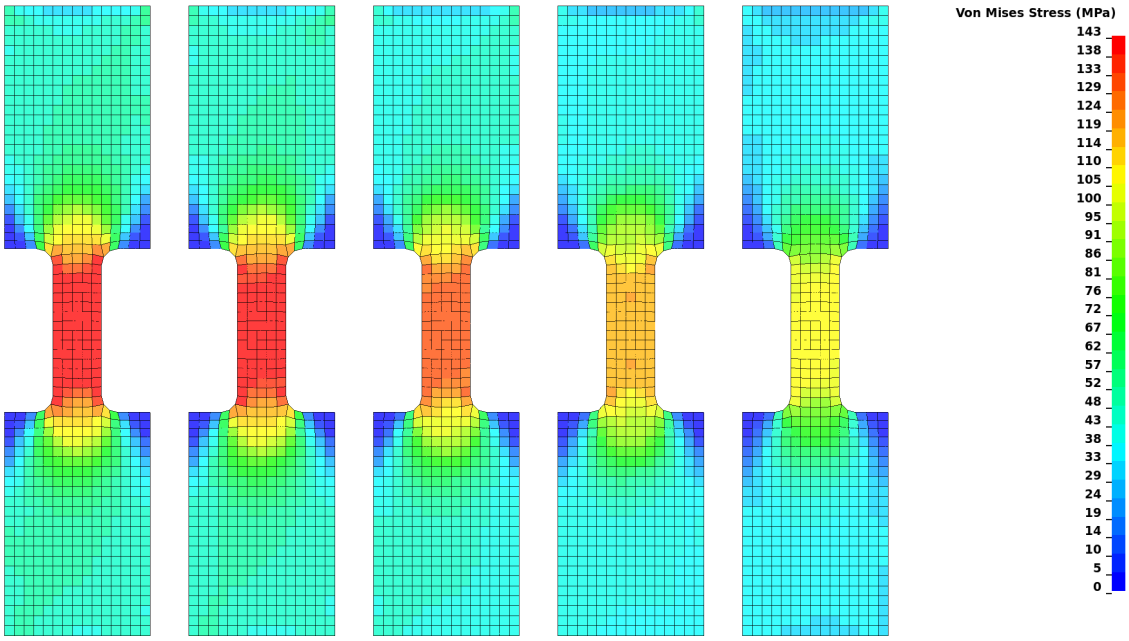

(a) $t_{\text{sim}} = 1.2\,\text{s}$ RT Max: 145 MPa (b) $t_{\text{sim}} = 1.2\,\text{s}$ $T_s = 100\,°\text{C}$ Max: 144 MPa (c) $t_{\text{sim}} = 1.2\,\text{s}$ $T_s = 150\,°\text{C}$ Max: 133 MPa (d) $t_{\text{sim}} = 1.2\,\text{s}$ $T_s = 200\,°\text{C}$ Max: 120 MPa (e) $t_{\text{sim}} = 1.2\,\text{s}$ $T_s = 250\,°\text{C}$ Max: 107 MPa (f) Colour scale σ^{eff} (MPa) for (a-e)

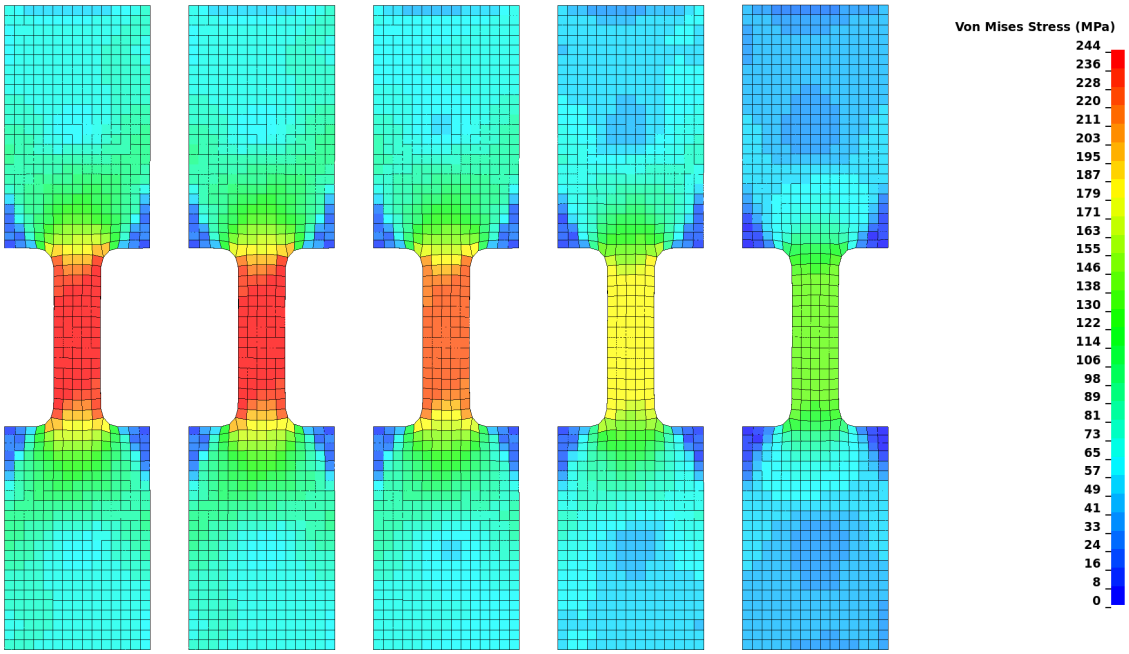

(g) $t_{\text{sim}} = 10.2\,\text{s}$ RT Max: 245 MPa (h) $t_{\text{sim}} = 10.2\,\text{s}$ $T_s = 100\,°\text{C}$ Max: 244 MPa (i) $t_{\text{sim}} = 10.2\,\text{s}$ $T_s = 150\,°\text{C}$ Max: 227 MPa (j) $t_{\text{sim}} = 10.2\,\text{s}$ $T_s = 200\,°\text{C}$ Max: 187 MPa (k) $t_{\text{sim}} = 10.3\,\text{s}$ $T_s = 250\,°\text{C}$ Max: 144 MPa (l) Colour scale σ^{eff} (MPa) for (g-k)

Figure 4.7: Von Mises stress (effective stress) σ^{eff} resulting from Voce values obtained for pre-set temperatures T_s and RT after first plotted state (a-e) and after appr. 10 s (g-k). Respective colour scales in (f) and (l).

The texture evolution in Figure 4.8 is shown by the average grain orientations of the VPSC-polycrystals defined in each element, using the IPF colouring in Figure 4.8a, which is the direct result of the weighted average crystal orientation from the reduced texture seen in Figure 3.6c of Section 3.4.3. The initial configuration used in all simulations is represented in Figure 4.8b. To highlight the change in the microstructure from the different temperatures, Figure 4.8c to Figure 4.8e display the evolution at the simulated time t_{sim} of the lowest temperature tensile test optimization result (RT), while Figure 4.8i to Figure 4.8k show the evolution at the highest pre-set temperature ($T_s = 250\,°\text{C}$). A texture evolution for an intermediate temperature ($T_s = 150\,°\text{C}$) is provided in Figure 4.8f to Figure 4.8h. Figure 4.8e, Figure 4.8h and Figure 4.8k show the corresponding last simulated time step. Due to the UTS occurring at different displacements in Figure 4.1, the total displacement of the simulation had to be set accordingly, via adapting the total simulated time t_{sim}. This leads to the last deformation step being performed at $t_{\text{sim}} = 16.8\,\text{s}$ and $10.3\,\text{s}$ for RT, $T_s = 150\,°\text{C}$ and $250\,°\text{C}$ respectively.

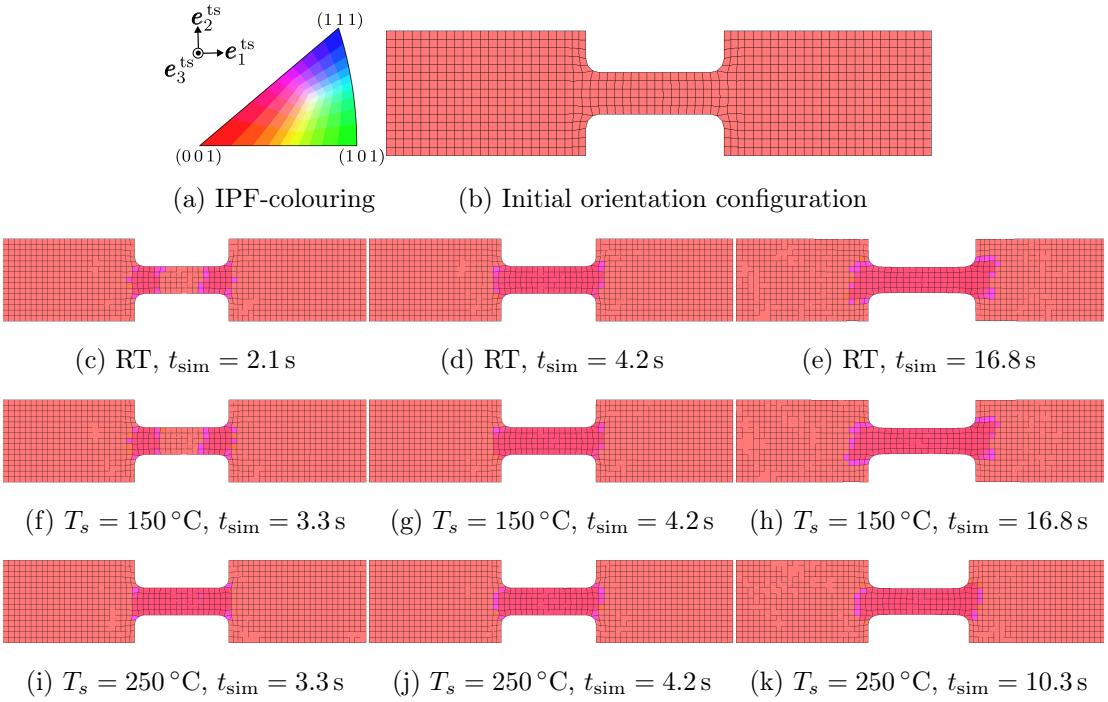

(a) IPF-colouring (b) Initial orientation configuration

(c) RT, $t_{\text{sim}} = 2.1\,\text{s}$ (d) RT, $t_{\text{sim}} = 4.2\,\text{s}$ (e) RT, $t_{\text{sim}} = 16.8\,\text{s}$

(f) $T_s = 150\,°\text{C}$, $t_{\text{sim}} = 3.3\,\text{s}$ (g) $T_s = 150\,°\text{C}$, $t_{\text{sim}} = 4.2\,\text{s}$ (h) $T_s = 150\,°\text{C}$, $t_{\text{sim}} = 16.8\,\text{s}$

(i) $T_s = 250\,°\text{C}$, $t_{\text{sim}} = 3.3\,\text{s}$ (j) $T_s = 250\,°\text{C}$, $t_{\text{sim}} = 4.2\,\text{s}$ (k) $T_s = 250\,°\text{C}$, $t_{\text{sim}} = 10.3\,\text{s}$

Figure 4.8: Average grain orientation of VPSC polycrystals at certain deformation steps, represented by an IPF-colour encoding (a). Change of the average crystal orientations from the initial configuration (b) over the simulated time for RT (c-e), for $T_s = 150\,°\text{C}$ (f-h) and for $T_s = 250\,°\text{C}$ (i-k).

Table 4.3 shows the total (rounded) CPU-time $t_{\text{tot}}^{\text{CPU}}$ as well as the average CPU-time per FEM iteration $\bar{t}_{\text{iter}}^{\text{CPU}}$ and the average CPU-time per deformation time step Δt ($\bar{t}_{\Delta t}^{\text{CPU}}$) of the presented simulations. While the optimization runs were done using 4 nodes consisting of 16 CPUs each, the cooling simulation was done using 12 such nodes. For the recalculation of $T_s = 250\,^{\circ}\text{C}$, only 2 nodes were available. One MPI-process was started per used CPU.

T_s	Δt	$t_{\text{tot}}^{\text{CPU}}$(s)	$\bar{t}_{\text{iter}}^{\text{CPU}}$(s)	$\bar{t}_{\Delta t}^{\text{CPU}}$(s)	No. nodes	CPUs
RT	0.3 s	33 664	152	601	4	64
100 °C	"	34 366	155	614	"	"
150 °C	"	21 258	96	380	"	"
200 °C	"	17 050	96	397	"	"
250 °C	"	16 600	97	461	"	"
"	0.1 s	71 681	117	664	2	32
Cooled	0.3 s	12 820	41	176	12	192

Table 4.3: Total used CPU time $t_{\text{tot}}^{\text{CPU}}$ of simulation runs, respective average per iteration $\bar{t}_{\text{iter}}^{\text{CPU}}$ and deformation step $\bar{t}_{\Delta t}^{\text{CPU}}$, as well as the available number of nodes and the corresponding number of CPUs for simulations presented.

5 Discussion

The discussion is divided into two distinct parts for the simulation results. Section 5.1 focuses on LS-OPT®'s performed FEM simulations, while Section 5.2 discusses the method developed in this thesis for approximating a plastic deformation of changing temperature. A final conclusion an outlook is provided in Section 5.3.

5.1 Constant Temperature Cases

In Section 5.1.1 the results for the optimizations regarding the agreement of the best macroscopic material responses with the tensile test data is discussed, while Section 5.1.2 focuses on the simulated influence of the microstructure evolution. The load-displacement curves of the experiments at RT and 100 °C (Figure 4.1a and Figure 4.1b) display macroscopically observable serrated load responses, which are a common feature in EN AW-5754 alloys [2]. This strain-path and temperature dependent material behaviour is known as PLC effect. Microscopically, the PLC effect is the result of Mg atoms interactions with mobile dislocations or other obstacles [2]. The temperature dependence of the PLC effect is visible when comparing the load curves of Figure 4.1a and Figure 4.1b with the ones at higher temperatures (Figure 4.1c to Figure 4.1e). This behaviour of the serrated load response also occurs in the verification experiment, when the specimen cooling has reached approximately 125 °C, shortly before the UTS (Figure 4.1f).

However, the PLC effect is not predominant texture dependent and is therefore neither considered in the derivations of Section 2.3.1 nor modelled in the simulations presented.

5.1.1 Optimization Results

For the constant temperature cases, Voce hardening parameters have successfully been calculated using the optimization approach laid out in Section 3.5.1. The obtained values result in force(load)-displacement curves, which describe the behaviour of the measured load-displacement curves well up to the UTS. This can be seen qualitatively in the direct comparison of Figure 4.2 with the measurements as well as quantitatively by the calculated PCM discrepancy d listed in Table 4.1. The biggest discrepancy of $d = 0.0080$ is given by the result for the $T_s = 250\,°\mathrm{C}$ case, which is observed due to the unstable stress responses the UMAT provided for the softer material in some finite element cells of low strain, leading to difficulties for the optimization procedures. As seen in Figure 4.2, lowering the deformation time step size from $\Delta t = 0.3\,\mathrm{s}$ to $0.1\,\mathrm{s}$ leads to a much smoother total load response on $\mathcal{R}_0$'s nodes. A similar issue is observed in Figure 4.2 in the optimization curve of the $T_s = 200\,°\mathrm{C}$ case for the displacement between 0.01 mm to 0.50 mm, which

can be reduced with smaller deformation time step sizes. However, the comparison with the measurement data shows the lowest discrepancy d of 0.0001 for $T_s = 200\,°\mathrm{C}$, closely followed by $T_s = 150\,°\mathrm{C}$ with $d = 0.0002$.

Otherwise, the Voce values for RT and $T_s = 100\,°\mathrm{C}$ seem to have been overestimated, as the simulated force(load)-displacement curves display stiffer material behaviour than measured. This is applicable in Figure 4.2 as well and leads to the corresponding discrepancies of 0.0030 and 0.0010 in Table 4.1. As the material load response of the EN AW-5754 tensile specimens was very similar up to the UTS (compare Figure 4.1a to Figure 4.1b) the 24 tensile test force-displacement curves (3 iterations $\times$ 8 individual tensile test simulations) were used to obtain the Voce value estimate for $T_s = 100\,°\mathrm{C}$. Refer to Section 3.5 for an explanation of the optimization routine. While the fitted support points of τ_0, τ_1, θ_0 for RT and $T_s = 100\,°\mathrm{C}$, display an expected slight downward trend, if compared to the other temperatures in Figure 4.4, θ_1 for RT is unexpectedly lower than what was estimated for $T_s = 150\,°\mathrm{C}$ and $150\,°\mathrm{C}$. The correlation matrix in Table 4.2 for the RT and $T_s = 100\,°\mathrm{C}$ case, shows θ_1 to have the lowest influence on the discrepancy, if compared to τ_0, τ_1 and θ_0. Such is expected, as referring to Equation (2.18), θ_1 describes the asymptotic behaviour of stage IV hardening, which becomes more dominant in higher strains. Nonetheless, the hardening parameters give a material behaviour of subsequently decreasing hardness, i.e. lower load bearing capacity, at higher temperatures, which is observed in Figure 4.2 for both the tensile test data and the simulation results. The difficulties the optimization faced for these two temperature cases is the result of the serrated load responses from the before mentioned PLC effect, which were not modelled but might still distort the discrepancy calculations. The problem becomes apparent if considering the θ_1 values of 23.25 MPa and 32.40 MPa for RT and $T_s = 100\,°\mathrm{C}$ respectively, still lead to very similar force responses in Figure 4.2.

Further investigating the correlation matrices in Table 4.2, shows expected dependencies of the Voce values with each other as well as with the obtained discrepancies. However, due to the differently set sampling boundaries for the Leapfrog Optimizer for Constrained minimization (LFOPC), LS-OPT® calculated varying correlations between the Voce parameters. Still, some expected dependencies can be readout. For example, τ_0 and θ_0 are mostly independent of each other, as one models the initial CRSS and the other nearly linear behaviour of the stage I "easy glide" hardening. Furthermore, a comparatively high correlation within each case can be seen between τ_1 and θ_1, which gives the height and tangential slope of the asymptote in the extended Voce hardening law in Equation (2.18). This asymptote models the highly temperature dependent stage III hardening and the transition to stage IV. Refer to Section 2.2.3 on the physical effects behind the mentioned stages of strain hardening.

The choice of the constraints used for LFOPC can be evaluated and compared between each optimization case, if the obtained Voce values are scaled to their respective sampling spaces. Such is provided in Figure 4.3, which shows them well within the set ranges for all temperatures. Attention is drawn in particular to the rescaled results for $T_s = 200\,°\mathrm{C}$, as its boundaries were not pre-estimated from previous simulations but directly set to the narrow bandwidths given by the fitted values of $T_s = 150\,°\mathrm{C}$ and $250\,°\mathrm{C}$, even

resulting in the closest match with the measurement curves and the lowest PCM value of Table 4.1. As not to introduce a bias into the fitting, comparatively much larger constrained spaces were used to sample the values for the independent optimizations of RT, $T_s = 150\,°\mathrm{C}$ and $250\,°\mathrm{C}$.

5.1.2 Interpretation of Strain-Stress Responses

The influence of the crystal orientation of VPSC polycrystals defined in each finite element has on the distribution of the macroscopic material responses is visible in both the contour plots of the effective plastic strain for the first printed deformation step in Figure 4.6a to Figure 4.6e and after appr. 10 s in Figure 4.6g to Figure 4.6k. It can be recognized by the propagation of the strongest strains along a 45° diagonal to the longitudinal direction (tensile direction) throughout all the different temperature cases. By comparing the von Mises stress distributions over the increasing temperature after approx. 10 s in Figure 4.7g to Figure 4.6k, it can be observed that the different set of Voce parameters indeed lead to lower yield stress, i.e. softer material, due to lower resulting CRSS for the FCC slip mode, as these are the only material specific parameters which have been changed in the different temperature cases. Furthermore, they are directly responsible for the UMAT stress responses to the FEM model. Refer to Section 2.3.1 and Section 3.3 on the mathematical details on how the stress responses calculated by VPSC are included into the FEM formulation. As expected, comparing the plastic stresses in Figure 4.7 with the plastic strains in Figure 4.6 for the same simulated time steps, the increase in temperature leads to an decrease of Von Mises stresses, which is compensated by an overall increase of the plastic strains, i.e. stronger plastic deformation.

Concerning the texture evolution, it becomes apparent that the tensile specimen geometry was simulated with a tensile axis rotated −45° off RD by taking note of the developing distribution of the average crystal orientations in Figure 4.8e. Furthermore, as all the other parameters of the VPSC-FEM coupled simulation were kept the same, the difference in the microstructure evolution for the highest temperature case ($T_s = 250\,°\mathrm{C}$), seen in Figure 4.8i to Figure 4.8j, compared to the lowest investigated temperature (RT $\approx$ 23.7 °C), seen in Figure 4.8c to Figure 4.8d, is the direct result of the different sets of Voce hardening values (Table 4.1).

5.2 Temperature Interpolation

Using the proposed change of certain microstructural material parameters by only estimating the increase of the CRSS, did successfully result in a load response behaviour similar to what was observed in the verification experiment of constant cooling, if simulation and measurement data in Figure 4.5b are compared. While giving a first proof of concept, some larger issues still persist.

First, general deviations from the measurement: The simulated force in tensile direction did not completely match the one obtained from the verification experiment. At a displacement of about 0.5 mm, a jump can be seen in the load response. This is not

completely unexpected, considering the specimen had a temperature of about 220 °C at this deformation (see Figure 4.5a). Such an instability should occur, as the curve of $T_s = 250\,°C$ for $\Delta t = 0.3\,°C$ had a jump in the force response at this same displacement as well and the cooling simulation was performed with the same time step size. The deviation of the calculated force response to the measurement between the displacements of 1.5 mm to 2.5 mm does correspond with the largest deviation of the measured specimen temperature from linearity, leading to a higher hardness being calculated in this region than was measured. In the end of the cooling simulation, numerical instability occurs, as the calculated force response seems to fluctuate for a displacement larger than 2.0 mm. This, however, seems to be an issue specific to the FEM-model or used solver, as such behaviour was seen for some of the 24 combinations of sampled hardening parameters of the RT case, which used the classical VPSC Voce implementation, as well. Reruns of such simulations suggest adapting the convergence test performed by the iterative method of the FEM solver for assembling Equation (3.10b). A promising fix for the problem of unstable load responses seems to be to change the convergence criteria from a total displacement increment ratio evaluated over the entire simulation, to a ratio evaluated only over the current time step. This is controlled by setting the LS-DYNA® keyword DNORM [19, Volume I].

Second, latent hardening: Unlike the stepwise CRSS calculation with Equation (2.19), latent hardening cannot be considered by directly implementing the continuous Voce hardening of Equation (2.18). This does not seem to be a problem with the investigated EN AW-5754 sheet metal using only one slip mode, but might be a problem for different alloy compositions.

Third, elastic constants: The single crystal plasticity is temperature dependent [36] but the elastic behaviour at RT was set fixed for all simulations. However, as mentioned before, this does not seem to be the main cause of the discrepancy of the measured and simulated force(load)-displacement curves in Figure 4.2 and Figure 4.5b.

5.3 Conclusion and Outlook

In this thesis, the coupling of the VPSC material model to a commercial FEM-solver, as used by LKR, is described in detail. Microscopic material parameters for calculating strain hardening of a polycrystalline EN AW-5754 (AlMg3) metal sheet are determined and validated against tensile test results. The influence of the microstructure evolution on the plastic deformation is discussed. An extension to the calculation method of the CRSS, using the classical 4-parametric Voce hardening law, is presented and applied to a linearly cooled tensile specimen. The resulting macroscopic material responses of said method were evaluated against measurement data. An application of the extended method for other deformation cases might be feasible, which would give a method depending only on 4 parameters per slip mode and temperature for fast simulating large thermo-mechanical industrial metal forming problems.

Further adjustments and investigations into the FEM convergence criteria for the coupled microstructural UMAT with LS-DYNA® are currently outstanding, to avoid

fluctuations in the macroscopic force responses. Improvements in the optimization routines might be obtained, if the dependencies of τ_0, τ_1, θ_0 and θ_1 on the stages of work hardening are considered more dominantly in the sampling for the optimization iteration. A physical informed sampling algorithm, which also considers the texture evolution explicitly in certain elements, could be promising.

Concluding

1. A robust method for determining microscopic material parameters for polycrystalline strain hardening using the Voce hardening law was presented.
2. The influence of temperature on the plastic deformation was realized via adjustment of slip mode activation energies (i.e. CRSS) in a polycrystalline FCC aggregate.
3. A new method for using VPSC-FEM, which will be useful for thermo-mechanical industrial metal forming problems was introduced and evaluated.

Bibliography

[1] B. S. Anglin, B. T. Gockel and A. D. Rollett. 'Developing constitutive model parameters via a multi-scale approach'. In: *Integrating Materials and Manufacturing Innovation* 5.1 (July 2016), pp. 212–231. DOI: 10.1186/s40192-016-0053-4.

[2] O. Berk Aytuna and Mert Efe. 'Investigation of Portevin-LeChatelier Bands in 5754 Aluminum Alloy under Various Strain Paths'. In: *Procedia Structural Integrity* 21 (2019), pp. 120–129. ISSN: 2452-3216. DOI: 10.1016/j.prostr.2019.12.093.

[3] *DOE fundamentals handbook: Material science. Volume 1*. DOE-HDBK-1017/1-93. U.S. Department of Energy. Washington, D.C. 20585, United States, Jan. 1993. URL: https://www.standards.doe.gov/standards-documents/1000/1017-BHdbk-1993-v1/@@images/file.

[4] Martin Fleck. *Burgers Vector and dislocations (screw and edge type)*. Aug. 2020. URL: https://commons.wikimedia.org/w/index.php?curid=96858277 (visited on 18/05/2024).

[5] J. T. Fourie and R. J. Murphy. 'Elongated dislocation loops and the stress-strain properties of copper single crystals'. In: *Philosophical Magazine* 7.82 (Oct. 1962), pp. 1617–1631. ISSN: 0031-8086. DOI: 10.1080/14786436208213699.

[6] Günter Gottstein. *Materialwissenschaft und Werkstofftechnik : Physikalische Grundlagen*. ger. 4th ed. 2014. Springer-Lehrbuch. Berlin, Heidelberg : Springer Berlin Heidelberg : Imprint: Springer Vieweg, 2014. ISBN: 3-642-36603-1.

[7] Rudolf Gross and Achim Marx. *Festkörperphysik*. De Gruyter, Oct. 2022. ISBN: 9783110782394. DOI: 10.1515/9783110782394.

[8] M.E. Harr, S. Daly and A.L. Pilchak. 'The effect of temperature on slip in microtextured Ti-6Al-2Sn-4Zr-2Mo under dwell fatigue'. In: *International Journal of Fatigue* 147 (June 2021), p. 106173. ISSN: 0142-1123. DOI: 10.1016/j.ijfatigue.2021.106173.

[9] Rodney Hill. *The mathematical theory of plasticity*. eng. 1. publ. in Oxford classic series. Oxford classic texts in the physical sciences. Oxford et al.: Clarendon Pr., 1998. ISBN: 0198503679.

[10] William F. Hosford. *Mechanical Behavior of Materials*. Cambridge University Press, Nov. 2009. ISBN: 9781107642461. DOI: 10.1017/cbo9780511810923.

[11] Claes Johnson. *Numerical solution of partial differential equations by the finite element method*. Dover ed. Dover books on mathematics. Mineola: Dover Publications, 2009. 278 pp. ISBN: 9780486469003.

[12] Hans Kerner. *Mathematik für Physiker*. ger. 3., überarb. Aufl. 2013. Springer-Lehrbuch. Berlin, Heidelberg: Springer Berlin Heidelberg, 2013. ISBN: 9783642376542.

[13] Kloeckner Metals Germany. *EN AW-5754 Datenblatt: Eigenschaften, Anwendungsbeispiele, Besoderheiten*. 2024. URL: https://facts.kloeckner.de/werkstoffe/aluminium/3-3535/ (visited on 10/09/2024).

[14] Marko Knezevic and Nicholas W. Landry. 'Procedures for reducing large datasets of crystal orientations using generalized spherical harmonics'. In: *Mechanics of Materials* 88 (Sept. 2015), pp. 73–86. ISSN: 0167-6636. DOI: 10.1016/j.mechmat.2015.04.014.

[15] Shiro Kobayashi. *Metal Forming and the Finite-Element Method*. Ed. by Soo-Ik Oh and Taylan Altan. Oxford Series on Advanced Manufacturing Ser v.4. New York: Oxford University Press, Incorporated, 1989. 1398 pp. ISBN: 9780195364576.

[16] Johannes Kronsteiner et al. 'Modeling of Texture Development during Metal Forming Using Finite Element Visco-Plastic Self-Consistent Model'. In: *Crystals* 14.6 (June 2024), p. 533. ISSN: 2073-4352. DOI: 10.3390/cryst14060533.

[17] Ricardo A. Lebensohn, C. N. Tomé and P. Ponte CastaÑeda. 'Self-consistent modelling of the mechanical behaviour of viscoplastic polycrystals incorporating intragranular field fluctuations'. In: *Philosophical Magazine* 87.28 (Aug. 2007), pp. 4287–4322. ISSN: 1478-6443. DOI: 10.1080/14786430701432619.

[18] Ricardo A. Lebensohn and Carlos N. Tomé. 'A self-consistent anisotropic approach for the simulation of plastic deformation and texture development of polycrystals: Application to zirconium alloys'. In: *Acta Metallurgica et Materialia* 41.9 (Sept. 1993), pp. 2611–2624. ISSN: 0956-7151. DOI: 10.1016/0956-7151(93)90130-k.

[19] Livermore Software Technology Corporation LSTC. 'LS-DYNA Keyword User's Manual Volume I-III'. In: 09/24/21. User manual R13.01 for LS-DYNA finite element code. Livermore, CA, Oct. 2021. URL: https://www.dynasupport.com/manuals/ls-dyna-manuals.

[20] Livermore Software Technology Corporation LSTC. *LS-DYNA Theory Manual*. 03/16/23. Draft theory manual for LS-DYNA finite element code. ANSYS, Inc. Livermore, CA, Mar. 2023. URL: https://ftp.lstc.com/anonymous/outgoing/web/ls-dyna_manuals/DRAFT/DRAFT_Theory.pdf.

[21] Russell E. Marki and Marko Knezevic. 'Nonlinear optimization for compact representation of orientation distributions based on generalized spherical harmonics'. In: *Journal of the Mechanics and Physics of Solids* 187 (2024), p. 105609. ISSN: 0022-5096. DOI: https://doi.org/10.1016/j.jmps.2024.105609. URL: https://www.sciencedirect.com/science/article/pii/S0022509624000759.

[22] A. Molinari, G.R. Canova and S. Ahzi. 'A self consistent approach of the large deformation polycrystal viscoplasticity'. In: *Acta Metallurgica* 35.12 (Dec. 1987), pp. 2983–2994. ISSN: 0001-6160. DOI: 10.1016/0001-6160(87)90297-5.

[23] Dmitri A. Molodov, ed. *Microstructural design of advanced engineering materials*. First edition. Includes bibliographical references and index. Weinheim, Germany: Wiley-VCH, 2013. 1507 pp. ISBN: 9783527652846.

[24] Alois C. Ott et al. 'Automatic Texture Alignment by Optimization Method'. In: *Microscopy and Microanalysis* 30.2 (Mar. 2024), pp. 253–277. ISSN: 1435-8115. DOI: 10.1093/mam/ozae013.

[25] Horst Parisch. *Festkörper-Kontinuumsmechanik. Von den Grundgleichungen zur Lösung mit Finiten Elementen*. Teubner Studienbücher Technik. Wiesbaden: Vieweg+Teubner Verlag, 2003. 13699 pp. ISBN: 9783322800527.

[26] Valerie Randle. *Introduction to texture analysis : macrotexture, microtexture and orientation mapping*. eng. Amsterdam: Gordon and Breach, 2000. ISBN: 9056992244.

[27] Anthony D. Rollett and U.F. Kocks. 'A Review of the Stages of Work Hardening'. In: *Solid State Phenomena* 35-36 (Sept. 1993), pp. 1–18. DOI: 10.4028/www.scientific.net/ssp.35-36.1.

[28] Javier Segurado et al. 'Multiscale modeling of plasticity based on embedding the viscoplastic self-consistent formulation in implicit finite elements'. In: *International Journal of Plasticity* 28.1 (Jan. 2012), pp. 124–140. ISSN: 0749-6419. DOI: 10.1016/j.ijplas.2011.07.002.

[29] J.A. Snyman. 'A new and dynamic method for unconstrained minimization'. In: *Applied Mathematical Modelling* 6.6 (Dec. 1982), pp. 449–462. ISSN: 0307-904X. DOI: 10.1016/s0307-904x(82)80007-3.

[30] J.A. Snyman. 'The LFOPC leap-frog algorithm for constrained optimization'. In: *Computers & Mathematics with Applications* 40.8–9 (Oct. 2000), pp. 1085–1096. ISSN: 0898-1221. DOI: 10.1016/s0898-1221(00)85018-x.

[31] Stefan C. Soare. 'Plasticity and non-Schmid effects'. In: *Proceedings of the Royal Society A: Mathematical, Physical and Engineering Sciences* 470.2161 (Jan. 2014), p. 20130440. ISSN: 1471-2946. DOI: 10.1098/rspa.2013.0440.

[32] Nielen Stander et al. *LS-OPT User's Manual*. Version 7.0. A design optimization and probabilistic analysis tool for the engineering analyst. LSTC. Livermore, CA, Nov. 2020. URL: https://www.lsoptsupport.com/documents/manuals/ls-opt/lsopt_70_manual.pdf.

[33] Elias Theil. 'Clustering technique for efficient coupled simulations of grain structure and precipitation kinetics'. en. MA thesis. TU Wien, 2022. DOI: 10.34726/HSS.2022.97561.

[34] Carlos N. Tomé. *Material Modeling with the Visco-Plastic Self-Consistent (VPSC) Approach. Theory and Practical Applications*. Ed. by Ricardo A. Lebensohn. Elsevier Series on Plasticity of Materials Series. San Diego: Elsevier, 2023. 1381 pp. ISBN: 9780128207208. DOI: 10.1016/C2019-0-01217-4.

[35] Carlos N. Tomé et al. 'The relation between macroscopic and microscopic strain hardening in F.C.C. polycrystals'. In: *Acta Metallurgica* 32.10 (Oct. 1984), pp. 1637–1653. ISSN: 0001-6160. DOI: 10.1016/0001-6160(84)90222-0.

[36] J. Vallin et al. 'Elastic Constants of Aluminum'. In: *Journal of Applied Physics* 35.6 (June 1964), pp. 1825–1826. ISSN: 1089-7550. DOI: 10.1063/1.1713749.

[37] E. Voce. 'Empirical Formulae for the Determination of Stress Curves'. In: *The Journal of the Royal Aeronautical Society* 59.533 (1955), pp. 362–364. DOI: 10.1017/S0368393100117626.

[38] E. Voce. 'The Relationship Between Stress and Strain for Homogeneous Deformation'. In: *Journal of the Institute of metals* 74 (1948), pp. 537–562.

[39] Miroslav Zecevic and Marko Knezevic. 'A new visco-plastic self-consistent formulation implicit in dislocation-based hardening within implicit finite elements: Application to high strain rate and impact deformation of tantalum'. In: *Computer Methods in Applied Mechanics and Engineering* 341 (Nov. 2018), pp. 888–916. ISSN: 0045-7825. DOI: 10.1016/j.cma.2018.07.027.

[40] Miroslav Zecevic et al. 'Viscoplastic self-consistent formulation as generalized material model for solid mechanics applications'. In: *Applications in Engineering Science* 6 (June 2021), p. 100040. ISSN: 2666-4968. DOI: 10.1016/j.apples.2021.100040.

[41] Feng Zhao, Yikun Zhu and Jinhong Xie. 'Deformation twinning in pure aluminum under ultrahigh strain rate: Dependence of strain rate and crystallographic orientation'. In: *Materials Letters* 285 (Feb. 2021), p. 129181. ISSN: 0167-577X. DOI: 10.1016/j.matlet.2020.129181.

Acronyms

AIT Austrian Institute of Technology. 2

AW Aluminium Wrought. iii, v, xi, 45, 47, 48, 65, 66, 68

BCC Body Centered Cubic. ix, 7, 16, 20–22

CP crystal plasticity. iii, v, 1

CRSS Critical Resolved Shear Stress. 21–25, 28, 30, 50, 51, 58, 60, 66–69

EBSD Electron Back Scatter Diffraction. xi, 14, 37, 46–48

EN European Norm. iii, v, xi, 45, 47, 48, 65, 66, 68

FCC Face Centered Cubic. ix, 7, 16, 19, 20, 48, 49, 54, 67, 69

FDM Finite Difference Method. 39

FEM Finite Element Method. iii, v, xi, 1, 2, 24, 26, 27, 30, 31, 33, 37–39, 41–45, 49, 50, 52, 55, 60, 64, 65, 67–69

HCP Hexagonal Close Packed. ix, 7, 16, 20

HEM Homogeneous Effective Medium. 27, 29, 44

IPF Inverse Pole Figure. xi, xii, 15, 18, 19, 48, 63

LFOPC Leapfrog Optimizer for Constrained minimization. 49, 54, 57, 58, 66

LKR Leichtmetallkompetenzzentrum Ranshofen. i, xi, 2, 34, 37, 38, 42, 46, 68

ND Normal-Direction. xi, 15, 17, 18, 46, 48, 52

PCM Partial Curve Mapping. ix, 49, 50, 56, 58, 65, 67

PDE Partial Differential Equation. 2, 31–33, 39, 40, 42

PF Pole Figure. xi, 18, 48

PLC Portevin-LeChatelier. 65, 66

RD Rolling-Direction. xi, 14, 15, 17, 18, 46, 48, 67

RSS Resolved Shear Stress. 20, 21, 23

RT Room Temperature. xii, 34, 46, 55, 56, 58, 61–68

TD Transverse-Direction. xi, 15, 17, 18, 46, 48

UMAT User Defined Material Model. xi, 37, 38, 42, 44, 45, 49, 50, 52, 53, 58, 60, 65, 67, 68

UTS Ultimate Tensile Strength. xii, 33, 47, 53, 55, 56, 63, 65, 66

VPSC Visco-Plastic Self-Consistent. iii, v, xi, xii, 1, 2, 26–28, 30, 33, 37, 38, 42–45, 49–54, 60, 63, 67–69